

COMPARISON OF THE MICROSTRUCTURE OF
THE BIVALVE SHELLS *PINCTADA FUCATA* AND
ANODONTA CYGNEA AND THE GASTROPOD
SHELL *PHORCUS TURBINATUS*

Dissertation

Zur Erlangung des Doktorgrades

an der

Fakultät für Mathematik, Informatik und Naturwissenschaften im

Fachbereich Geowissenschaften

der Universität Hamburg

vorgelegt von

Jianhan He

aus Jingzhou, P.R.China

Hamburg, 2018

Vorsitzende/r: Prof. Dr. Ulrich Bismayer

Erstgutachter: Prof. Dr. Ulrich Bismayer

Zweitgutachter: Prof. Dr. Jochen Schlüter

Datum der Disputation: 05. Juni 2018

Eidesstattliche Versicherung

Declaration on oath according to § 7 (4) doctoral degree regulations of MIN faculty

Hiermit erkläre ich an Eides statt, dass ich die vorliegende Dissertationsschrift selbst verfasst und keine anderen als die angegebenen Quellen und Hilfsmittel benutzt habe.

I hereby declare, on oath, that I have written the present dissertation by my own and have not used other than the acknowledged resources and aids.

Hamburg 27.03.2018

Hamburg, den / *city and date*

A handwritten signature in black ink that reads "Jianhan He". The signature is written in a cursive style with a light yellow highlight behind it.

Unterschrift / *signature*

‘Many years later as he faced the firing squad, Colonel Aureliano Buendía was to remember that distant afternoon when his father took him to discover ice.’

Gabriel García Márquez, *One Hundred Years of Solitude*.

For my father Shunyou He and my mother Zhengxiang Lei.

Content

Abstract	3
1 Introduction	7
1.1 Biominerals and biomineralization	7
1.1.1 Species of biominerals	8
1.1.2 Biominerals and organic matrix in molluscs.....	9
1.1.3 Studies of biominerals based on EBSD and Raman spectroscopy	12
1.2 Molluscs.....	16
1.2.1 Bivalvia	16
1.2.2 Gastropoda	19
1.3 Calcium carbonates.....	23
1.3.1 Calcite	23
1.3.2 Aragonite.....	24
2 Materials and methods.....	26
2.1 Samples and sample preparation.....	26
2.2 Scanning electron microscopy (SEM)	30
2.3 Electron backscatter diffraction	31
2.4 Laser Raman spectroscopy.....	33
2.5 Electron microprobe.....	38
3 Results.....	39
3.1 Morphology of samples	39
3.1.1 <i>Pinctada fucata</i>	39
3.1.2 <i>Anodonta cygnea</i>	42
3.1.3 <i>Phorcus turbinatus</i>	45
3.2 Crystallography orientation of samples	48
3.2.1 <i>Pinctada fucata</i>	48
3.2.2 <i>Anodonta cygnea</i>	55
3.2.3 <i>Phorcus turbinatus</i>	70
3.3 Chemical composition of samples	76
3.3.1 <i>Pinctada fucata</i>	76

3.3.2	<i>Anodonta cygnea</i>	80
3.3.3	<i>Phorcus turbinatus</i>	84
4	Discussion	89
4.1	Nacreous layers	89
4.2	Prismatic layers	94
4.3	From prisms to nacre	99
5	Conclusions	101
	Bibliography	103
	Appendix	113
	Appendix I	113
	Appendix II	115
	Appendix III	116
	Appendix IV	117
	Appendix V	118
	Appendix VI	119
	Curriculum Vitae	120
	List of publications	122
	Acknowledgements	123

Abstract

The structure of mollusc shells is of major interest in the field of biomineral research due to its potential application in bionic materials. In order to understand the physical/chemical background of their outstanding biomechanical properties, in this study topological and material features were revealed using several morphological, crystal orientational and spectroscopic methods.

Three shells from different habitats were selected as the main experimental subjects: a bivalve named *Pinctada fucata* from South China Sea, another bivalve named *Anodonta cygnea* from the Volga River in Russia and a gastropod *Phorcus turbinatus* from the Mediterranean Sea on the coast of France.

By applying scanning electron microscope, the structures of the shells were studied in detail. By using electron backscatter diffraction and Raman spectroscopy, the variation of the crystal orientation in different crystallites was investigated comprehensively. Furthermore, microprobe and electron microscopy provided insight into the compositional and morphological differences between the three species.

Shells of the three species have similar mesoscopic structure, which consists of two types of layers: nacreous layer and prismatic layer. From the crystallographic arrangement, such as the distribution of domain structure and mesoscale twinning, differences of nacreous layers in three species were compared. Based on differences in compositions, mesostructures and crystallographic features, the structural information of prismatic layers is enhanced. Finally, the transition between two layers and possible growth modes have been discussed in this work.

In the three species, the inner part of the shell is an aragonitic nacreous layer composed of nacre tablets in 'brick-and-mortar' arrangement. The *c*-axis of aragonite crystallites of the three species has identical orientation, the *a*- or *b*-axis is however arranged in different domain structures. Cross sections of all investigated species show experimental evidence that the aragonite particles with similar crystallographic orientation grow through several organic boundaries forming larger clusters. Besides, the nacreous layers from the three species show different degrees of co-orientation and different distribution of mesoscale twinning.

The prismatic layers of the three species contain compact prisms with their elongated axes often perpendicular to the surface of the shell. They do however possess different microstructures. In *Pinctada fucata*, each prism is an assemblage of highly co-oriented calcite

crystallites. This high degree of co-orientation bundles the *c*-axis of crystallites within each prism mainly along one direction with a small dispersion. Different calcitic prisms can still have different orientations of their *c*-axis. In contrast, the prisms of *Anodonta cygnea* and *Phorcus turbinatus* are assembled by aragonite crystallites and within each prism, there is a high amount of mesoscale twinning. Although the aragonite crystallites from the two species are arranged in granular and pinnate textures, respectively, the *c*-axis of crystallites in aragonitic prisms align also in mainly one direction with a larger degree of dispersion. The *a*- and *b*-axes are less co-oriented and grouped in domains when compared with *Pinctada fucata*. Besides, considerable amount of organic matter can be found between the prisms of *Pinctada fucata* and *Anodonta cygnea*, but less in *Phorcus turbinatus*.

The interfacial area where prismatic layer transits to nacreous layer has also distinguishable features among the three species. In *Pinctada fucata*, between nacreous and prismatic layers there occurs a layer of organic matter, which cannot be seen in the same order of magnitude in the other two species. The transformation range from calcitic prisms to nacre has a sharp boundary in *Pinctada fucata*. In *Anodonta cygnea*, the orientation of aragonitic nacre tablets is partly inherited from the fibrous crystallites in the aragonitic prisms.

It is shown in the study that electron backscatter diffraction combined with scanning electron microscope is a powerful tool to resolve the microstructure of biominerals. The application of Raman spectroscopy for the orientational study of biominerals has also been proved to be a promising new technique, although further studies are needed. At last, the relationship between the habitats and the microstructures have been discussed.

Zusammenfassung

Die Struktur von Molluskenschalen ist für potentielle Anwendungen in bionischen Materialien von großem Interesse auf dem Gebiet der Biomineralforschung. Um den physikalisch-chemischen Hintergrund ihrer biomechanischen Eigenschaften zu verstehen, wurden in dieser Arbeit topologische und Materialcharakteristika unter Verwendung verschiedener morphologischer, kristallographischer und spektroskopischer Methoden studiert.

Drei Schalen aus verschiedenen Habitaten wurden als Hauptversuchsobjekte ausgewählt: eine Salzwassermuschel aus dem Südchinesischen Meer (*Pinctada fucata*), eine Süßwassermuschel aus der Wolga in Russland (*Anodonta cygnea*) und ein Gastropode (*Phorcus turbinatus*) von der französischen Mittelmeerküste.

Mit dem Rasterelektronenmikroskop wurden die Strukturen der Schalen detailliert untersucht. Mittels Elektronenrückstreubeugung und Ramanspektroskopie wurde die Kristallorientierung der verschiedenen Kristallite umfassend untersucht. Darüber hinaus hat die Elektronenstrahlmikrosonde und die Elektronenmikroskopie einen Einblick in die kompositorischen und morphologischen Unterschiede zwischen den drei Arten ermöglicht.

Die Schalen der drei Arten haben eine ähnliche mesoskopische Struktur, die aus zwei unterschiedlichen Schichten besteht: eine prismatische Schicht und eine Perlmuttertschicht. Mittels Gesichtspunkten der kristallographischen Anordnung, der räumlichen der Domänenstruktur und der mesoskaligen Verzwilligung, wurden die Perlmuttertschichten dreier Spezies im Detail verglichen. Basierend auf Unterschieden in Zusammensetzung, der mesostrukturen und der kristallographischen Merkmale wurden neue Informationen über die prismatischen Schichten der drei Spezies gewonnen. Darüber hinaus wird der Übergang zwischen den Schichten und ihr möglicher Wachstumsmodus in dieser Arbeit diskutiert.

Bei allen drei Spezies ist der innere Teil der Schale eine aragonitische Perlmuttertschicht, die eine 'Backstein-Mörtel-Komposition' aufweist, jedoch in unterschiedlichen Mustern ausgeprägt ist. Die *c*-Achse der Aragonitkristallite ist bei allen drei Spezies identisch orientiert, die *a*- oder *b*-Achse weist jedoch verschiedene Domänenstrukturen auf. Die Querschnitte aller untersuchten Spezies zeigen experimentell, dass die Aragonitpartikel mit der selben kristallographischen Orientierung durch mehrere organische Grenzen wachsen und dadurch größere Cluster bilden. Außerdem weisen die Perlmuttertschichten der drei Arten unterschiedliche

Grade der Koorientierung und unterschiedliche Verteilungen der mesoskaligen Zwillingsbildung auf.

Die prismatischen Schichten der drei Spezies enthalten kompakte Prismen, deren längliche Tracht oft senkrecht zur Oberfläche der Schale stehen. Sie besitzen jedoch unterschiedliche Mikrostrukturen. In *Pinctada fucata* besteht jedes Prisma aus einer Ansammlung hochkoordinierter Calcitkristallite. Dieser hohe Koorientierungsgrad bündelt die *c*-Achse von Kristalliten in jedem Prisma hauptsächlich entlang einer Richtung bei nur geringer Streuung. Unterschiedliche calcitische Prismen können jedoch unterschiedliche Orientierungen ihrer *c*-Achse aufweisen. Im Gegensatz dazu werden die Prismen von *Anodonta cygnea* und *Phorcus turbinatus* aus Aragonit-Kristalliten gebildet und in jedem Prisma tritt mesoskalige Zwillingsbildung häufig auf. Obwohl die Aragonitkristallite der beiden Spezies in körnigen und gefiederten Strukturen angeordnet sind, richtet sich die *c*-Achse der Kristallite in den aragonitischen Prismen primär entlang einer Richtung mit einem größeren Dispersionsgrad aus. Die *a*- und *b*-Achsen sind im Vergleich zu *Pinctada fucata* weniger koorientiert und in Domänen gruppiert. Außerdem können organische Substanzen zwischen den Prismen von *Pinctada fucata* und *Anodonta cygnea* beobachtet werden, jedoch kaum in *Phorcus turbinatus*.

Der Übergangsbereich zwischen prismatischer und perlmuttartiger Schicht weist in beiden drei Spezies ebenfalls Unterschiede auf. In *Pinctada fucata* tritt zwischen den Perlmutter- und prismatischen Schichten ein Bereich organischer Substanz auf, die bei den beiden anderen Arten nicht in der gleichen Größenordnung gefunden wird. Die Umwandlungsregion von calcitischen Prismen zu Perlmutter weist in *Pinctada fucata* eine scharfe Grenze auf. In *Anodonta cygnea* wird die Orientierung der aragonitischen Perlmutter-Segmente zum Teil von den faserigen Kristalliten der aragonitischen Prismen übernommen.

In der Studie wurde nachgewiesen, dass die Elektronenrückstreubeugung in Kombination mit dem Rasterelektronenmikroskop ein leistungsfähiges Werkzeug zur Auflösung der Mikrostruktur von Biomineralen ist. Die Anwendung der Raman-Spektroskopie hat sich für die Orientierungsuntersuchung von Biomineralen ebenfalls als sehr vielversprechende Technik erwiesen. Basierend auf den morphologischen und orientierungsabhängigen Analysen werden mögliche Wachstumsmodelle von Schalen und die Beziehung zwischen Habitaten und Mikrostrukturen diskutiert.

1 Introduction

1.1 Biominerals and biomineralization

From bacteria (e.g. *Magnetospirillum magneticum*) (Fdez-Gubieda *et al.*, 2013) to molluscs (e.g. *Haliotis rufescens*) (Pérez-Huerta *et al.*, 2011), echinoderms (e.g. *Ophiocoma wendtii*) (Aizenberg *et al.*, 2001) and mammals, from the calcium oxalate in plants (Monje and Baran, 2002) to the hydroxyapatite in animals (Bismayer *et al.*, 2005), different living species produce different minerals. These minerals produced in organisms, often comprise both, inorganic crystallites and organic matrices. Since they differ from their abiogenetic equivalent in terms of shape, structure, trace elements and organic content, they are called biominerals. Fig. 1.1 shows the different morphologies of an aragonitic pearl and an aragonite single-crystal of geological origin.

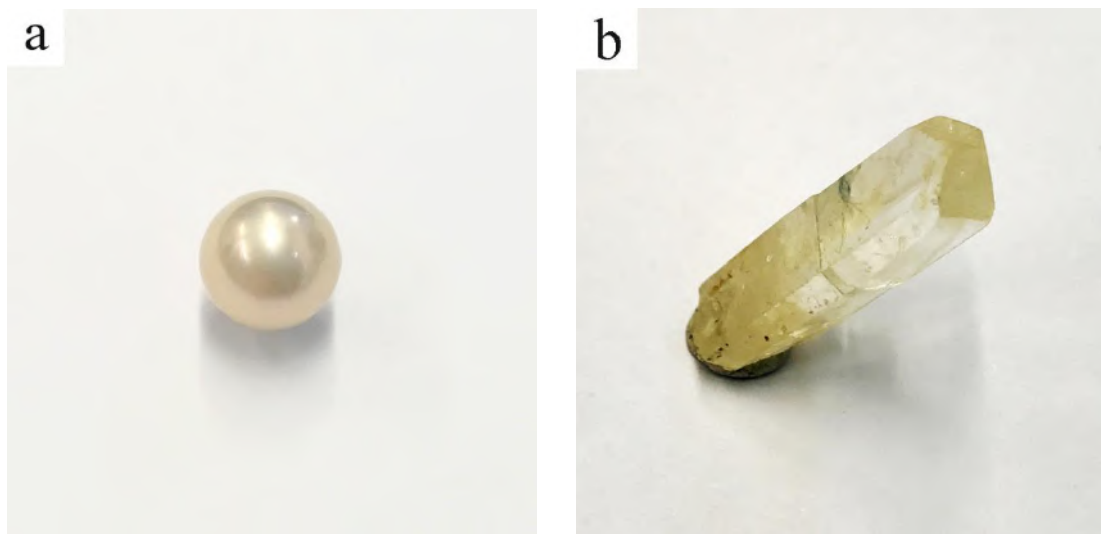


Fig. 1.1 Morphologies of an aragonitic pearl (a) and an abiogenetic single-crystal of aragonite (b)

Biominerals exist in or outside living species as skeletons, teeth, thorns or shells. Their function in living species is mainly to uphold, move, digest and protect, including other gravitational, magnetic or optical sensors.

Distinguished from abiogenetic minerals, biominerals are formed under controlled conditions. Under biological conditions, the growth of biominerals in organisms always involves organic material, which finally occurs in the mineral composition. The assemblage of organic and inorganic from nanoscopic to macroscopic dimension creates a precise and well-

1.1 Biominerals and biomineralization

organized hierarchical structure. The complex process of such a biologically controlled mineralization is called biomineralization.

The well-organized organic-inorganic hierarchical structure makes biominerals' mechanical properties superior to their abiogenic equivalent minerals (*Ji and Li, 2014; Liang et al., 2016; Li et al., 2017*). For example, the pearl shown in Fig. 1.1 composed by 95% of aragonite crystallites is much more fracture-resistant than a single-crystal of aragonite (*Smith et al., 1999*). The key to learning these superb properties exists in the understanding of their microstructures.

1.1.1 Species of biominerals

More than 60 biomineral types have been found so far in organisms. They consist of more than 25 chemical elements such as hydrogen, carbon, oxygen, magnesium, silicon, phosphor, sulphur, calcium, manganese, iron and more. Calcium is the most widely distributed element and carbonates are the most common biominerals. The exoskeletons of invertebrates are often made of calcium carbonates, and the endoskeletons of vertebrates are often made of calcium phosphates. Other trace elements can be also found in biominerals. For example, strontium and barium are mineralized as intracellular sulphate in some algae (*Bertini, 2007*). Table 1.1 shows various types of biominerals formed in different organisms and their locations.

Table 1.1 The main biomineral types

biomineral	formula	example of location
calcium carbonate	CaCO ₃	calcite shells of foraminifera (<i>Theodor et al., 2016</i>)
		aragonite core of corals (<i>Cusack et al., 2008</i>)
		vaterite spicules of ascidian (<i>Pokroy et al., 2015</i>)
		amorphous cuticle of crustaceans (<i>Raz et al., 2002</i>)
calcium phosphate	Ca ₁₀ (PO ₄) ₆ (OH) ₂	scales of fish (<i>Huang et al., 2011</i>)
		hydroxyapatite human teeth and bones (<i>Driessens and Verbeeck, 1990</i>)
	octacalcium phosphate	Ca ₈ H ₂ (PO ₄) ₆ bones of mice (<i>Crane et al., 2006</i>)
calcium oxalate	CaC ₂ O ₄ ·2H ₂ O	whewellite kidney stones of human (<i>Daudon et al., 2009</i>)
		weddellite

1.1 Biominerals and biomineralization

silica	$\text{SiO}_2 \cdot n\text{H}_2\text{O}$	teeth of limpets (<i>Mann et al.</i> , 1986)
goethite	$\alpha\text{-FeOOH}$	
magnetite	Fe_3O_4	teeth of chitons (<i>Weaver et al.</i> , 2010)
iron phosphate	FePO_4	

1.1.2 Biominerals and organic matrix in molluscs

The organic matrix of biominerals refers to localized organic composites including proteins, phospholipid, collagen, carbohydrate, etc. The organic matrix is a minor part of biominerals but plays a very important role during growth and for material properties.

In the seventies, the shells of bivalve animals were often treated with ethylenediaminetetraacetic acid (EDTA) to remove inorganic compositions mildly without destroying the structure of the organic matrix (*Crenshaw*, 1972). Since then the study of organic matrix in mollusc shells has been a new focus in biomineralization. However, to date the organic matrix has not received sufficient qualitative attention. The detailed structure of the organic matrix, the amino acid sequence and its functions still require further work. However, according to EDTA studies, some data are known. The organic matrix weighs less than 5 wt. % and can be divided into two general groups: the insoluble matrix (IM) and the soluble matrix (SM) (*Weiner and Addadi*, 1997; *Marxen et al.*, 1998). The IM, which consists of chitin, silk proteins and other hydrophobic molecules, is the dominant part of the organic matrix. The prominent compositions of the SM are glycoproteins, phosphoprotein and sulphated polysaccharide, which are the main regulators of the biomineralization process (*Sikes and Wheeler*, 1988)

The regulation or control of the biomineralization process by the organic matrix has been discussed in several previous studies. The first important role of organic matrix lies in regulating the shapes of biominerals. In the geological process, calcite crystallites tend to take the forms of rhombohedra or prismatic shape with scalenohedral faces; the (104)-plane is the most stable surface of calcite; the aragonite crystallites usually form a columnar or acicular shape and the (010)-plane is the most stable surface (*de Leeuw and Parker*, 1998). In contrast to geological crystals, the shapes of biominerals can differ drastically from geological minerals. Fig. 1.2 shows the cross section of the calcitic prismatic layer in *Atrina pectinata* shell (*Suzuki et al.* 1981) and the aragonitic nacreous layer in *Margaritifera margaritifera* (*Liao et al.*, 2000).

1.1 Biominerals and biomineralization

Both layers had been decalcified with EDTA and the organic frameworks are exposed and examined under scanning electron microscope (SEM). In Fig. 1.2a, the framework shows that calcite crystallites form polygonal columns, which are separated by organic walls. Fig. 1.2b shows that aragonite crystallites form lamellae separated by organic sheets. Both biominerals have composite structures and their shapes of crystallites clearly distinguish themselves from geological calcite or aragonite.

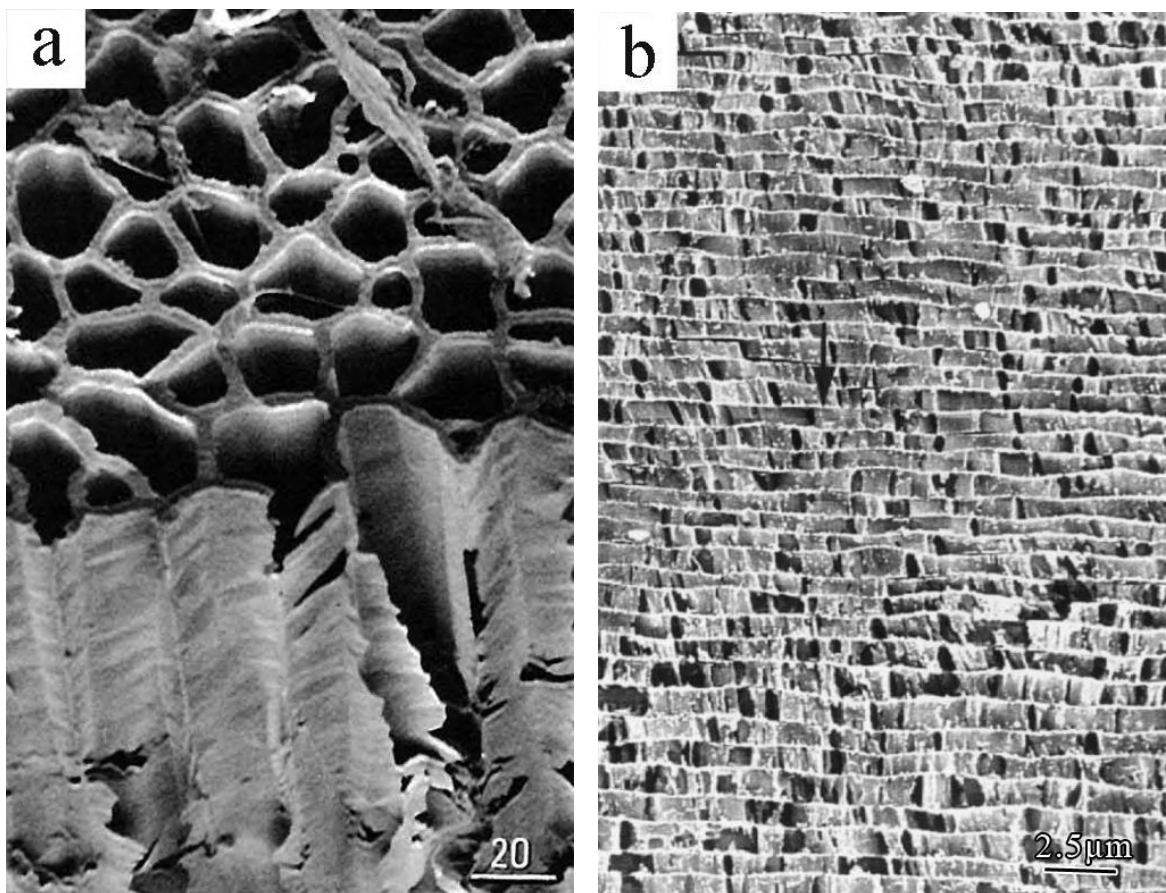


Fig. 1.2 (a) SEM image of the interprismatic organic matrix of calcitic prisms of *Atrina pectinata* (Suzuki and Uozumi, 1981). (b) SEM image of the interlamellar organic matrix of aragonitic nacre of *Margaritifera margaritifera* (Liao et al., 2000).

The second role of the organic matrix in biomineralization lies in the selective nucleation of different calcium carbonate polymorphs. Several in vitro studies have shown that calcium carbonate will deposit in different mineral phases when different organic matrices are added to the saturated solution (Belcher et al., 1996; Falini et al., 1996). When SM is extracted from an aragonitic shell and added to the solution with a substrate of chitin and silk fibroin, aragonite

crystallizes at room temperature and when SM from the calcitic shell layer is induced jointly with a substrate of IM, calcite is formed. However, when there is no IM substrate in the solution, no aragonite is formed regardless of the SM from aragonitic or calcitic shell layers. The results show that in mollusc shells, both IM and SM contribute to the crystallization of different polymorphs and SM is the main determinant. Hence, one or more macromolecules are involved in the polymorphic determination, but the exact composite that induces the determination needs greater isolation and characterization.

Furthermore, the organic matrix may also affect the co-orientation of crystallites. The consistent orientation of one or more crystallographic axes has been found in many biominerals. For example, the *c*-axis of calcite crystallites in the herringbone units of the red coral *Corallium rubrum* is arranged in two main directions (Vielzeuf *et al.*, 2010), and the *c*-axis of calcite crystallites in the spine of sea urchin *Paracentrotus lividus* is co-orientated along the long axis of the spine. Several previous studies have brought up theories about this co-orientation phenomenon. After studying the structure of macromolecules extracted from molluscs, it was proposed that calcium ions are regularly bound to the IM surface (Weiner *et al.*, 1984), which adopts the antiparallel β -chitin conformation and contains acidic proteins. The chitin fibres and the protein polypeptide chains are oriented perpendicular to each other and parallel to the *a*- and *b*-axis of aragonite. Thus, they form the template for the growth of co-oriented aragonite crystallites. Fig. 1.3 shows an illustration of the possible mode of calcium binding to the surface of β -sheet containing aspartic acid. In vitro studies have also shown that calcium carbonate can deposit in preferred orientations of the crystallographic axis on Langmuir–Blodgett films, which contain one or more monolayers of small organic molecules (Heywood and Mann, 1994; Litvin *et al.*, 1997). Considering the results, how animals control nucleation, crystallization and preferred crystal orientation is a complex process that requires further understanding.

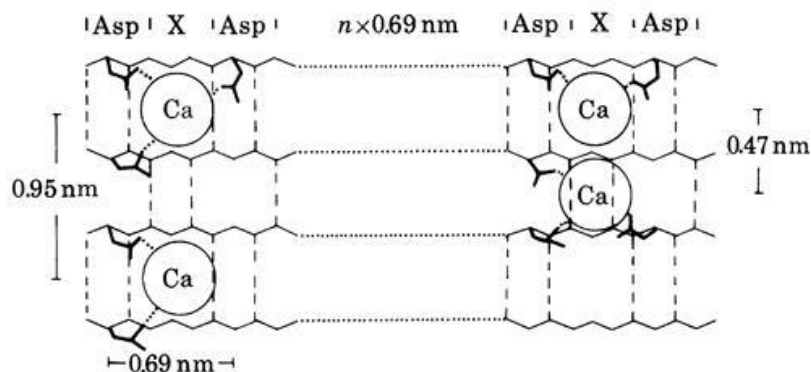


Fig. 1.3 Schematic illustration of possible modes of calcium binding to the surface of a β -sheet containing aspartic acid residues. The calcium ions are bonded to 2 or 3 aspartic acid residues (Weiner *et al.*, 1984).

1.1.3 Studies of biominerals based on EBSD and Raman spectroscopy

Approaches to study the material features of biominerals developed rapidly during the last decades. The morphology of biominerals from macroscopic to nanoscopic scale has been investigated using optical microscope, scanning electron microscope, atomic force microscope (AFM) and transmission electron microscopy (TEM). By applying X-ray powder diffraction (XRD), electron microprobe, nuclear magnetic resonance (NMR) and gas chromatography–mass spectrometry (GC-MS), the chemical compositions of biominerals have been studied from both, organic and inorganic constituents. Because of the development of sensitive local techniques in the last two decades, more advanced technologies have been applied to the study of biominerals, such as electron backscatter diffraction (EBSD) and Raman spectroscopy.

In material sciences, EBSD was at first widely used in analysing the textures of metals and ceramics. Using it in combination with SEM, scientists studied crystallographic and morphologic information on the same surface simultaneously. With the help of EBSD, the grain morphology, orientation and boundaries can be revealed, which are critical to the mechanical properties of polycrystalline materials. EBSD was first applied to biominerals in 2003 (*Ozaki and Kogure, 2003*) to study the coccoliths of marine unicellular algae (*Pleurochrysis carterae*). Fig. 1.4a shows the mesostructure of coccolith. The ring-shaped coccolith is composed of tens of submicron-sized calcite particles. The long and short arrows in Fig. 1.4a indicate directions of the *a*- and *c*-axis of calcite, respectively. The first EBSD study on mollusc shells was conducted in 2004. Results showed that the calcite crystallites in the fibrous layer of a brachiopod shell (*Megerlia truncata*) have a preferred orientation (*Schmahl et al., 2004*). In 2007, EBSD experiments were first processed on the calcitic foliated layer of bivalve shells (*Checa et al., 2007*). The foliated layer, which consists of elongated blade-like crystallites and is unlike the common nacreous and prismatic layer, only exists in certain species. Fig. 1.4b shows the pole figures generated from EBSD measurements of calcite crystallites in a folium. The results show that the *c*-axis of calcite crystallites in both species has preferred orientations which form certain angles with the growth direction of the folia (black double arrows in Fig. 1.4b). Similar preferred orientation of aragonite crystallites in the corals has been reported in 2008 (*Cusack et al., 2008*). Fig. 1.4c shows the cross section of the core of the coral *Porites lutea*. The *c*-axis of most aragonite crystallites is parallel to the long axes of the fibres and radiates from the centre of calcification (COC), except that there is a circular microboring (red colour in Fig. 1.4c), which exhibits *c*-axis orientation perpendicular to the analysis surface. Besides the preferred orientation of certain crystallographic axes, in 2011 another significant

1.1 Biominerals and biomineralization

structure in biominerals was characterized as ‘mesoscale twinning’ (Floquet and Vielzeuf, 2011). A mesocrystal is defined as an assembly of nano- or micrometre-sized crystalline units. A mesotwin is to a twin what a ‘mesocrystal’ is to a crystal—an analogue with defects. Fig. 1.4d shows a cross-shaped sclerite and its pole figures generated by EBSD experiments. The distinguished colours in the sclerite and two groups of poles in Fig. 1.4d confirm that the calcitic sclerite is composed of two adjacent sectors with the c -axis at an angle of about 90° from each other. The overlapping (104) indicates that the two adjacent sectors have a ‘twinning’ relationship. However, the imperfect twinning interface and the polycrystalline character of the two ‘twins’ may prevent the use of the term ‘twin’ in the strict sense. The term ‘mesotwinning’ was therefore adopted to describe the twinning structure of biominerals.

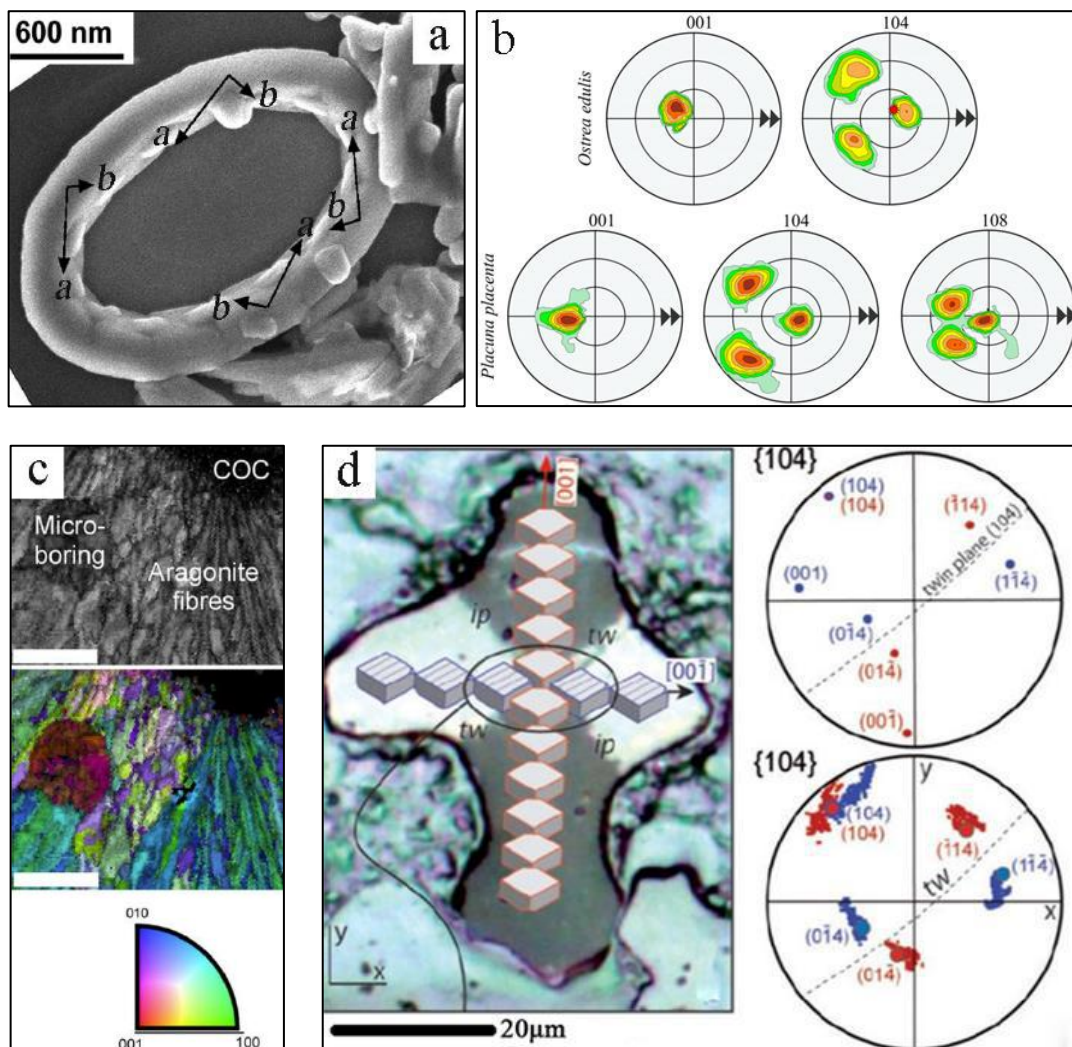


Fig. 1.4 Crystal orientation studies of biominerals based on the EBSD method. (a) First application of EBSD to biominerals shows that the a -axis of calcite crystallites are approximately parallel to the base plane and the c -axis stand by $50 \sim 60^\circ$ from the basal plane (Ozaki and Kogure, 2003). (b) First application of EBSD to bivalves showing that the c -axis and $\{104\}$ of calcite crystallites have preferred orientation. The c -axis tilts backwards and

1.1 Biominerals and biomineralization

the {104} faces forwards to the growth direction (black arrows) (Checa *et al.*, 2007). (c) First EBSD applications to aragonite crystallites of *Porites* coral showing a preferred orientation of the *c*-axis along the fibre axis (Cusack *et al.*, 2008). (d) Schematic arrangement of calcite crystallites in the sclerite of *Corallium rubrum* showing mesoscale twinning where each of the ‘twins’ is polycrystalline (Floquet and Vielzeuf, 2011).

Previous studies of preferred orientation and twinning structures have revealed that the controlled growth of biominerals differs from the abiogenic minerals not only in morphology but also in crystallographic orientation. With the development of EBSD technology, we can obtain the crystal orientation information of biominerals at the scale of 0.1 μm at present. However, EBSD studies still have to deal with several problems. First, EBSD measurements require highly polished surfaces with minimum mechanical deformation of the samples. It requires strict mechanical and chemical polishing processes (see Chapter 2.3), which make in situ tests difficult to proceed. Second, the minor but critical organic component cannot acquire diffraction under SEM. Finally, the studies of EBSD on biominerals are still limited. The majority of earlier studies were processed with low resolution or in a limited local area, possibly omitting secondary or superior structures.

To counteract the weaknesses of EBSD measurements, Raman spectroscopy was introduced into the research of biominerals. As a traditional non-destructive technique in condensed matter physics and chemistry, Raman spectroscopy is a rather new technique applied to biominerals as opposed to infrared spectroscopy. It can be in-situ processed on the surface, and more importantly, organic and inorganic components can be examined at the same time. Studies on biominerals with the help of Raman spectroscopy date back to late 1980s and early 1990s (Urmos *et al.*, 1986; Unvros *et al.*, 1991). Corals and pearls were characterized by different calcium carbonate polymorphs and compared with synthetic calcite and aragonite. Raman spectroscopy mapping was first carried out on the biominerals of plant *Equisetum hyemale* (Gierlinger *et al.*, 2008). On the cross section of different regions, spectral maps show different distributions of hemicelluloses, pectin and silica (see Fig. 1.5a). The Raman spectroscopy imaging technique was applied to molluscs in 2010 (Weaver *et al.*, 2010). The line scanning result shows that from the core to the shell region of a chiton tooth occurs a transition from magnetite to iron phosphate (see Fig. 1.5b). Later, three different polymorphs of calcium carbonates, calcite, aragonite and vaterite were imaged by Raman spectroscopy in a chondrophore area of the bivalve shell *Laternula elliptica* (Nehrke *et al.*, 2012). However, the use of Raman spectroscopy to study the preferred orientation of biominerals has rarely been

1.1 Biominerals and biomineralization

practised. Even until 2011 (Nehrke and Nouet, 2011), unpolarized Raman spectroscopy had been used to describe the distribution of aragonite crystallites with two distinguishable orientations together with calcite and organic compositions in a cross section of the gastropod shell *Nerita undata* (see Fig. 1.5d). With the introduction of polarizers, different vibrational modes in different minerals can be distinguished by using Raman spectroscopy. Based on the polarization features, several studies attempted to explain the theory of using polarized Raman spectroscopy to recognize different crystallographic phases and orientations (Lu, 2009; Munisso et al., 2009; Yang et al., 2010; Carter et al., 2013; ZHANG and GONG, 2013; De La Pierre et al., 2014) . In this work, mappings under both, polarized and unpolarized Raman spectroscopy was done as an attempt to establish a new way to evaluate crystallographic orientations in biominerals (for details, see Chapter 2.4).

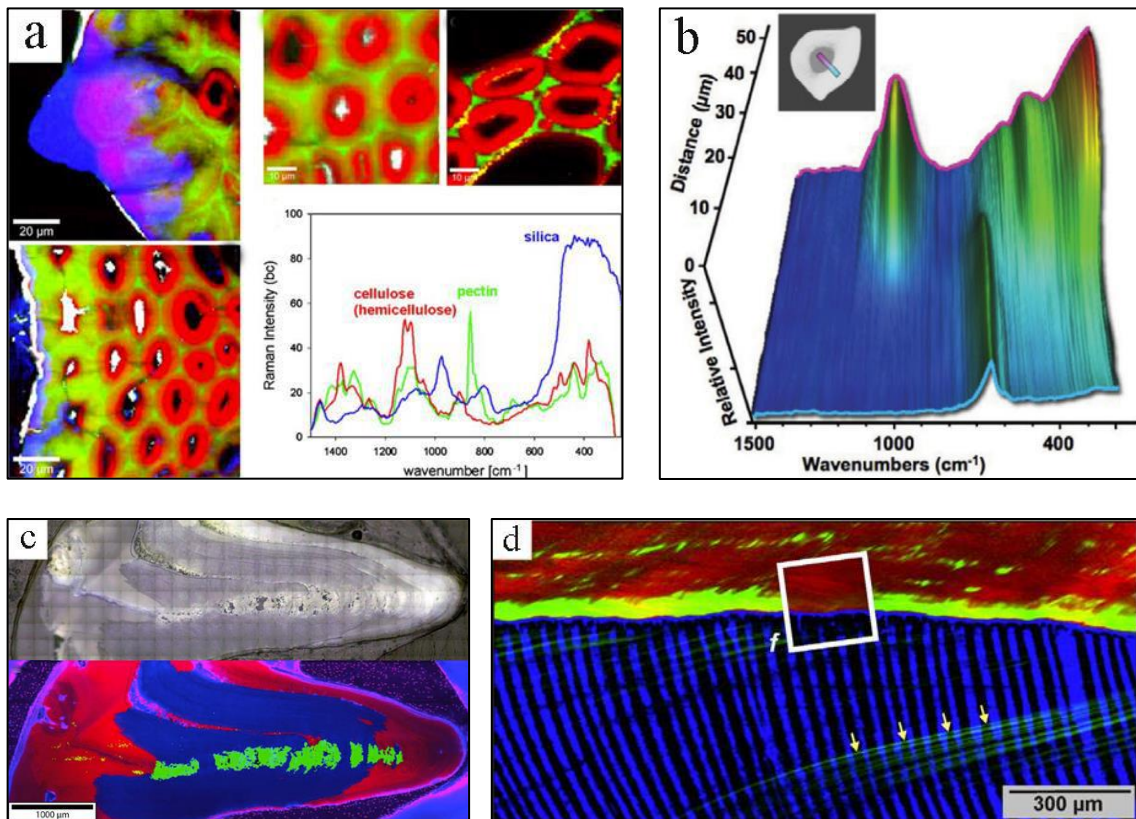


Fig. 1.5 Applications of Raman spectroscopy imaging technique to biominerals. (a) An early Raman spectroscopy mapping operated on the biominerals of *Equisetum hyemale*. It shows the distribution of hemicelluloses (red), pectin (green) and silica (blue) in the cross section of a plant (Gierlinger et al., 2008). (b) A line scanning, which first took place on molluscs, shows a transition of two mineral phases in the teeth of a chiton (Weaver et al., 2010). (c) Raman spectroscopy mapping shows the distribution of calcite (green), aragonite (red) and vaterite (blue) in the chondrophore area of a bivalve shell (Nehrke et al., 2012). (d) Unpolarized Raman spectroscopy mapping reveals two distinguishable orientations (black and blue) of aragonite crystallites in a gastropod shell *Nerita undata* (Nehrke and Nouet, 2011).

1.2 Molluscs

Mollusca is the second-largest animal phylum after insects, and it is also the largest marine phylum. Molluscs are known for their ability to produce shells. The estimated number of the described mollusc species ranges from 34,000 (Boss, 1971) to 120,000 (Ponder *et al.*, 2002). Including undescribed species, there are in total between 47,000 (Boss, 1971) and 200,000 (Chapman, 2009) mollusc species. Most of molluscs share certain common features: a soft body without endoskeleton; a mantle with a cavity which may secrete calcareous shells; the body is not segmented but can be divided into radula (a functioning structure for feeding), muscular foot, visceral mass and other parts. Molluscs of different classes have various morphologies, behaviours and habitats. The phylum can be divided into 9-10 taxonomic classes, including two extinct ones, depending on different definitions. Eight living classes (Haszprunar, 2001) are listed as follows:

1. Gastropoda (snails, slugs, limpets and their kin),
2. Bivalvia (mussels, clams, oysters, scallops and their kin),
3. Cephalopoda (squids, octopuses, nautilus and their kin),
4. Scaphopoda (tusk shells),
5. Solenogastres,
6. Caudofoveata (often combined with Solenogastres as Aplacophoran, shell-less class),
7. Monoplacophora,
8. Polyplacophora (chitons and their kin).

Of the eight classes, Gastropoda is the most abundant as it includes about 80% of the total mollusc species. Except for gastropods, the study of biomineralization also focuses on bivalves, cephalopods and chitons. In this thesis, the measurements and discussion will focus on the comparison of selected species from Bivalvia and Gastropoda.

1.2.1 Bivalvia

The Bivalvia class contains about 7,500 species including animals with two shell valves (Gosling, 2008). This class of species has acquired a wide interest chiefly because it is eaten by humans in large amounts, as well as the economic value of producing pearls.

Members of this class are diverse and abundant. Mostly aquatic, bivalves are found in freshwater, estuarine water and marine environment. They survive at all depths and latitudes, though none of them is planktonic. There are no terrestrial species, though some are able to

tolerate drought situations. Most bivalves are infaunal burrowers. In order to move rapidly into sediments, the shells of some species: For example, *Ensis ensis* are laterally compressed. The edge of the mantle may also have evolved into long siphons in order to feed or breathe, while the body is generally buried in sand, mud or other substrates. Byssally attached species rank second. Some bivalves, such as *Mytilus edulis*, can secrete byssus from their muscular feet to be attached to hard substrates. Boring, nestling, cementing, swimming and reclining are other forms of locomotion attachments of bivalves (Stanley, 1970; Morton, 1996).

The taxonomy of bivalves is based on gills, stomachs, labial palps, shell structures and other characteristics. The class can be divided into six major subclasses gives below (Newell, 1965):

1. Pteriomorpha, a subclass that possesses mostly duplivincular grade of ligament, epifaunal habit and throughout life byssus,
2. Palaeoheterodonta, a subclass that has free or incompletely fused mantle margin, a parivincular ligament,
3. Palaeotaxodonta, a compact subclass characterized by a primitive taxodont hinge and protobranch ctenidia,
4. Cryptodonta, a not well understood, thin-shelled subclass without well-developed hinge,
5. Heterodonta, a subclass that possesses no nacles and more or less fused, siphonate mantle margins,
6. Anomalodesmata, a siphonate burrowing form with prismatic-nacreous shells, possessing an internal resilium, chondrophores and a lithodesma.

Different subclasses of bivalves differ from each other in shapes and sizes. Nonetheless, all of them have two mantle lobes that secrete two shell valves, hinged dorsally by a flexible ligament, covering the organ mass (Gosling, 2008) (see the transverse and longitudinal section of a bivalve in Fig. 1.6). The shell opens and closes the two valves by using two muscles— anterior and posterior adductors. There is a wedge-shaped muscular foot in the cavity formed by the mantle for the purpose of locomotion. Other than containing the organs, the cavity could also be used for brooding, respiration and locomotion (for example the scallops).

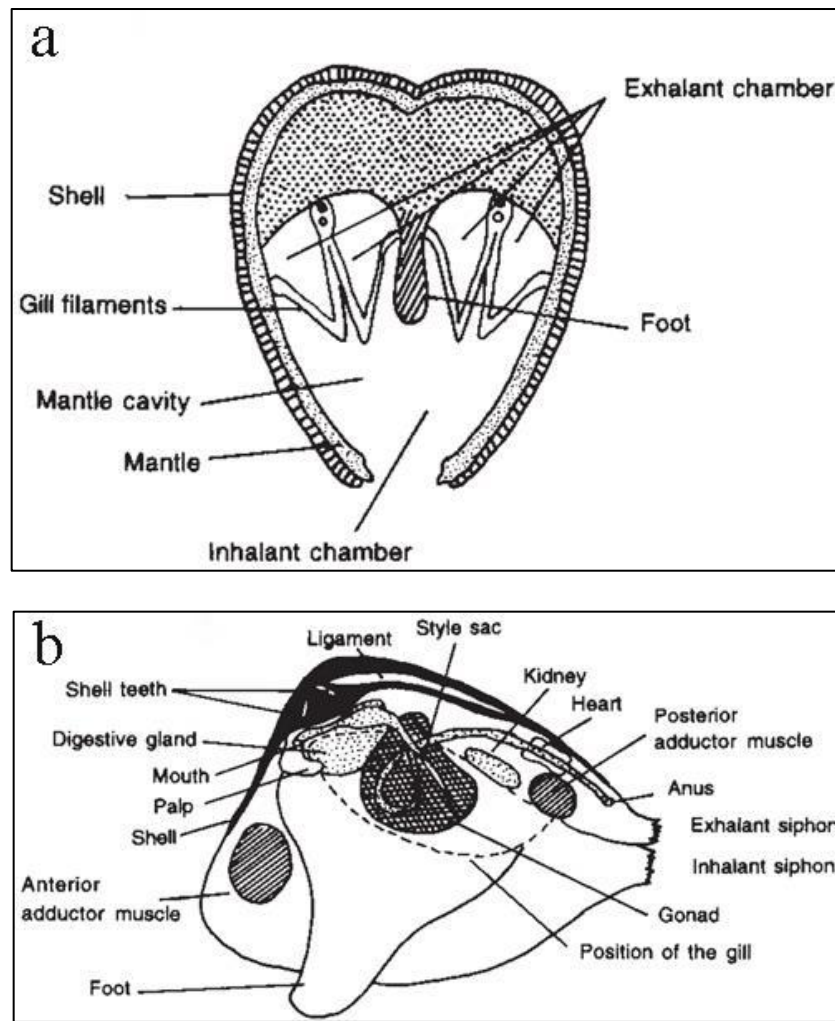


Fig. 1.6 Illustrations of the structure of a bivalve from transverse and longitudinal view. (a) Transverse section shows the position of mantle, foot and gills. (b) Longitudinal section shows the major organs (Gosling, 2008).

The mantle (also known as pallium) is a significant thin tissue related to biomineralization. The margin of mantle is attached to the open edge of shell valves and is thrown into three folds (see Fig. 1.7). The one next to the shell is considered with the secretion of the periostracum layer and outer shell layer (C fold in Fig. 1.7); a middle one has a sensory function (B fold in Fig. 1.7); and an inner muscular fold controls the water flow in the mantle cavity (A fold in Fig. 1.7) (Yonge, 1982; Gosling, 2008). Between the outer surface of the mantle and the shell is a minute space filled with extrapallial fluid (see Fig. 1.7), which contains the essential compositions for calcification.

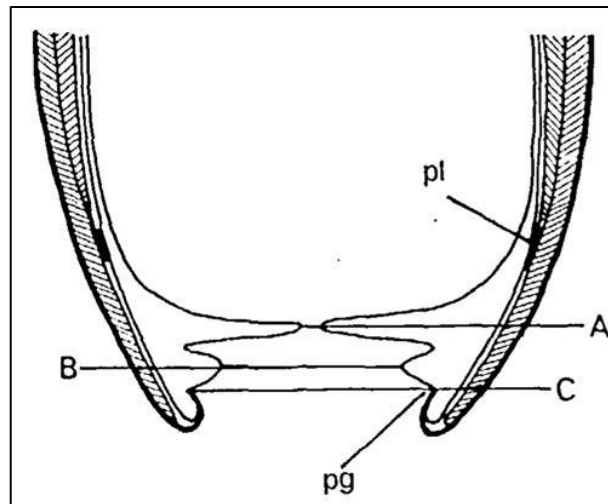


Fig. 1.7 Schematic illustration showing the mantle margin of a bivalve in transverse view. (a) Inner fold of the margin that controls the water flow in the cavity. (b) A middle fold has a sensory function. (c) An outer fold secretes periostracum and the outer shell layer. Pl: pallial line. It separates the shell area where the margin is attached and the area where there is extrapallial fluid existing between the mantle and the shell. Pg: periostracal groove, where periostracum is secreted (Yonge, 1982).

1.2.2 Gastropoda

With more than 80,000 species (Bouchet *et al.*, 2005), gastropods are the largest group of the phylum mollusc. The class includes snails, slugs, limpets, conches and other common names. Several species, such as abalone, river snails and limpets are consumed by people as food. The shells of some species, such as the abalone shells, are used as parts of jewellery or decorations like inlays in furniture and buildings.

Used by George Baron Cuvier, the word ‘gastropod’ derives from the Greek words for stomach and foot (Chase, 2002). Molluscs belonging to this class appear to crawl ventrally on their ‘bellies’, which in humans generally contains internal organs. However, it is not anatomically comparable since the digestive organs of gastropods are mostly situated dorsally.

Different from bivalves, gastropods are diversely distributed in freshwater, marine and terrestrial habitats (Vermeij and Signor, 1992; Strong *et al.*, 2008). They are found at all altitudes and depths, including planktonic swimmers. The great majority of gastropods move by crawling with the contraction of their muscular foot or the beating of cilia (Chase, 2002). Other than crawling, a remodelling of the foot into paddles or wings also allows some shell-less species to swim.

Based on morphological characteristics, gastropoda can be divided into three subclasses: prosobranchia, opisthobranchia and pulmonata (*Chase, 2002*). However, more developed anatomical and molecular characteristics have given new insights into the taxonomy of gastropods. Many points in the traditional classification are controversial. Based on old classifications and new cladistics studies, a recent classification of living gastropods is as follows (*Bouchet et al., 2017*):

1. Patellogastropoda, known as true limpets, a major marine subclass with flattened cap-shape shells,
2. Neophaliones, a new deep-sea subclass with only two orders,
3. Vetigastropoda, a subclass characterized by having intersected crossed platy shell structure (*Hedegaard, 1997*), ctenidial sense organs (so-called bursicles), epipodial sense organs and the special structure of the ocsophagus,
4. Neritimorpha, a diverse subclass characterized by concatenated genome sequences evolved with snails, slug- and limpet-like gastropods in different living habitats,
5. Caenogastropoda, a large and diverse subclass that comprises about 60% of living gastropod species. They have aragonitic crossed-lamellar shells (*Bandel, 1990*), multispiral and orthostrophic protoconchs and a heart with a single auricle (*Ponder et al., 2008*),
6. Heterobranchia, a subclass with heterostrophic protoconchs and columella lamellae (*Haszprunar, 1985*).

Due to the diversity of this class, it is hard to define overall characteristic features of morphology. Nonetheless, the only common feature of the gastropoda class is their body torsion (*Bandel, 1997*). Torsion is a process that happens at the larva (veliger) stage before the gastropods become juvenile. Fig 1.8 shows the process of torsion and the terms of the soft parts of a gastropod from dorsal and lateral views.

1.2 Molluscs

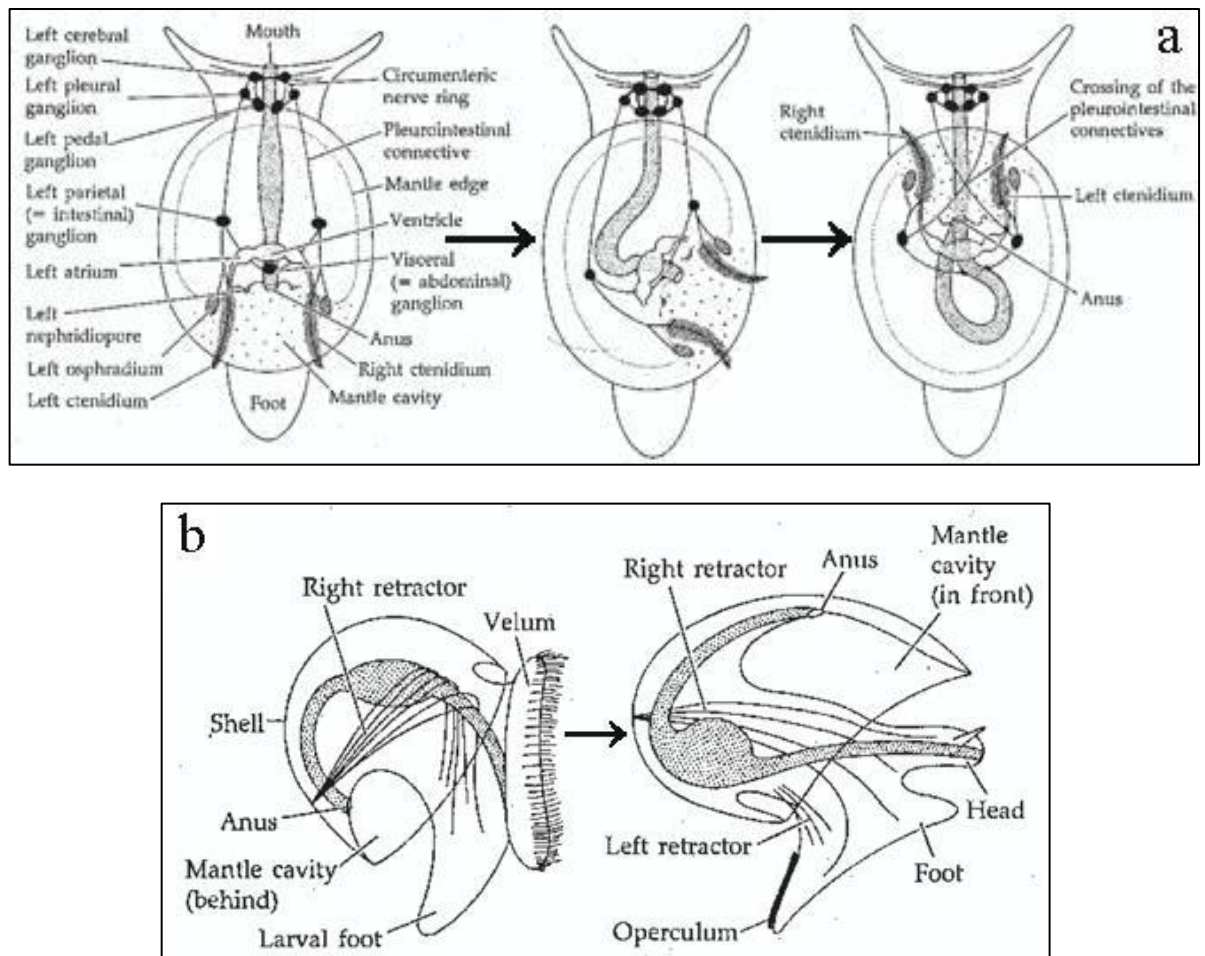


Fig 1.8 Illustrated process of torsion in gastropods (Prothero, 2013). (a) Dorsal view of a hypothetical untorted gastropod and gastropods after torsion. The mantle cavity, gills, anus and nephridiopores move from a posterior to an anterior position. (b) Lateral view of a veliger larva before and after torsion.

After the torsion is completed, the visceral mass is placed in the mantle cavity over the head. The nerve cord is twisted, the positions of the left and right gills are reversed and the anus is located from the posterior position to the anterior position.

When the larva becomes juvenile, the mantle of species with shells starts to secrete teleoconch after the protoconch, which is the primitive part of the whole shell and has a sculpture different from the teleoconch. The forms of gastropod shells vary largely from species to species. The most common form of a gastropod shell is a cone coiling around an axis in a corkscrew fashion. The mantle is fully or partially hidden inside the helical shell. In some species, there is an operculum attached on the surface of the muscular foot for the animal to close the aperture when they retract the outer body into the shell. The operculum is either corneous or calcareous. Fig 1.9 shows a structure of a gastropod shell.

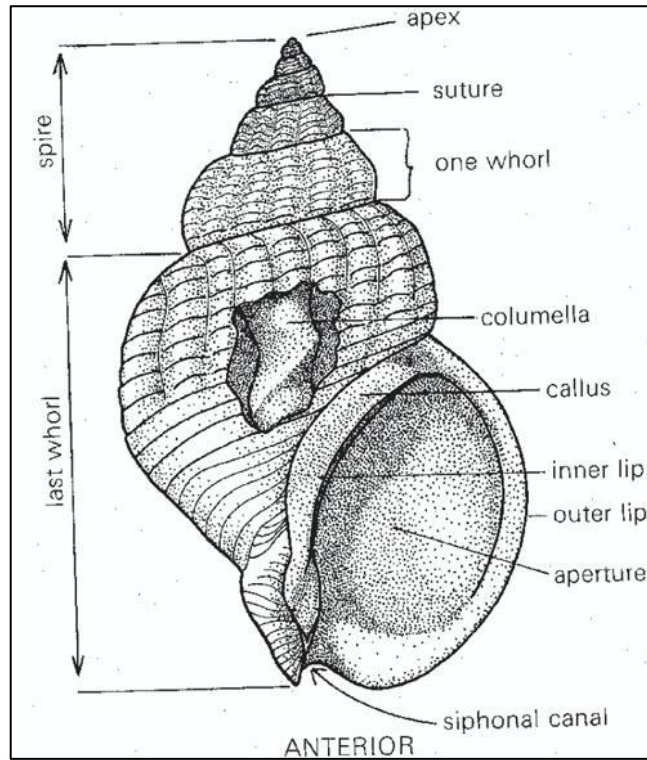


Fig 1.9 Structure of a dextral gastropod shell. The apex is usually the protoconch or abraded. Sutures are the places where two whorls joined. The columella is the central pillar in a coiled shell formed by the fusion of the inner walls of the whorls. The columella could be a solid or hollow structure depending on the species (Prothero, 2013).

1.3 Calcium carbonates

Calcium carbonate is one of the most abundant minerals of the earth crust. It has in addition only been found on Mars (*Boynton et al.*, 2009). Carbonates are generally products of aqueous processes, and are closely related to the global deep carbon circle (*Park et al.*, 1996) and activities of living species (*Spero et al.*, 1997). Thus, they have been extensively studied in various fields, including geochemistry, biology and mineralogy.

Calcium carbonates are compounds with the general formula of CaCO_3 . The carbonate group is trigonal planar with carbon lying at the centre and three oxygen atoms at the corners of the triangle (*DeVol et al.*, 2014). In nature occur three anhydrous polymorphs of calcium carbonate forms: calcite, aragonite and vaterite; two hydrated modifications: calcium carbonate monohydrate and calcium carbonate hexahydrate; and amorphous calcium carbonate (*Perić et al.*, 1996). Among the polymorphs, only calcite and aragonite are thermodynamically stable (*Mann*, 2001). Vaterite is a metastable form of calcium carbonate and changes into calcite irreversibly at a temperature of 730K (*Perić et al.*, 1996). It is found in limited quantity in natural environment and mainly in biominerals (*Lowenstam and Abbott*, 1975; *Gauldie et al.*, 1997; *Berland et al.*, 2013). Monohydrocalcite is also less stable and has been found in biominerals (*Lowenstam*, 1989; *Señorale-Pose et al.*, 2008). Calcium carbonate hexahydrate, also known as ikaite, has not yet been found in biominerals. The amorphous calcium carbonate (ACC) observed in biominerals is considered to be the transient precursor of aragonite or calcite (*Addadi et al.*, 2003). In the present work, the mineralogical studies will focus on calcite and aragonite.

1.3.1 Calcite

Calcite is the most stable polymorph of calcium carbonate (*Perić et al.*, 1996). It is a common mineral with various forms and colours constituting the major element of many rocks. The recognizable characteristics of calcite is its Mohs hardness of three and high maximum birefringence of 0.174 (*Oldenbourg*, 2008).

In nature, calcite usually forms rhombohedral or scalenohedral crystals in tabular, acicular, prismatic or needle-like shapes (*Kirov et al.*, 1972). Calcite has trigonal point group and space group $R\bar{3}c$. The lattice parameters of calcite are $a=4.9911 \text{ \AA}$, $c=17.0622 \text{ \AA}$, $\alpha=90^\circ$, $\gamma=120^\circ$ (*Pilati et al.*, 1998). Fig. 1.10 shows the crystal structure of calcite. The structure consists of alternating layers of Ca^{2+} and CO_3^{2-} groups that are perpendicular to the c axis. Carbonate groups

within one layer have identical orientations and alternate layers of CO_3^{2-} groups are rotated by 180° with respect to the layer above or below (Gorr, 1992). Four twinning structures of calcite have been found on {012}, {001}, {104} and {018}, of which {012} is the most common twin plane (Bruno *et al.*, 2010).

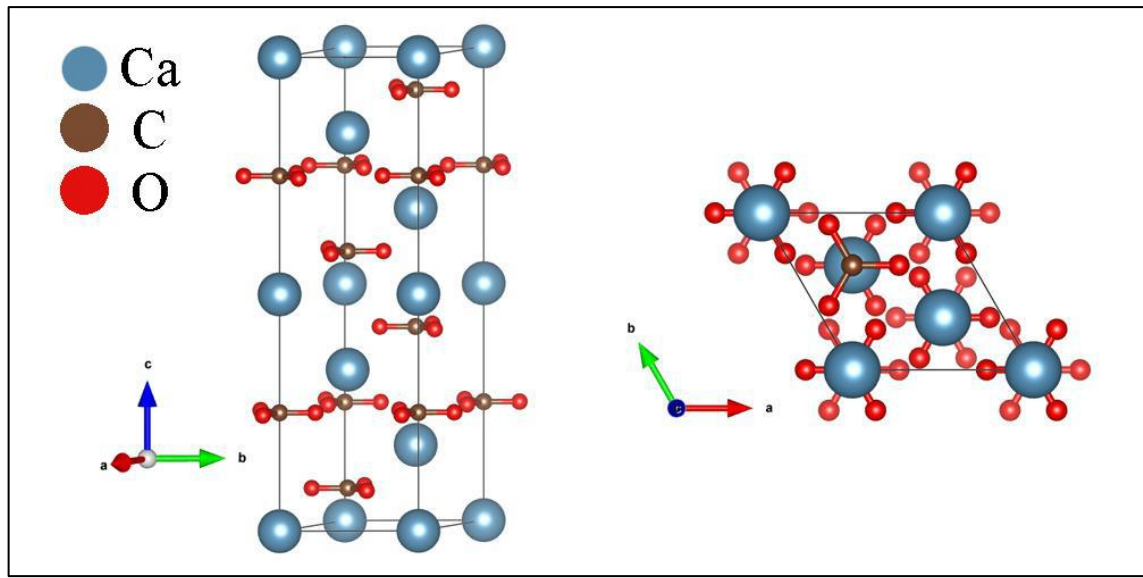


Fig. 1.10 Schematic illustration of the primitive cell of calcite from two viewing directions. Figures depicted using software VESTA.

1.3.2 Aragonite

Aragonite is not as abundant as calcite, but it is a main constituent of biominerals and marine carbonate sediments. Under atmospheric pressures, aragonite is thermodynamically less stable than calcite and transforms into calcite irreversibly after being heated at the temperature of 675.9 K (Perić *et al.*, 1996). Calcite can also convert into aragonite at room temperature under 2.94 kPa of pressure (Lippmann, 1973).

In abiogenic environment, aragonite may have fibrous, acicular, prismatic shapes or bladed crystal with tabular terminations (Perrin *et al.*, 2014). Aragonite belongs to the orthorhombic system with space group of $Pmcn$. The lattice parameters of aragonite are $a=4.9611 \text{ \AA}$, $b=7.9672 \text{ \AA}$, $c=5.7407 \text{ \AA}$, $\alpha=\beta=\gamma=90^\circ$ (Pilati *et al.*, 1998). Fig. 1.11 shows the crystal structure of aragonite. Similar to calcite, the Ca-ions are grouped in layers perpendicular to the c -axis. They are arranged in the so-called distorted hexagonal close packing. Nonetheless, unlike the carbonate groups in calcite which are located in one plane, the carbonate groups in

1.3 Calcium carbonate

aragonite are non-planar. The carbon atoms lie slightly displaced out of the plane of oxygen atoms. Besides, different carbon atoms along the c -axis do not project on top of each other (see Fig. 1.11a right). They are displayed relative to each other along the b -axis (*Schaeffer*). Owing to the distorted hexagonal close packing of Ca^{2+} , the aragonite crystals have a very common twinning structure along the c -axis on the (110) -plane (see Fig. 1.11c) and twinning usually causes pseudohexagonal-shaped triplets in natural environment. The angle between two a - or b -axes is 63.8° instead of 60° (*Bragg, 1924*).

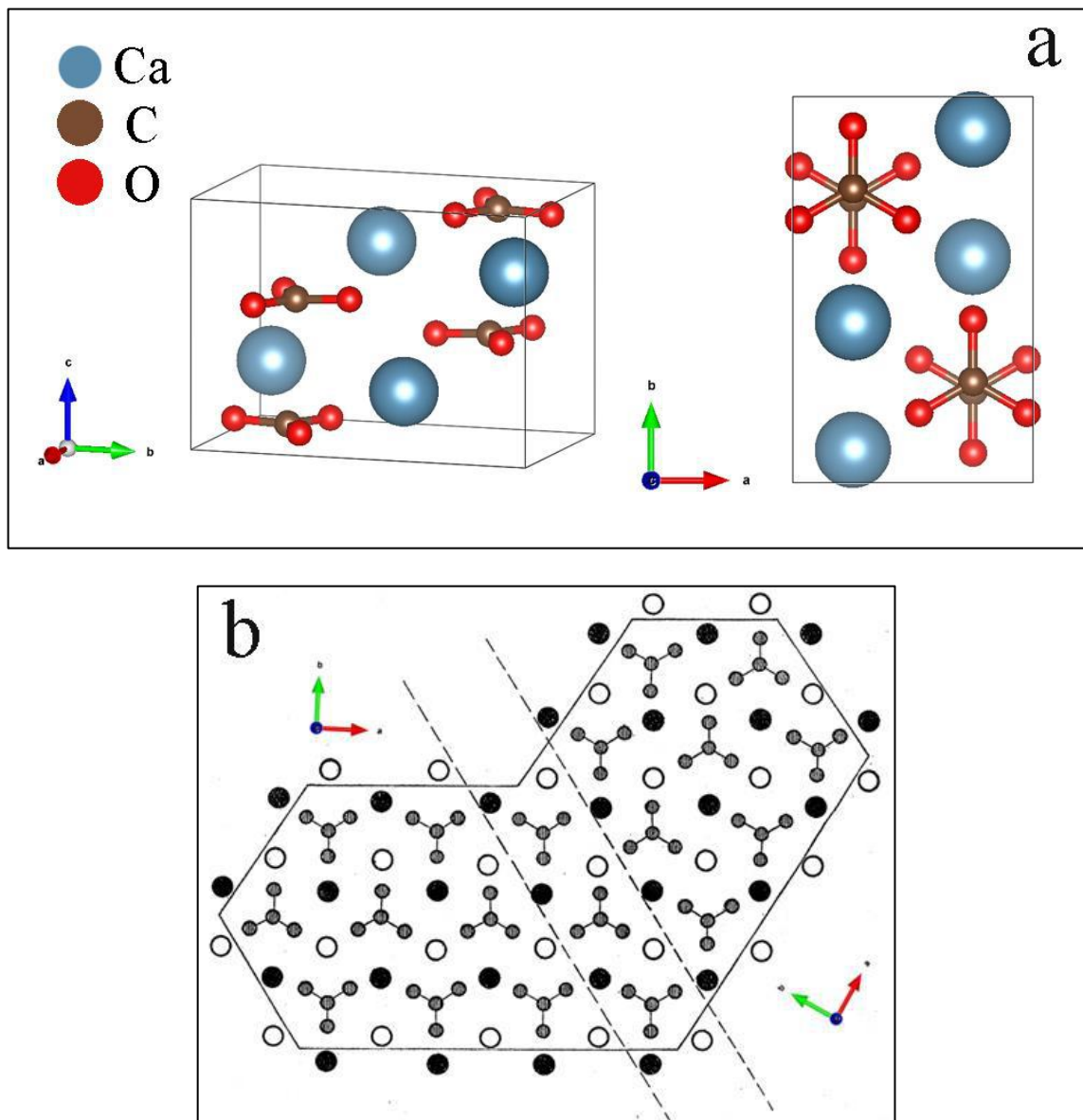


Fig. 1.11 Schematic illustrations of atomic structures of aragonite and aragonite twins on $\{110\}$. (a) The primitive cell of aragonite from two viewing directions. Figures are prepared using software VESTA. (b) Schematic structure of an aragonite twinning on (110) , viewing along the c -axis. The section between the dotted lines can serve as origin or seed for the growth of either crystal on each side of it (*Bragg, 1924*).

2 Materials and methods

2.1 Samples and sample preparation

For the comparison of topological studies between different types of molluscs, three species: *Pinctada fucata*, *Anodonta cygnea*, *Phorcus turbinatus* were selected based on their different living habits and different economic importance.

Specimens of *Pinctada fucata* were obtained from a pearl farm in Beihai, China. *Pinctada fucata* is one of the most widely cultivated species in China and Japan. The species has important economic value in producing pearls. It belongs to the subclass of Pteriomorphia (class Bivalvia), and lives in seawater distributed mostly between the Tropic of Cancer and the Tropic of Capricorn in the Indo–Pacific region and is found in the shallow littoral zone (*Southgate and Lucas, 2011*). Fig. 2.1 shows the morphology of *Pinctada fucata* on a macroscopic scale.

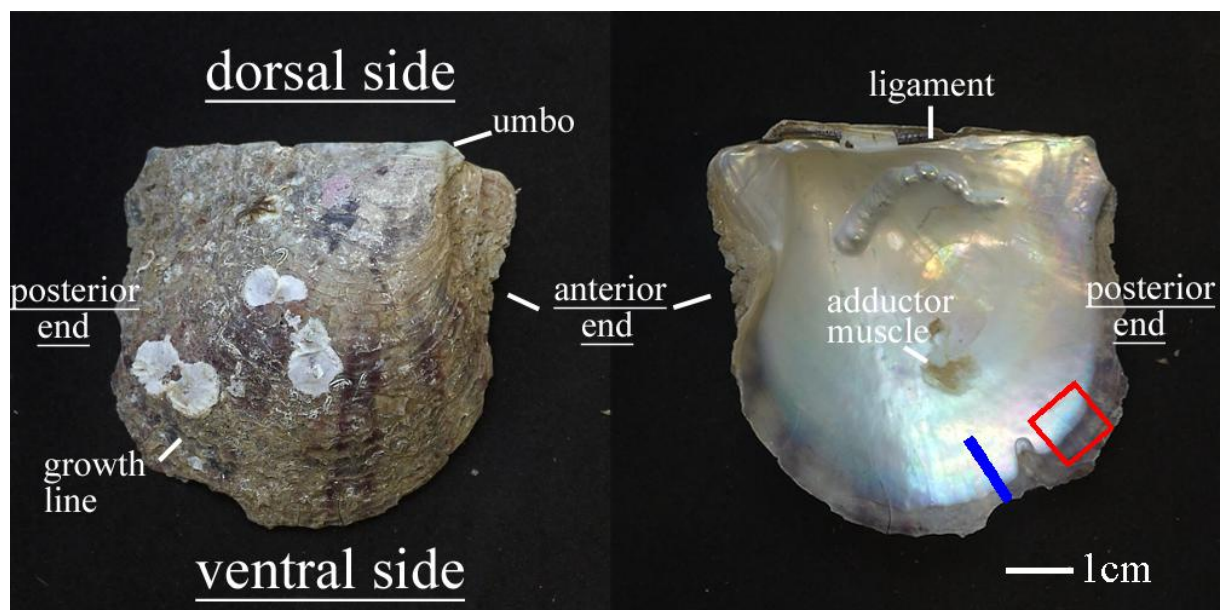


Fig. 2.1 The terminology and morphology of a *Pinctada fucata* shell.

Specimens of *Anodonta cygnea* were chosen from the collections of Prof. Klaus Bandel (Institute for Geology of the Universität Hamburg), collected in Astrakhan, Russia. *Anodonta cygnea* belongs to the subclass of Palaeoheterodonta (class Bivalvia). It lives in fresh water distributed commonly across Europe. *Anodonta cygnea* prefers wide ponds or slow-flowing rivers with high concentration of dissolved oxygen and avoids silted water bodies with overgrown floating vegetation (*Zajac, 2002*). Fig. 2.2 shows the morphology of *Anodonta cygnea*.

2.1 Samples and sample preparation

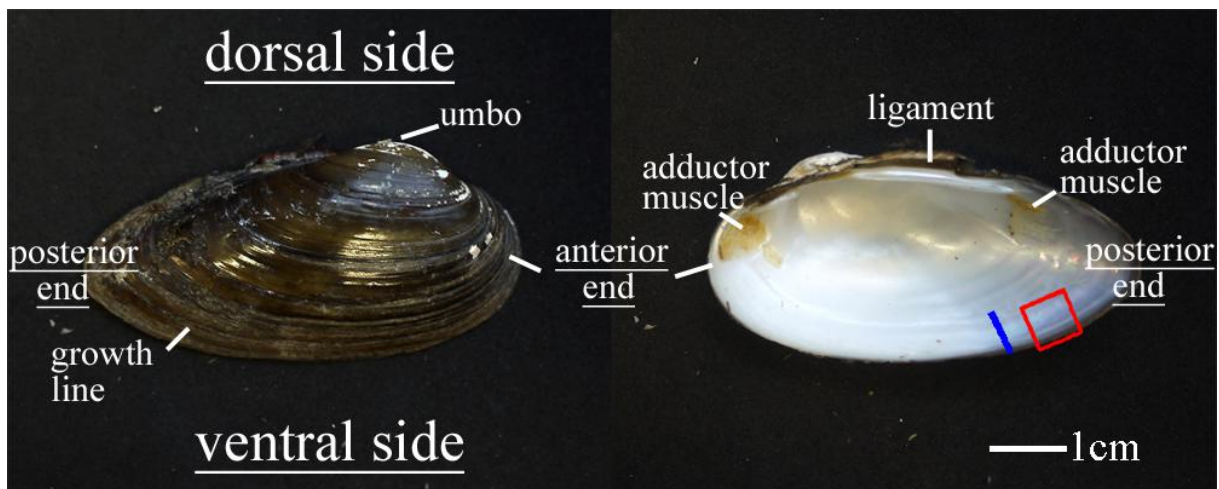


Fig. 2.2 The terminology and morphology of an *Anodonta cygnea* shell.

Specimens of *Phorcus turbinatus* were also chosen from the collections of Prof. Klaus Bandel and they were collected in Banyuls, France. This species belongs to the subclass Vetigastropoda (class Gastropoda) and lives in the Mediterranean Sea. It has been used as a biomonitor for indication of trace metal pollution (Campanella *et al.*, 2001; Conti and Cecchetti, 2003). *Phorcus turbinatus* could be found in the lower midlittoral zone. Comparing to the *Pinctada fucata* living in the shallow littoral zone, *Phorcus turbinatus* is less exposed to a wider range of environmental parameters, e.g. temperature, salinity and desiccation, which are caused by tidal changes and ambient conditions (Menzies *et al.*, 1992). Fig. 2.3 shows the mesoscopic morphology of *Phorcus turbinatus*.

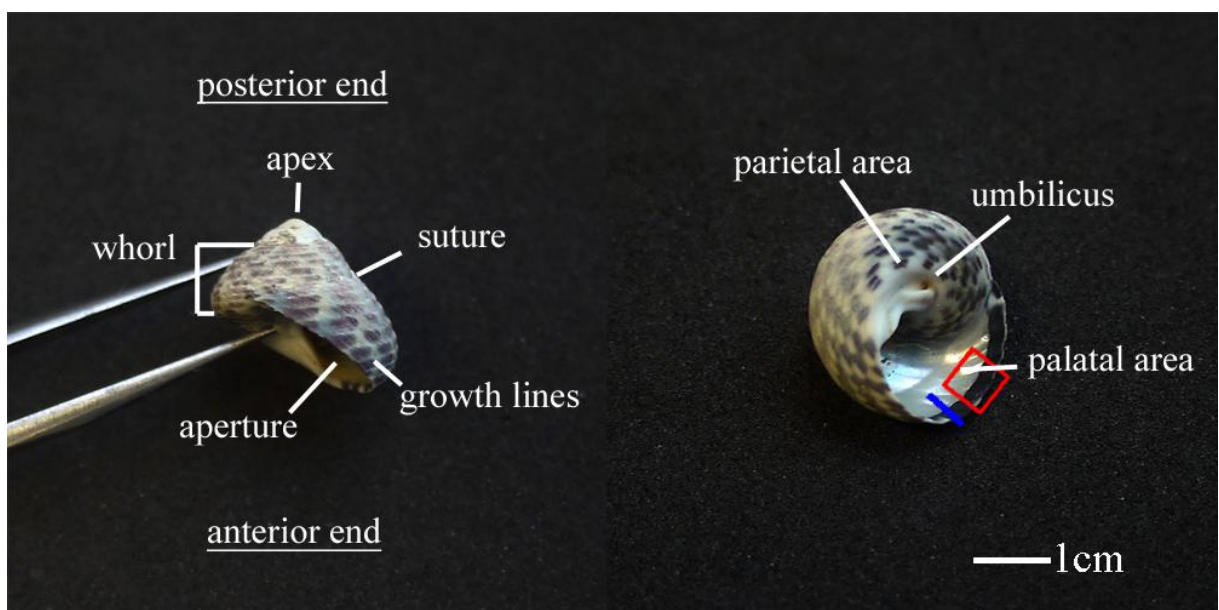


Fig. 2.3 The terminology and morphology of a *Phorcus turbinatus* shell.

Sample preparation for SEM

For SEM measurements, two types of surfaces were selected from the rim of shells. The first type of surface was cut from the original inner surface as a lateral section at the posterior or anterior end of the three shells (see red squares in figs. 2.1, 2.2 and 2.3). The second type of surface is the cross section at the posterior or anterior end of three shells by fracturing the shells (see blue lines in figs. 2.1, 2.2 and 2.3). Both surfaces were then cleaned in 3% peroxide for 48h and dried at room temperature. All samples remained unpolished. Samples were then coated with carbon and photographed with a scanning electron microscope (Zeiss LEO 1455VP SEM).

Sample preparation for EBSD and electron microprobe

For EBSD analysis, sample preparation is crucial to the results. The EBSD patterns are generated within a small diffraction volume located at the surface of a sample with a penetration depth less than 50-100 nm (Nowell *et al.*, 2005) (see Chapter 2.3 for details about EBSD technique). The EBSD pattern quality is extremely sensitive to the perfection of the crystallographic lattice order at the surface of the sample, especially when dealing with shells, which are thin, fragile and containing mixed organic-inorganic phases compared with geological or metallic materials. The surface should avoid any oxidations, contaminations, scratches and the crystallographic deformations should be reduced as much as possible. A brief record of the preparation process is given as follows:

Lateral sections (area of 1 cm × 1 cm) and cross sections (length of 1 cm) from the same positions were selected and cut with a wire saw. All cuts were then mounted with epoxy in small moulds and evacuated for 24 hours.

The moulded samples were then taken out and the epoxy left on the to-be-measured surface was carefully removed by grinding with silicon carbide abrasive paper manually (size P600). After moderate grinding, the surface was treated using a standard cleaning procedure in the sequence of using tap water, water with neutral detergent, tap water and purified water. Samples were then mildly dried with a hairdryer. The surface quality was controlled under the optical microscope. After the surface was exposed, it was then grinded using silicon carbide abrasive paper with the size P1200 automatically until a few straight scratches in one direction were left on the surface.

2.1 Samples and sample preparation

Since the samples were placed in the SEM sample chamber with 70 degrees to the upright incident electron beam, the space was very limited to get optimized diffraction quality, the size of the sample was reduced and shaped approximately to 2.5 cm long, 1.5 cm wide, and 3mm thick by cutting, grinding and cleaning.

The polishing procedure followed after shaping the samples. First, samples were polished automatically on a hard cloth with 3 μm diamond suspension. Samples were turned into different directions several times during polishing. During polishing, the surface was cleaned and checked several times until there were no scratches on the surface. Since minor deformation still remained at the surface after mechanical preparation, a Buehler VibroMet 2 vibratory polisher with 0.05 μm alumina polishing suspension was applied for three hours for final polishing.

After being cleaned and dried from the polishing procedures, silver paste as an extra conductive medium was pasted around the samples to minimize any drift or charging. Finally, the samples were coated with 4 nm carbon in the Leica EM ACE600 for half an hour.

After EBSD measurements, the samples were underwent Electron microprobe analyses at the same positions.

Sample preparation for Raman spectroscopy

A single-crystal of pure aragonite (1.5 cm \times 1.5 cm \times 2 cm) was used as a reference. Three faces perpendicular to the three principle axes of aragonite were cut and polished.

For the Raman spectroscopy mapping, a lateral section from the posterior area of *Anodonta cygnea* shell was cut and polished (see Fig. 2.2).

2.2 Scanning electron microscopy (SEM)

Scanning electron microscopy is a method for studying the surface topography of solid samples by scanning the surface with an electron beam.

The electron beam is usually produced by a thermal emission source, such as a heated tungsten filament. Electrons generated in this way are called primary electrons. They are driven through a vertical and evacuated column and then focused by electromagnetic lenses on the surface of a sample. When the primary electrons strike the surface, various charged particles and photons can be generated through a wide range of interactions (see Fig. 2.4) (Stokes, 2008). These emitted signals are related to the chemical compositions or crystal structure of the sample. They are emitted in different angles and can be collected for morphological, chemical and structural studies.

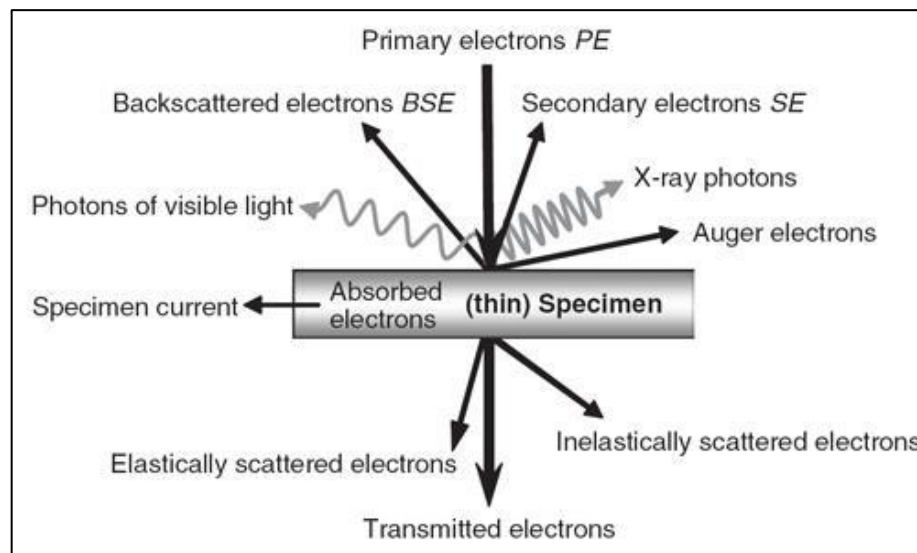


Fig. 2.4 Signals generated by the strike of primary electrons on the specimen (Stokes, 2008).

Secondary electrons are the principal signal for acquiring topographical information. They mostly have weak energy lower than 10 eV and are emitted from a few nanometres of the surface. The yield of secondary electrons increases with decreasing angle between the beam and the sample surface. This so-called 'edge effect' results in a three-dimensional image of contrast due to the uneven features of the surface (Reed, 2005). Samples of three shells were coated with carbon and photographed using a scanning electron microscope (Zeiss LEO 1455VP SEM) at the Institute for Geology at Universität Hamburg.

2.3 Electron backscatter diffraction

Electron backscatter diffraction is a technique that gives crystallographic information about the microstructure of a sample, and it is an extension of the SEM device.

When primary electrons strike the surface of the sample, they are scattered inelastically from the surface after penetrating it less than 100 nm deep (Wisniewski and Rüssel, 2016). Some of the electrons are scattered through the lattice planes at angles that satisfy the Bragg equation:

$$n\lambda = 2d \sin \theta \quad (2.1)$$

where n is an integer, λ is the wavelength of the electrons, d is the spacing of the diffraction plane and θ is the incident and scattering angle of electrons at the surface.

At the measured point, these scattered electrons form one set of paired large-angle cones if the material is finely crystallized. Each pair of cones corresponds to one diffracting plane. The cone pair made of scattered electrons can be collected by phosphor screen and forms two hyperbolic lines, which are called Kikuchi band (see Fig. 2.5a). A set of Kikuchi bands is called Kikuchi pattern or electron backscatter pattern (EBSP) (see Fig. 2.5b). Each Kikuchi band can be indexed with Miller indices and the intersections of the Kikuchi Bands correspond to the axes of the crystal. Based on different crystal structures and orientations of the crystal, the angles and width in the Kikuchi pattern are characteristic. EBSD is therefore a sensitive tool for the identification of phases and crystal orientations.

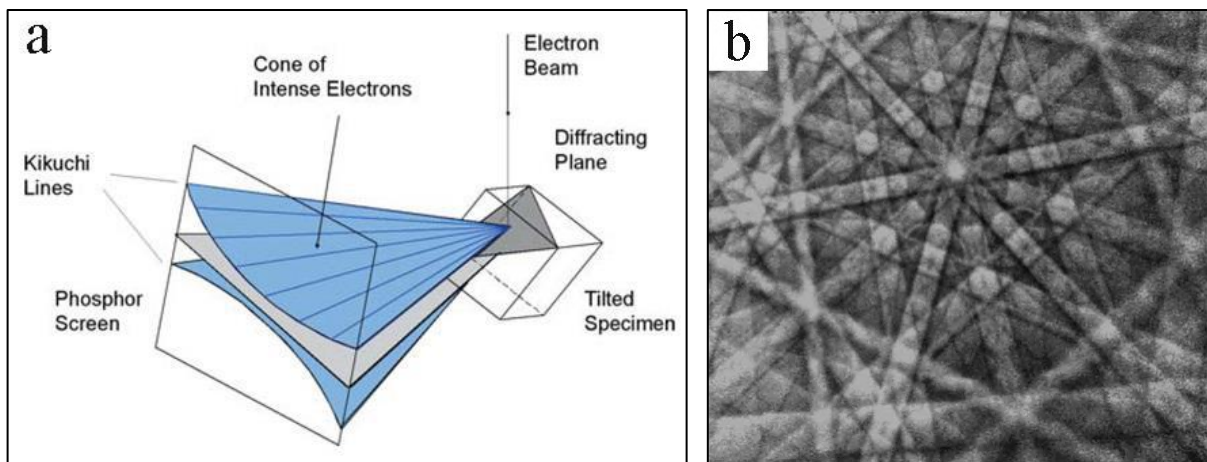


Fig. 2.5 (a) Origin of Kikuchi Band (b) A Kikuchi pattern from Cadmium at a measured point (Schwartz *et al.*, 2010).

With different acceleration voltages, probe currents and materials, a state-of-art EBSD instrument can reach a spatial resolution of 0.02 μm (*Schwartz et al.*, 2010) and an angular resolution of 0.1° (*Zaefferer*, 2011). The EBSD measurements of in this work were carried out using a SEM (JEOL JSM-6400 field emission SEM, Department of Earth- and Environmental Sciences, University of Munich) equipped with a Nordlys EBSD detector. Under the acceleration voltage of 20 kV, the samples were indexed and mapped using AZtecHKL software for different scanning step sizes. The EBSD data were analysed with CHANNEL5 software at the electron microscopy unit (BEEM) of Hamburg University of Technology, Hamburg Harburg.

2.4 Laser Raman spectroscopy

Raman spectroscopy is a non-destructive spectroscopic method to study the frequency ranges associated with molecular vibrations and rotations. The name is after the scientist Raman who first observed this type of light scattering experimentally (*Raman and Krishnan, 1928*). It is often used for characterizations of phases and structural phase transitions.

Basic theory of Raman spectroscopy

Light or electromagnetic radiation is a transverse wave of energy propagating through time and space. It is composed of electric and magnetic field oscillating perpendicular to each other and to the propagation direction. Electromagnetic radiation can be characterized by its wavelength (λ), frequency (f) and energy (Q_e), and can be regarded as packets or quanta of energy. A single quantum of the light energy is called photon, which can be characterized by its frequency (f) and photon energy (E), the relationship between the frequency and photon energy is:

$$E = hf \quad (2.2)$$

where h is Planck's constant (*Halliday et al., 2013*).

Crystals are solid material whose compositions (atoms, molecules, or ions) have long-range spatial periodicity. The atoms in crystals occurs in a periodic arrangement and are bound with each other by different forces. The lattice is however not a static structure. Atoms are thermally activated and moving around their lattice sites showing different vibrations. In a primitive unit cell of the lattice, N atoms vibrate in 3 dimensions and have $3N$ degrees of freedom. The collective vibration of all atoms can be described by different normal modes. The quanta of these normal modes are called phonons, which can be characterized by their frequency (f) and phonon energy (E). In one primitive unit cell, there are three acoustic phonons. The rest, $3N-3$ phonons are optical phonons, of which the adjacent atoms are vibrating out of phase (*Patterson and Bailey, 2007*).

When a beam of light interacts with crystals, the photons of the electromagnetic radiation may be absorbed, scattered, or may not interact with crystals and pass through it. The electric field of the incident light will induce a dipole moment for the polarized molecules in crystals. The relationship between dipole moment μ and the electric field E is:

$$\mu = \alpha E \quad (2.3)$$

where α is the polarizability tensor (Colthup, 2012).

If the energy of an incident photon corresponds to virtual energy levels of optical phonons in crystals, phonons will be excited. In this process, the dipole moment of the molecule vibration will change and vibrational energy will be promoted to a higher state. This change of dipole moments caused by the interaction between photons and optical phonons can be applied in infrared spectroscopy.

A part of the incident photons may also be scattered. The scattered photons consist of three types: the elastically scattered one is called Rayleigh scattering, which is strong and has the same energy as the incident light; the second one, which is inelastically scattered by acoustic phonons, called Brillouin scattering; the third is inelastically scattered by optical phonons. The last scattering is weak and the energy of scattered photons has been changed and it is called Raman scattering. Raman scattering consists of two types: when the energy of scattered photons is lower than the incident photon, it is called Stokes Raman scattering; when the energy of scattered photons is higher than the incident energy, it is called anti-Stokes Raman scattering (Lewis and Edwards, 2001; Smith and Dent, 2013). Fig. 2.7 shows a schematic illustration of the infrared absorption, Raman and Rayleigh scattering. In the process of Raman scattering, the polarizability or the electron cloud may change and determines if phonons are Raman active or not.

The vibrational modes of a crystal are specific to the crystal's chemical composition, structure and symmetry. If a monochromatic radiation with a single frequency (e.g. laser) is used as a light source and the scattered light is collected by a detector, the frequency shift between scattered and incident light caused by the crystal's vibrational modes can be analysed to reveal the internal structure of the crystal.

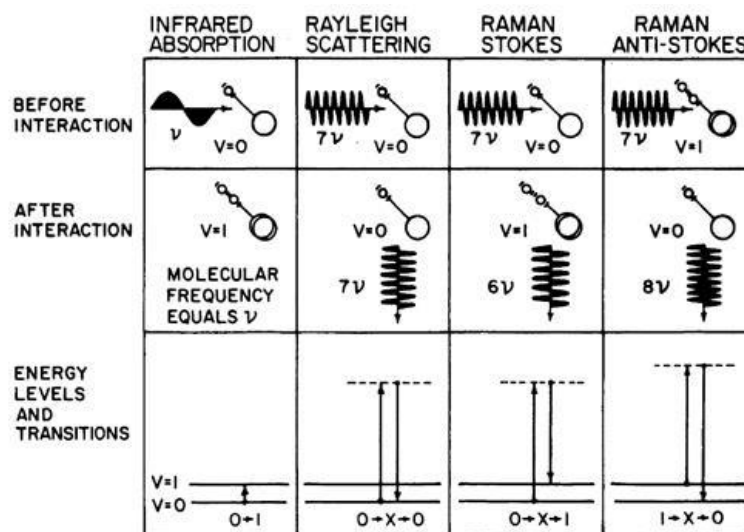


Fig. 2.7 Schematic illustration of infrared absorption and different scatterings (Colthup, 2012). $v=0$ and $v=1$ represent different vibrational energy levels of a molecule. $v=0$ is the ground state, $v=1$ is the first excited energy state and the dashed lines are virtual energy states.

One application of Raman spectroscopy is using polarized Raman spectroscopy, which allows analysing the crystal orientation. A parallel or perpendicular configuration is defined when the polarization of incident light is parallel or perpendicular to the polarization of scattered light, respectively. Due to the different symmetries of Raman modes, the appearance of certain Raman modes may vary under different configurations. The ratio between the intensities of two configurations is called depolarization ratio (Colthup, 2012):

$$\rho = \frac{I^{\perp}}{I^{\parallel}} \quad (2.4)$$

When the propagation direction of incident and scattered light and their polarization directions are well defined in the experiment, the depolarization ratio is due to the symmetry of the Raman modes and the orientation of the crystal.

For a given crystal, the relative intensity of a Raman spectrum caused by different Raman modes can be determined. The determination of the Raman spectrum of aragonite is given in Chapter 3.3.

Experimental setup

A HORIBA Scientific's T64000 triple-grating Raman spectrometer at the Mineralogy-Petrology Institute of Universität Hamburg was used to collect Raman spectra. An Ar^+ laser

with wavelength of 514.5 nm and adjusted power output of 600 mW was used as light source. An Olympus BX41 microscope was applied for microscopic measurements. The laser spot was focused on the sample surface with a diameter of ca. 2 μm . Raman spectra ranging from 15-1210 cm^{-1} were collected with a resolution of 2 cm^{-1} . The data were analysed with OriginPro software.

Mappings under both, parallel and perpendicular polarization configurations were performed both on the polished nacreous and prismatic layers of *Anodonta cygnea*. The mapped areas are 25 $\mu\text{m} \times 40 \mu\text{m}$ and 50 $\mu\text{m} \times 20 \mu\text{m}$ in nacreous and prismatic layers, respectively. The step length of mapping is about 1 μm .

To resolve the angular variation of the *a*- and *b*-axis in the nacreous layer, a series of Raman measurements were carried out using a single-crystal aragonite reference on (001). In order to have a series of depolarization ratios using different angles of polarization directions, the aragonite crystal was rotated around the *c*-axis in step of 5° for the measurements under both, parallel and perpendicular polarization configurations. The depolarization ratios of selected Raman modes were then calculated.

In the experiments with aragonite and shells, Raman spectra were collected in backscattering geometry. Two coordinate systems were used (see Fig. 2.8), one associated with the laboratory space-fixed coordinates (O, X, Y, Z) (black colour) and the other is given by the sample (o, x, y, z) (red colour).

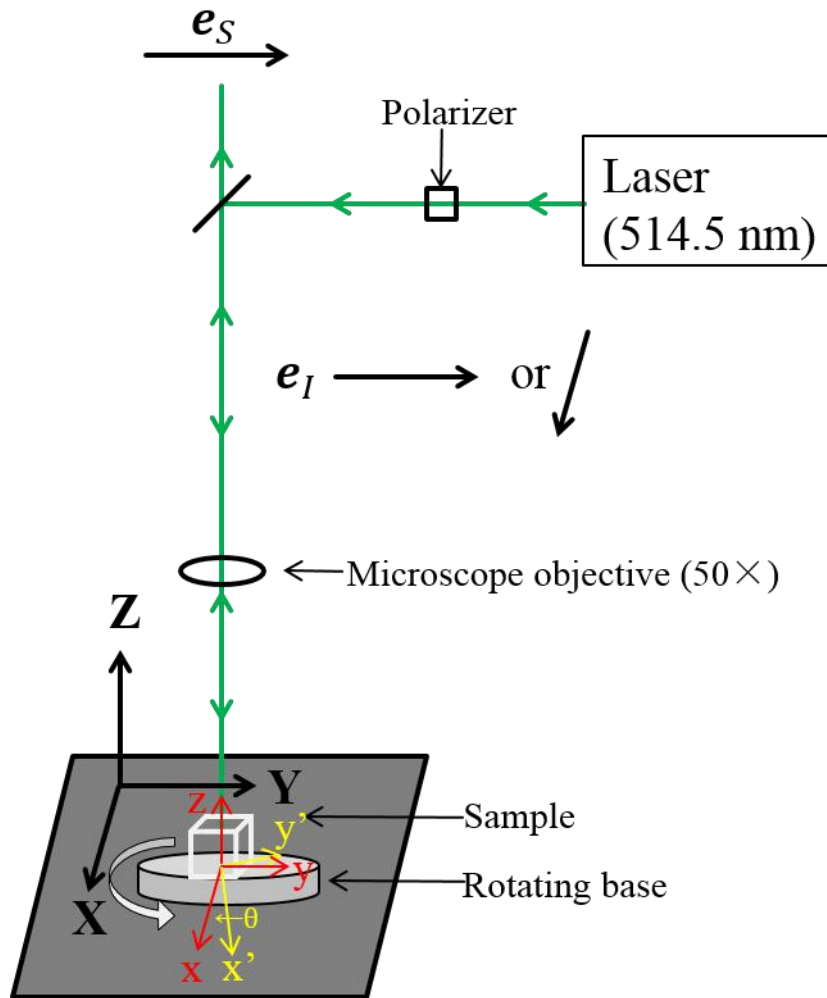


Fig. 2.8 Schematic illustration of the experimental configuration. There are two coordinate systems, one associated with the laboratory space-fixed coordinates (O, X, Y, Z) (black colour) and the other is determined by the sample (o, x, y, z) (red colour). Sample is stepwise rotated by the angle θ around the z-axis to (o, x', y', z').

In order to indicate the orientation of the crystal with respect to the polarization of the laser, Porto's notation was adopted. It consists of four letters: A(BC)D, A is the direction of the propagation of the incident light k_i , which is defined in the experiment as \bar{Z} ; B is the direction of the polarization of the incident light e_i , which can be changed to crossed polarization X or parallel polarization Y using a λ half-wave plate; C is the polarization of the scattered light e_s , which is parallel to Y in the instrument; D is the direction of the propagation of the scattered light k_s , which is along Z. In conclusion, there are two principle geometries denoted as $\bar{Z}(YY)Z$ and $\bar{Z}(XY)Z$, respectively.

2.5 Electron microprobe

Electron microprobe analysis (EMPA) is a technique to determine the chemical composition of solid materials on the micrometre length scale.

Similar to SEM and EBSD, EMPA uses a beam of primary electrons to bombard the sample as has been shown in Fig. 2.4. The primary electrons interact with atomic nuclei in crystals and may be scattered inelastically. An inner electron of the element (except for several low atomic number ones) in a crystal gained energy from the primary electron and is excited to a higher energy state, leaving a vacancy in the electron shell. The vacancy is not stable and must be filled by an electron from a higher energy state. During this process, the transition of the electron from higher energy state to the vacancy will emit X-rays characteristic to the atomic number of the element. Thus, the X-rays can be measured by detectors and used to determine the elements.

A CAMECA SX100 electron microprobe analyser was applied at the Mineralogy and Petrology Institute of Universität Hamburg. The electron microprobe measurements were done at the same areas of the samples as the EBSD measurements. Six elements, Mg, S, Ca, Mn, Sr, Ba, were determined qualitatively by mappings and quantitatively by profile analyses. All measurements were taken under an acceleration voltage of 15 kV and a probe current of 20 nA.

3 Results

3.1 Morphology of samples

Under the optical and the SEM microscope it is seen that the inorganic parts of the three shells can be divided into two layers with distinguishable structures. The one at the outside of the shell, which is covered by periostracum layer and composed of prisms or columns, is called prismatic layer. The other one, which is at the inner side and composed of nacre lamellae, is called nacreous layer. The two layers in three species share some similarities but still have relevant differences. Morphological studies are therefore focused on each of the two layers and the transition area where they change from one to another.

3.1.1 *Pinctada fucata*

Fig. 3.1 shows the inner surface of *Pinctada fucata* shells. Two areas with different morphological features are shown in Fig. 3.1a. One area is composed of small tablets and is called nacreous layer (N in Fig. 3.1a). The other one is composed of larger polygonal prisms, it is called prismatic layer (P in Fig. 3.1a).

The surface of the nacreous layer shows a terraced pattern (see Fig. 3.1b). Each step of the terrace is composed of a layer of compact nacre tablets. An overview using smaller magnification of the terraced surface from another sample of *Pinctada fucata* is shown in Appendix Ia. The diameter of the nacre tablets in each nacre lamella is about 2-5 μm .

The prisms in the prismatic layer range from 15-50 μm in diameter and have a flat surface (Fig. 3.1c). The top of the prisms near the interfacial zone are covered with a layer of organic substance, the coverage by organic material declines as the distance between prisms and interfacial zone increases.

Fig. 3.2 shows a cross section of the shell of *Pinctada fucata*. From the fractured surface, one can observe that the nacreous layer is constructed by compact parallel lamellae. The thickness of each lamella is about 0.5-0.7 μm . The prismatic layer is built up by packed prisms with their extended axes perpendicular to the surface of the shell. The thickness of the prismatic layer in *Pinctada fucata* is about 700-1000 μm . It can be seen that the prisms are composed by fine compacted particles (Fig. 3.2b) and the fractures of prisms appear to be flat and they are perpendicular oriented to the long axis of the prisms (see red dashed areas in Fig. 3.2a).

3.1 Morphology of samples

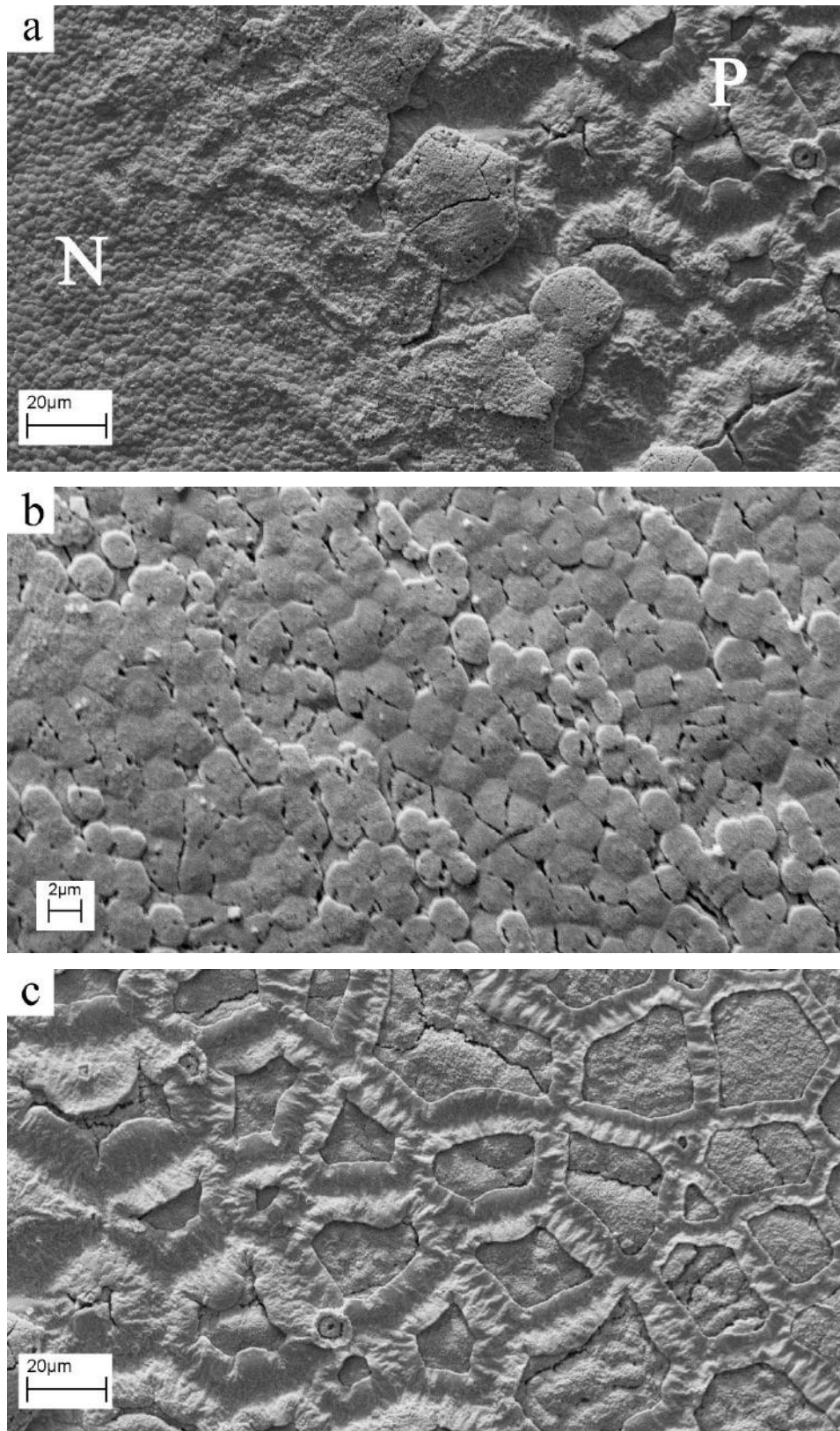


Fig. 3.1 SEM images of a lateral section from *Pinctada fucata* shell. (a) Overview at interfacial area in lateral section. N represents nacreous layer, P represents prismatic layer. (b) Nacreous layer with a terraced surface composed of nacre tablets. (c) Prisms with flat surface, partially covered by organic matter near the interfacial area.

3.1 Morphology of samples

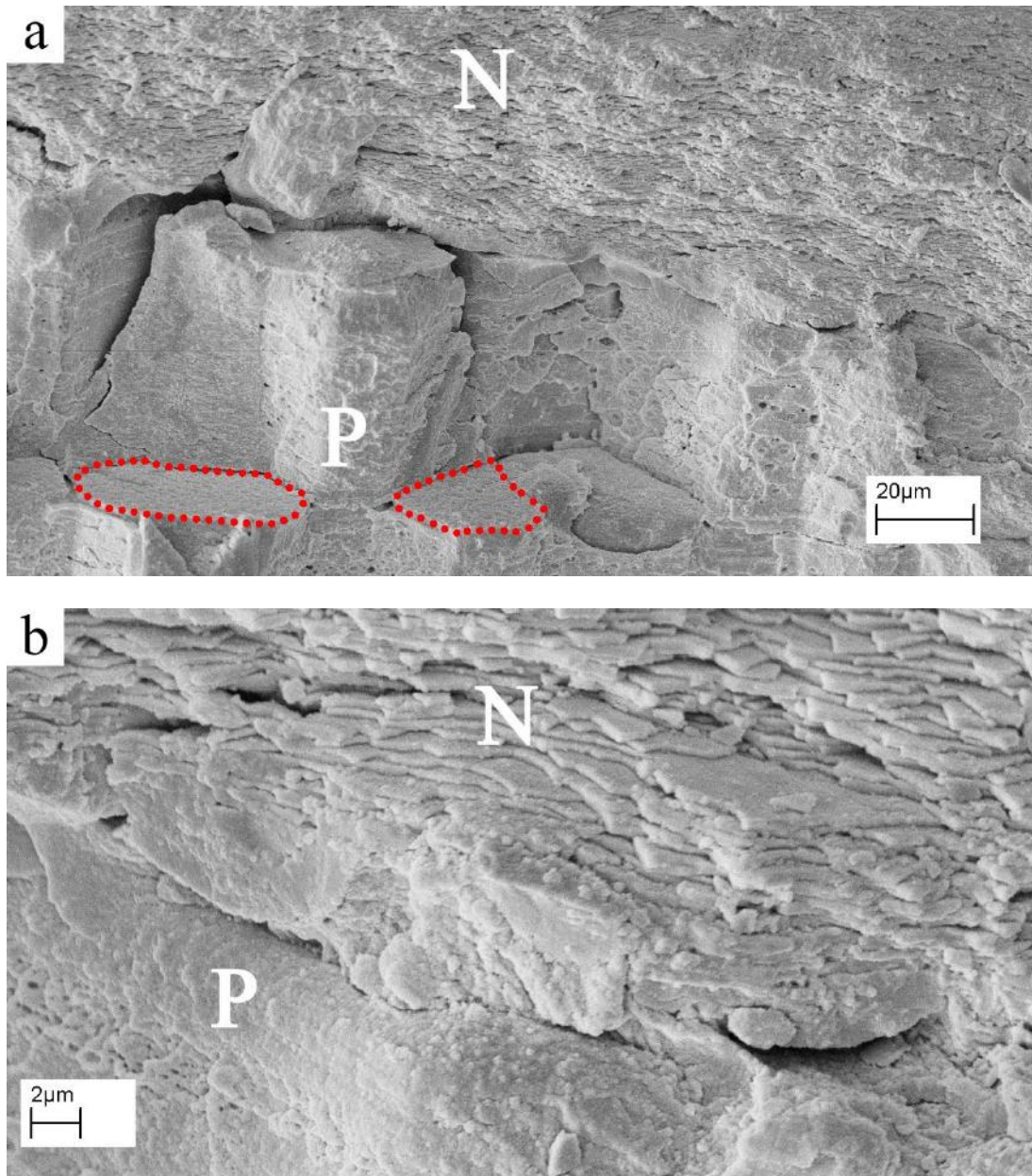


Fig. 3.2 SEM images of a cross section from *Pinctada fucata*. (a) Overview of the interfacial area between two layers. The prisms show flat fractures (see dashed red circles). (b) Details of the interfacial area showing the size of the nacre tables. The prism are composed of fine particles.

3.1.2 *Anodonta cygnea*

Fig. 3.3 shows the inner surface of the shells of *Anodonta cygnea*. Nacreous layer (N), prismatic layer (P) and the interfacial zone in between occurs clearly at the surface (Fig. 3.3a).

Unlike the nacreous layer of *Pinctada fucata* shell, *Anodonta cygnea* shows a rough surface without apparent terraced features (see Fig. 3.3b). The hexagonal nacre tablets are located separately upon the former tablets, instead of being attached at the edge of a lamella to form a terraced area. From the gaps between the tablets, one can see at least 3-4 unclosed nacre lamellae on the surface. Many of the nacre tablets possess a small concave centre (see example inside red circle in Fig. 3.3b). The diameter of the nacre tablets is about 2-5 μm . An overview of a larger surface from another sample of *Anodonta cygnea* is shown in Appendix I.b.

In the prismatic layer, prisms range from 5-30 μm in diameter and each prism has a convex surface (Fig. 3.3a). Similar to *Pinctada fucata*, the prismatic layer is composed of polygonal shaped prisms, but one major difference is that the prisms of *Anodonta cygnea* near the interfacial zone are not covered with organic layer and the nacre tablets appear directly on top of the prisms (Fig. 3.3c). Moreover, some of the prisms do not only have clear boundaries with their neighbouring prisms but also possess 'cleavages' within the prisms (see the black arrows in Fig. 3.3a and c).

Fig. 3.4 shows a cross section of the *Anodonta cygnea* shell. The thickness of each nacreous lamella in *Anodonta cygnea* is about 1.3-1.5 μm . The prismatic layer is also built up by packed prisms with their extended axes perpendicular to the nacre lamellae. However, the interface of the two layers forms about 20° to the nacre lamellae. Due to the convex nature of the prisms, there are empty spaces left between the nacreous and prismatic layer where the nacre tablets did not complete the filling (see red circles in 3.4a). The thickness of prismatic layers in *Anodonta cygnea* is about 50-100 μm . The prisms of *Anodonta cygnea* have ragged fractures and are composed of granules or spherulites with a size of about 1 μm (see Fig. 3.4b). Another important difference between shells of *Pinctada fucata* and *Anodonta cygnea* is that the particles at the top of *Anodonta cygnea* prisms form fibre-shaped crystallites (see area between dashed lines in Fig. 3.4a and red dashed area in Fig. 3.4b).

3.1 Morphology of samples

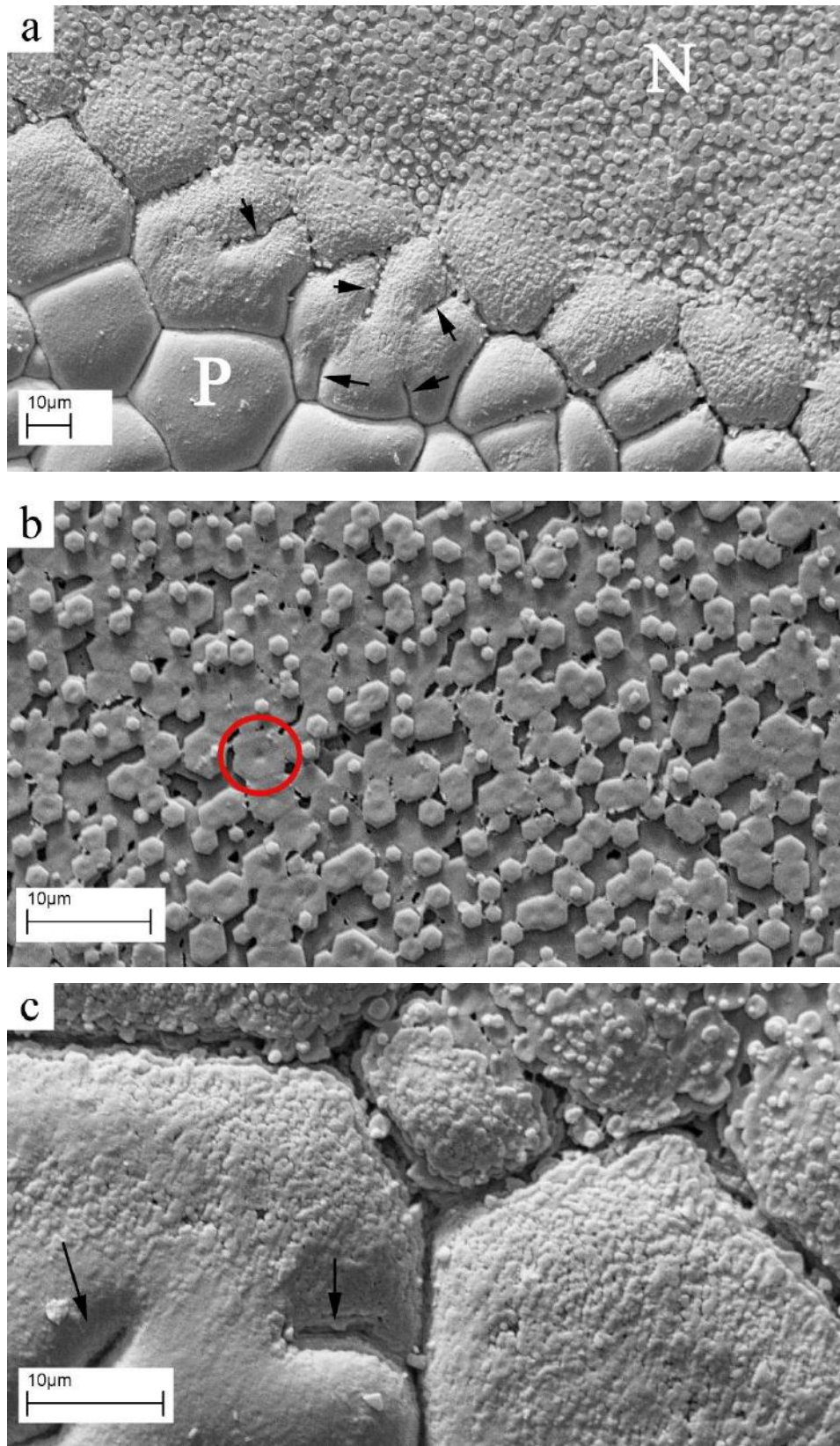


Fig. 3.3 SEM images of lateral sections of *Anodonta cygnea* shells. (a) Overview of the interfacial area between nacreous layer (N) and prismatic layer (P). Each prism has a convex shaped top. (b) The nacre tablets have regular hexagonal shape and no terraced morphology. The Red circle indicates the concave centre of a tablet. (c) Detail of the interfacial area show that nacre tablets grow directly on top of the prisms.

3.1 Morphology of samples

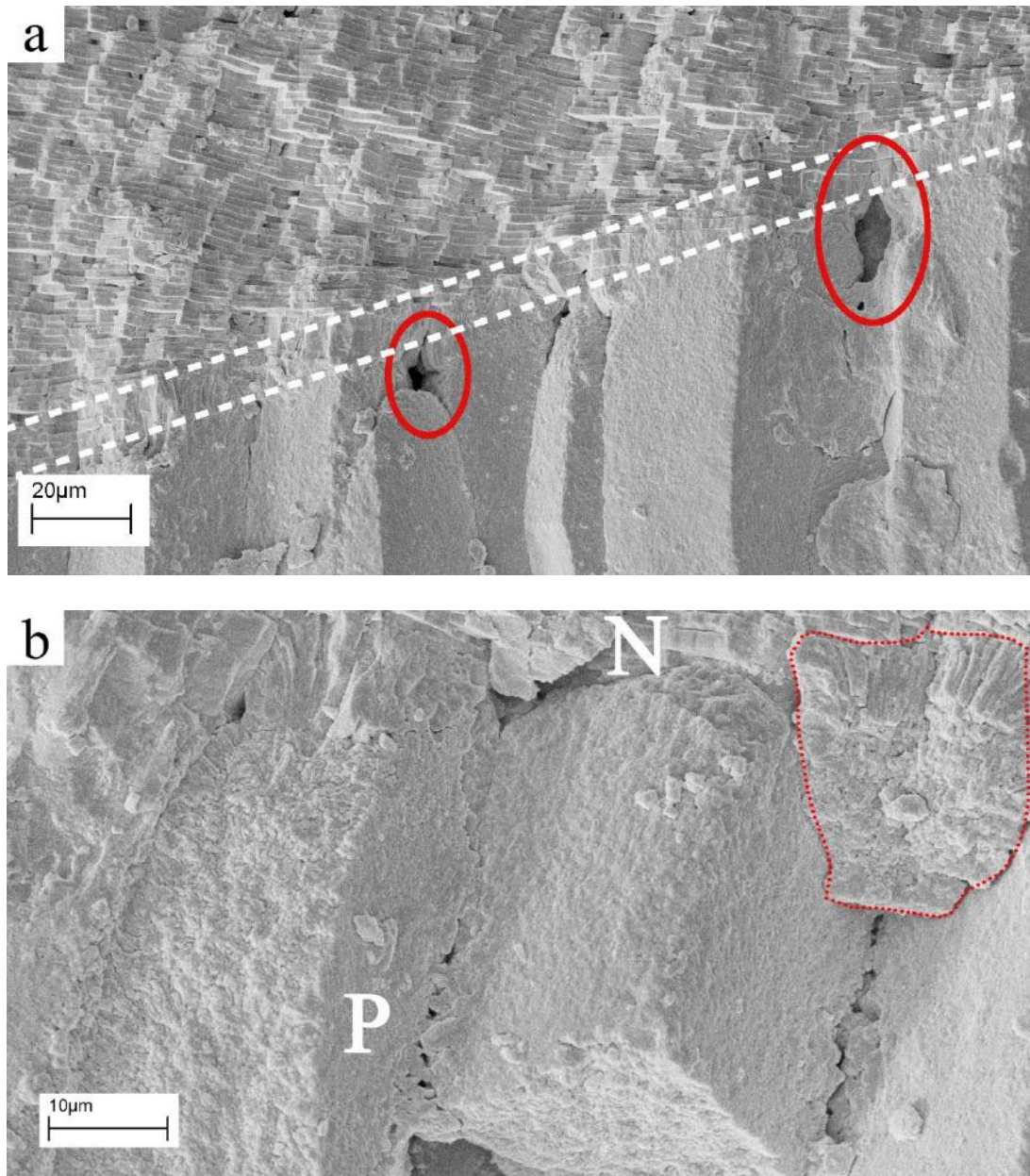


Fig. 3.4 SEM images of a cross section from the *Anodonta cygnea* shell. (a) Overview of the interfacial area between two layers. The crystallites have fibrous shape at the top of the prisms (between white dashed lines). There are empty spaces left between the two layers (red circles). (b) An enlarged area of the prisms showing that they are composed of spherulites compared to the ones seen in *Pinctada fucata*. Fibrous crystallites are also shown in the red dashed circle.

3.1.3 *Phorcus turbinatus*

Fig. 3.5 shows a lateral section of the *Phorcus turbinatus* shell. Similar to the other two species, the inner surface can be divided into two parts with different features: nacreous layer (N) and prismatic layer (P) (Fig. 3.5a).

Different from nacreous layers in *Pinctada fucata* and *Anodonta cygnea*, the surface of the nacreous layer is covered with nacre columns (see right part in Fig. 3.5a, and Fig. 3.5b). From Fig. 3.5b, it is seen that each column is a stack of nacre tablets with a clear hexagonal shape. The size of the tablets shrinks from the bottom to the top of the columns. Some columns are isolated, some of them are aligning together and the tablets are intersecting with each other (red circles in Fig. 3.5b). In the centre of the tablets on the top, one can also find holes or concavities similar to the shell of *Anodonta cygnea*. The diameter of the nacre tablets is about 2-10 μm . An overview of the surface from another sample can be seen in Appendix Ic.

Different from the prismatic layers in *Pinctada fucata* and *Anodonta cygnea*, the inner surface of the prismatic layer of *Phorcus turbinatus* is not smooth like in the other two species but rather coarse. The prisms range from 20-80 μm in diameter and each prism has a convex-like shape (left part in Fig. 3.5a). From the detailed image of the interfacial area between the two layers, one can see that the columns of nacre tablets grow directly on the uneven surface of the prisms (Fig. 3.5c).

Fig. 3.6 shows a cross section of the *Phorcus turbinatus* shell. The nacreous layer is similar to the other two species. It is composed of nacre lamellae and the thickness of each lamella is about 1-1.6 μm . The nacre lamellae form an angle of about 20° to the boundary of prismatic and nacreous layer. There is no significant transition area between nacreous and prismatic layers. Besides, there are also no distinctive boundaries between the prisms. Different from bivalves, the prismatic layer gets thicker and thicker in gastropod as the animal grows. In the shown sample, the thickness of the prismatic layer ranges from 300-1000 μm . In the enlarged image of the prisms (Fig. 3.6b), we can see that each prism is composed of fibrous crystallites. The same result has been shown using a polarized light microscope in Appendix VI.

3.1 Morphology of samples

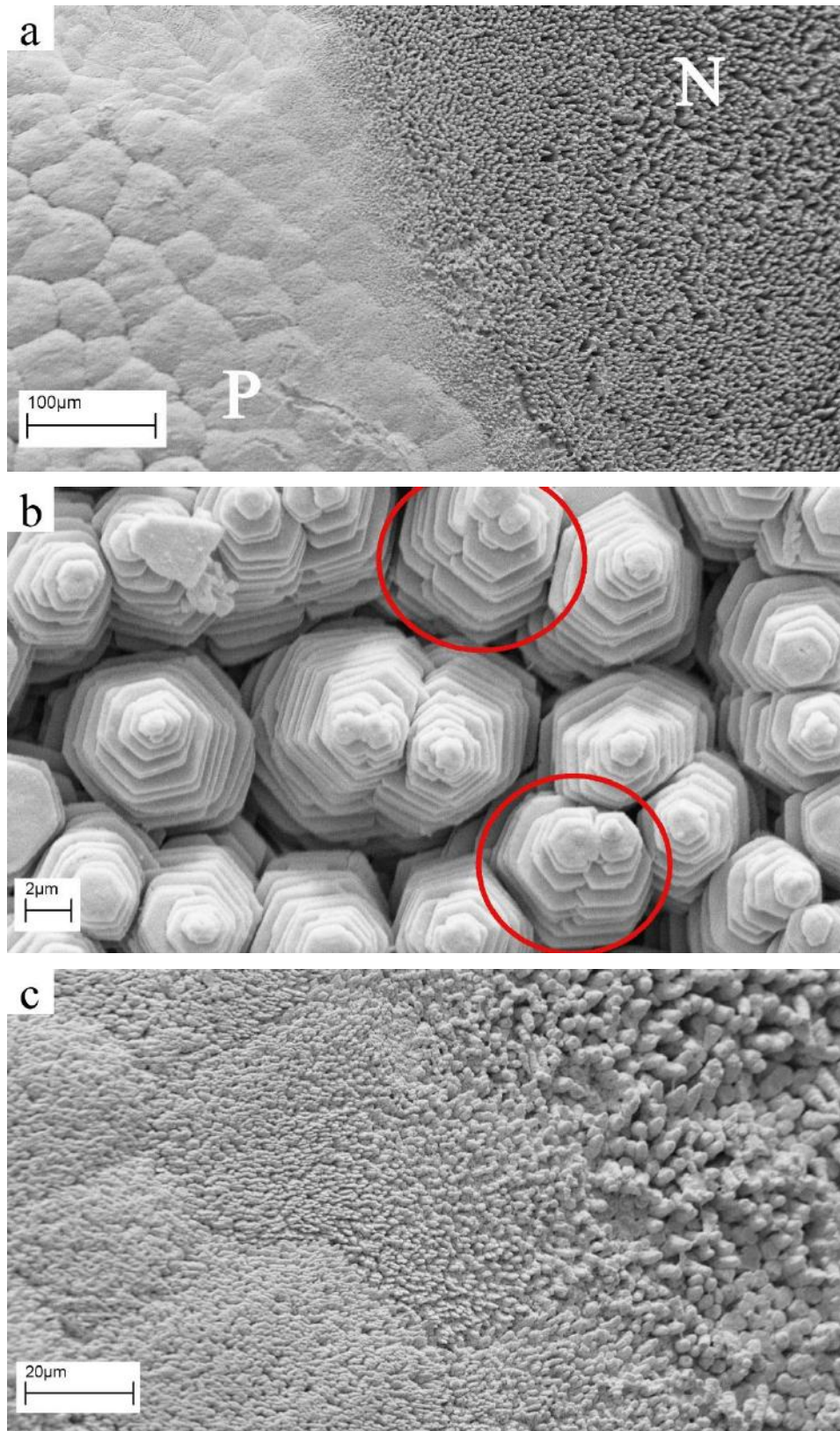


Fig. 3.5 SEM images of the inner surface from *Phorcus turbinatus*. (a) Overview of interfacial area between nacreous layer (N) and prismatic layer (P). (b) Enlarged area of nacreous layer. The nacreous layer forms a surface of tapering stacks, which are composed of hexagonal tablets. Red circles indicate columns which are aligning together. (c) Details of the interfacial area, where columns of nacre grow directly on the rough surface of prisms.

3.1 Morphology of samples

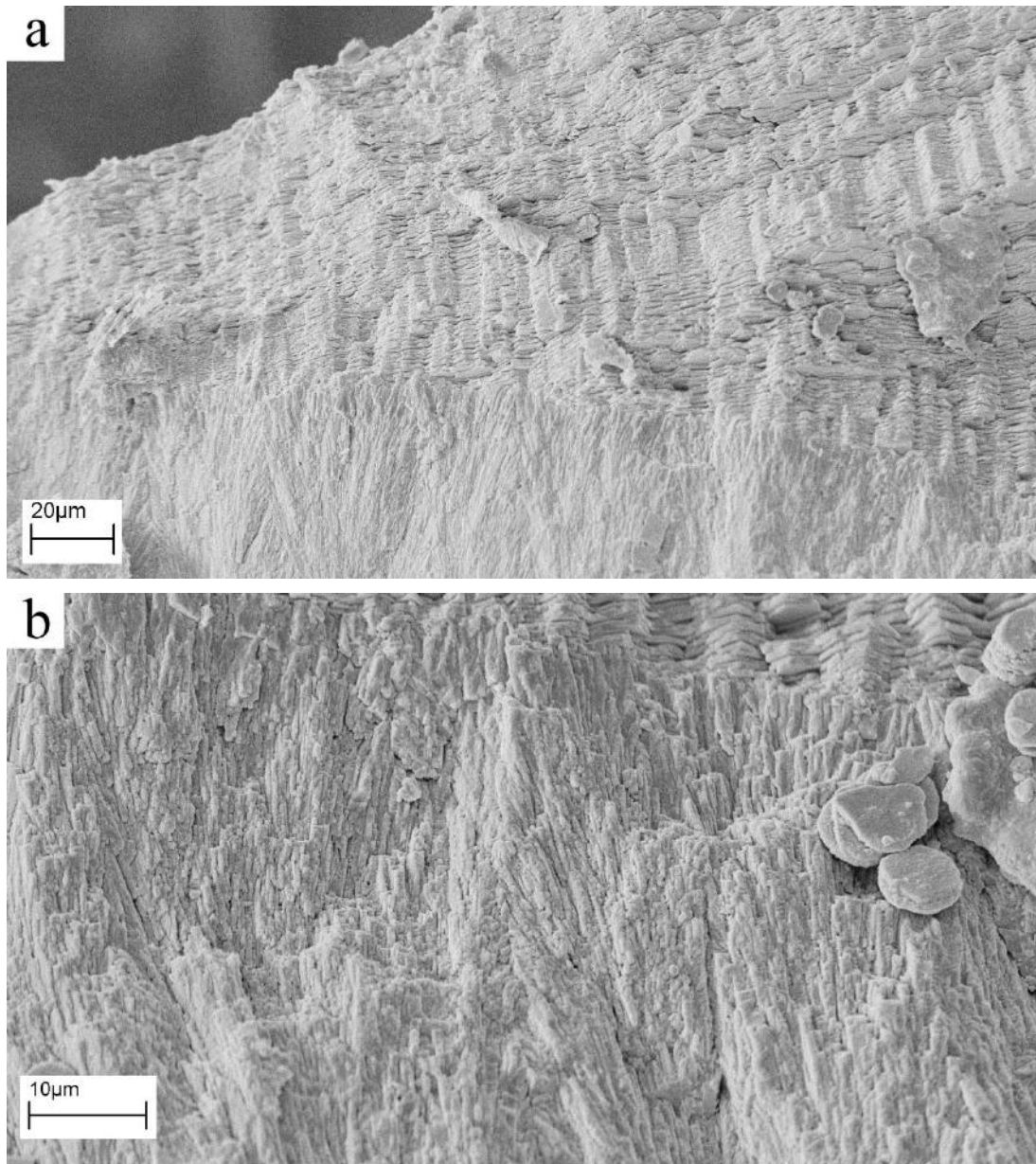


Fig. 3.6 SEM images of cross sections of the shell of *Phorcus turbinatus*. (a) Overview of the interfacial area between the two layers. (b) Fibrous feature of the prisms without obvious boundaries between the prisms.

3.2 Crystallography orientation of samples

EBSD experiments were undertaken on both, lateral and cross sections. Results are presented as band contrast maps, orientation information maps, pole figures and misorientation angle distributions.

3.2.1 *Pinctada fucata*

Lateral section

The EBSD measurements on lateral sections have been done in the nacreous layer and prismatic layer separately.

Fig. 3.7 shows the EBSD results from the lateral section of the nacreous layer of *Pinctada fucata* with relevant topological information. Since the sample was placed in the sample chamber with a tilt angle of 70° against the electron beam, the images are compressed in the vertical direction of the surface. Fig. 3.7a is the band contrast (BC) image of one mapped area which is almost parallel to the nacre lamellae, it was indexed using the lattice parameters of aragonite. The band contrast map describes the intensity of the Kikuchi diffraction of each indexed point on the map. Intensities are scaled from 0 to 255 and the BC map is plotted using a grayscale from black to white (Zhou and Wang, 2007). Deformation on the surface and organic matter in the shells do not lead to diffraction and hence, those areas remain dark. Because the cut is not exactly parallel to the nacre lamellae, which is unlikely to achieve under the preparation conditions since each lamella in Fig. 3.2b is less than $1\ \mu\text{m}$ thick, so we can observe dark parallel lines on the surface. Each dark line corresponds to a nacre lamella. Each lamella is built of small tablets, which corresponds to the SEM results in Fig. 3.1b. The upper half of the BC map (Fig. 3.7a) is superimposed by grain boundaries with angles of $63.8^\circ \pm 2^\circ$ (red), $52.4^\circ \pm 2^\circ$ (green) and $> 2^\circ$ (yellow) between them. The red and green boundaries represent the misorientation angles between different aragonite twins. The yellow boundaries represent misorientation angles of low-angle grain boundaries (LAGBs) (He *et al.*, 2016). For two given orientations of two crystallites, one can superimpose one crystallite onto the other by rotating around the common axis of the two crystallites. Misorientation angle is defined as the smallest rotation angle among equivalent rotations. From the insets in Fig. 3.7a, it can be seen that the grain boundaries occur between the tablets.

Fig. 3.7b indicates the EBSD crystallographic orientation map using the IPF colouring code, corresponding to Fig. 3.7a. The inset in the map shows the colour key, where the numbers at the corners represent principle crystal axes of aragonite. The X, Y or Z coordinate in colour keys indicates the horizontal, vertical or normal direction of the measured surface. The IPF map displays the crystallographic orientation of each indexed crystallite with respect to the X, Y or Z direction of the measured surface. Same or similar colours indicates same or similar crystal orientations. Fig. 3.7b shows mostly red, yellow and green colours which means, that no *c*-axis (blue colour) is oriented toward the vertical view direction. Moreover, the distribution of the colours shows 'lizard skin' pattern, which means the *a*- or *b*-axis of aragonite crystallites are arranged in clusters or more exactly, in domains.

If one plots the orientation information of every indexed point from Fig. 3.7b on the same pole figures, there are collective pole figures of {001} and {100} which are shown in Fig. 3.7c. The *c*-axis is well co-oriented and points perpendicular to the measured surface. The *a*-axis is however arranged in six directions with a certain dispersion on the primitive circle. The MUD (multiples of uniform density) values at the pole figures are derived from the contouring of pole figures. A higher value of MUD stands for a higher crystal co-orientation. Fig. 3.7d shows the statistical distribution of misorientation angles between neighbouring crystallites. Except for the LAGBs below 15°, angles around 63.8° describe the most dominant group of misorientation angles.

Fig. 3.8 displays a lateral section of prismatic layers from *Pinctada fucata*. EBSD results show that the prismatic layer is composed of calcite. Prims can be easily distinguished from each other by dark boundaries between them.

Fig. 3.8b is the corresponding orientation information map of Fig. 3.8a. The colour key shows the normal direction of the measured surface. One can observe that either the *c*-axis (red colour) or *a*-axis (blue and green colours) is mostly perpendicular to the measured surface. Within each prism, the distribution of colours is either homogeneous or has a gradient. Three profiles have been selected in two prisms of *Pinctada fucata* (see the black arrows in Fig. 3.8b).

The collective pole figures from Fig. 3.8c correspond to the orientation maps. The *c*-axis of calcite crystallites is either perpendicular or parallel to the measured surface.

3.2 Crystallography orientation of samples

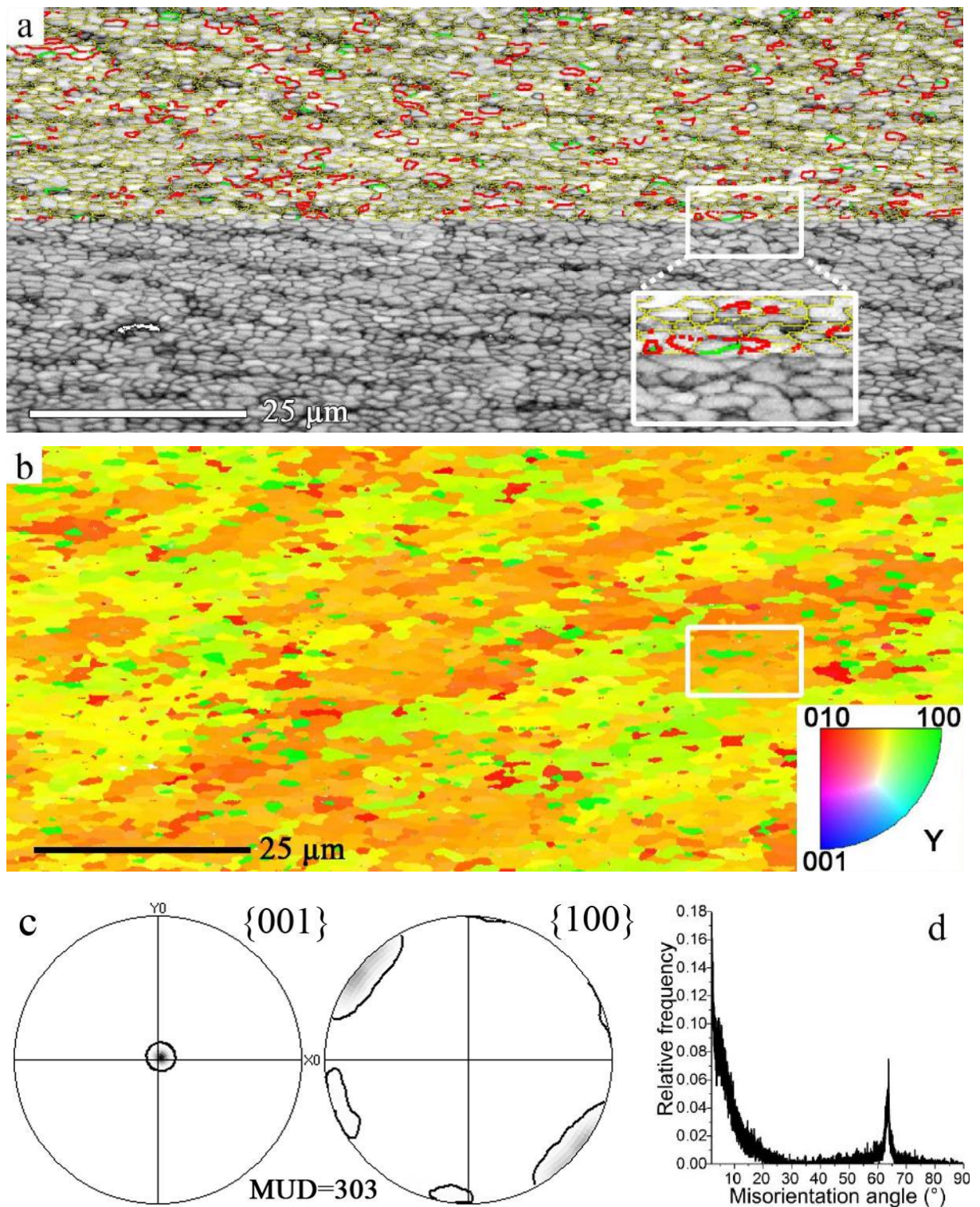


Fig. 3.7 EBSD measurement of the lateral section of nacreous layer of *Pinctada fucata*. (a) Band contrast (BC) map. In the upper half of the BC map, grain boundaries of $63.8^{\circ} \pm 2^{\circ}$ (red), $52.4^{\circ} \pm 2^{\circ}$ (green) and $> 2^{\circ}$ (yellow) are marked. The inset shows an enlarged area. (b) Crystal orientation information map of (a). The orientation colour key of aragonite is shown in the lower right corner. (c) Pole figures of $\{001\}$ and $\{100\}$ corresponding to (b), the MUD (multiples of uniform density) value is shown under the pole figures. (d) Misorientation angle distribution of (b).

3.2 Crystallography orientation of samples

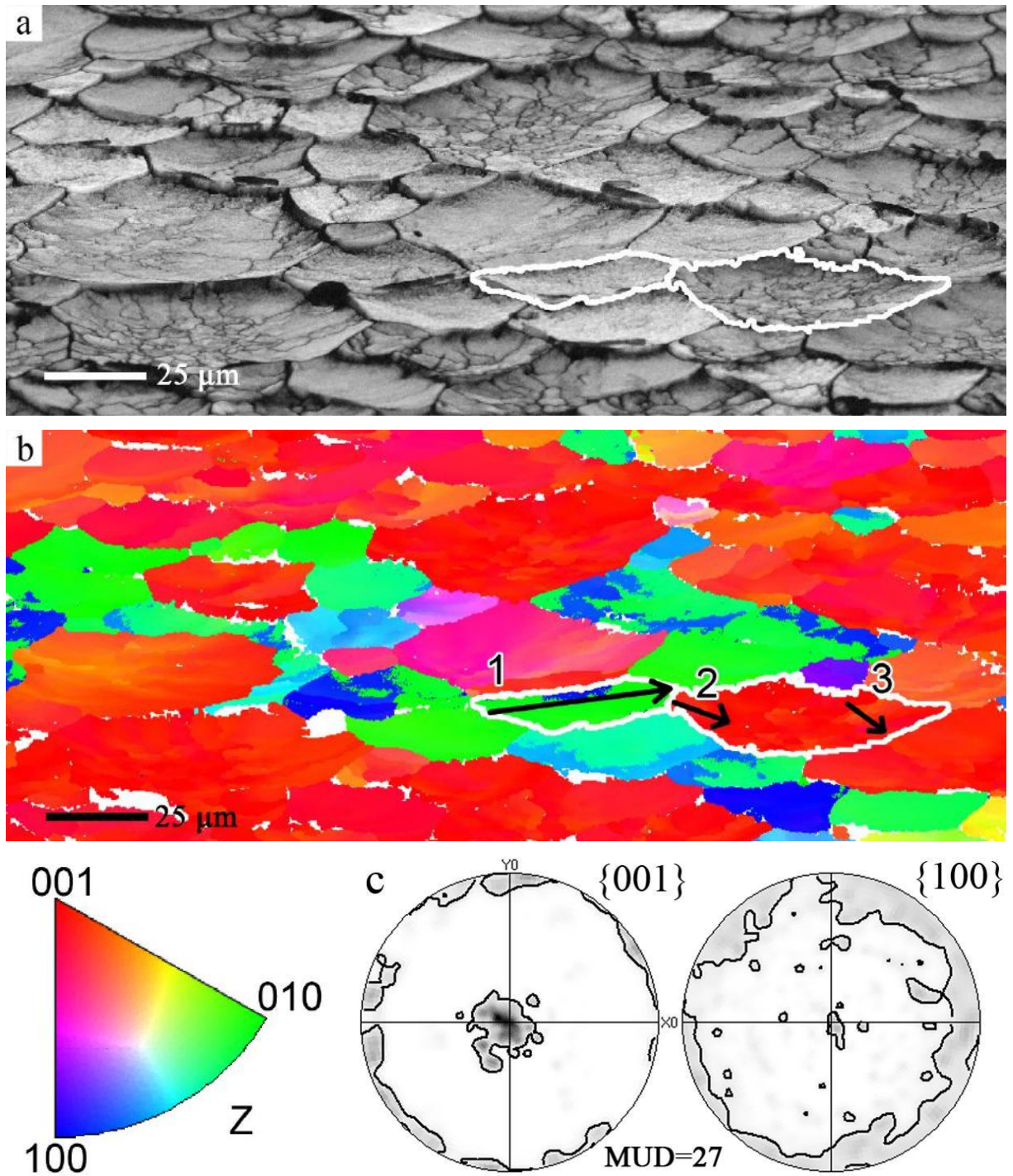


Fig. 3.8 EBSD measurement of the lateral section of the prismatic layer of *Pinctada fucata*. (a) Band contrast map. (b) Crystal orientation information map corresponding to (a). In *Pinctada fucata*, three line profiles labelled as 1-3 are shown in two white framed prisms. The arrows indicate the direction of profiles. The Z index at the corner of the colour key indicates the normal direction of the measured surface of Fig. 3.8b. (c) Pole figures of {001} and {100} correspond to Fig. 3.8b.

Cross section

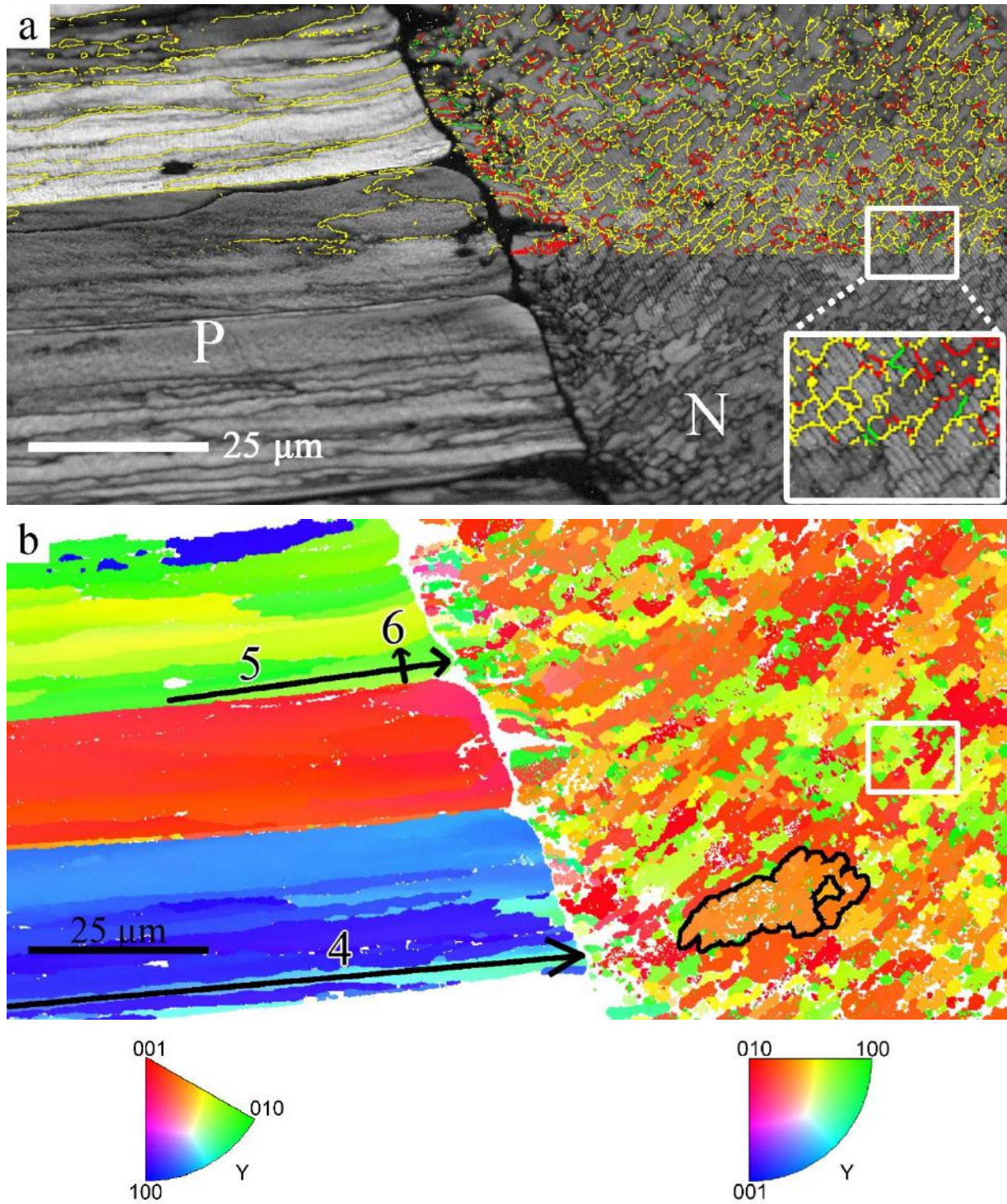
Fig. 3.9 shows the EBSD measurement of a cross section of an area containing both nacreous (right) and prismatic (left) layers in *Pinctada fucata*. Fig. 3.9a shows the band contrast map. The BC maps do not represent the true morphology of the surface but reflect the inner structure to some extent. Within the prisms, dark lines perpendicular to the boundary of the two layers can be observed. Within the nacreous layer, nacre lamellae parallel to the boundary of the layers can also be observed (see inset in Fig. 3.9a). Besides, a dark boundary between the prismatic and nacreous layer also exists. The upper half of the BC map is superimposed by grain boundaries with misorientation angles of $63.8^\circ \pm 2^\circ$ (red), $52.4^\circ \pm 2^\circ$ (green) and $> 2^\circ$ (yellow), only LAGBs are acquired in the prisms, but the twin boundaries are widely distributed both across and between the nacre lamellae (green and red colour in inset of Fig. 3.9a).

Fig. 3.9b is the matching orientation information map of Fig. 3.9a. The colour key for both layers is shown under the map. The prismatic layer is indexed using the lattice parameters of calcite and the nacreous layer is indexed using the aragonite lattice parameters. Both nacreous and prismatic layers have a high indexing rate. There occurs a gap between the calcitic prisms and aragonitic nacre, and there are no evident crystallographic relations between the two layers. In the prismatic layer, the three prisms show mainly three relatively homogeneous colours, green, red and blue. Other three profiles have been chosen in two prisms (see the black arrows), each of the profiles runs along an area separated by dark lines in the prisms. In the nacreous layer, the colours show a patchy pattern corresponding to the pattern in the lateral section. One colour (orientation) cluster has been selected by the black frame.

Fig. 3.9c and 3.9d show collective pole figures and the misorientation angle distribution in the nacreous layer of *Pinctada fucata*, respectively. Fig. 3.9e and 3.9f are equivalent pole figures of the prismatic layer. In the nacreous layer, the crystallographic *c*-axis of aragonite crystallites is well co-oriented along one direction, which is almost perpendicular to the boundary between the prismatic and nacreous layer. The misorientation angles around 63.8° and 57.5° are the two most dominant groups. In the prismatic layer, the *c*-axis of the three prisms is almost perpendicular to each other. The *c*-axis of the green prism is perpendicular to the measured surface and the long axis of the prism. The *c*-axis of the red prism is parallel to the measured surface and perpendicular to the long axis of the prism. The *c*-axis of the blue prism is parallel to the measured surface and the long axis of the prism. Finally, there is no

3.2 Crystallography orientation of samples

dominant angle differences between the neighbouring calcite crystallites in the misorientation angle distribution.



3.2 Crystallography orientation of samples

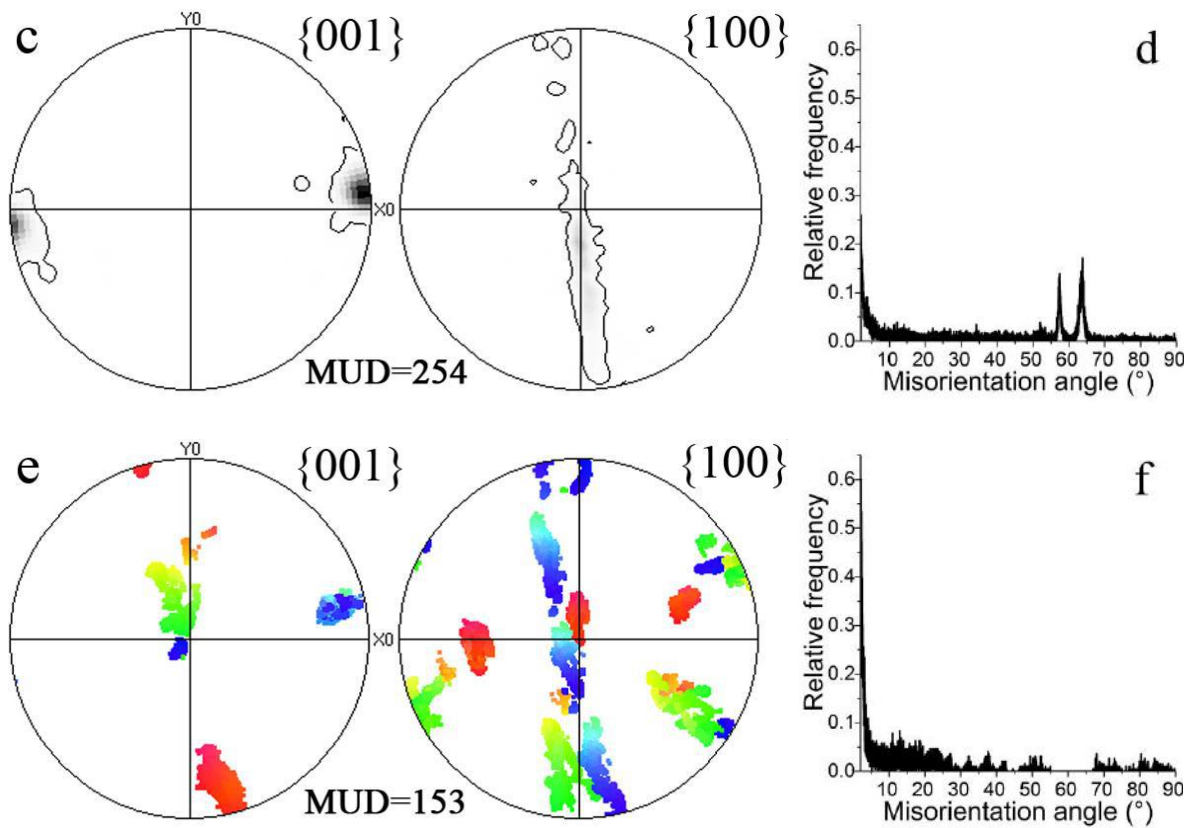


Fig. 3.9 EBSD measurement of the cross section of *Pinctada fucata*. (a) Band contrast map superimposed by grain boundaries with misorientation angles of $63.8^\circ \pm 2^\circ$ (red), $52.4^\circ \pm 2^\circ$ (green) and $> 2^\circ$ (yellow), inset shows an enlarged area of nacreous layer. (b) Orientation information map of (a). Three profiles labelled 4-6 and a colour cluster are selected from two prisms and nacreous layer, respectively. (c) Pole figures of {001} and {100} from the nacreous layer (right part) in (b). (d) Misorientation angle distribution of nacreous layer. (e) Pole figures of {001} and {100} from the prismatic layer (left part) in (b), colours in the pole figures correspond to colours in the prisms of (b). (f) Misorientation angle distribution of prismatic layer.

3.2.2 *Anodonta cygnea*

The shell of *Anodonta cygnea* was studied using both, EBSD and Raman measurements of different sections and layers.

EBSD measurements on lateral section

The measurements on lateral sections were carried out on the nacreous layer and prismatic layer separately.

Fig. 3.10 shows the lateral section of the nacreous layer from *Anodonta cygnea*. Fig. 3.10a is the band contrast map almost parallel to the nacre lamellae, it was indexed using structural data of aragonite. The upper half of the BC map is superimposed by grain boundaries with misorientation angles of $63.8^\circ \pm 2^\circ$ (red), $52.4^\circ \pm 2^\circ$ (green) and $> 2^\circ$ (yellow), it shows the twinning and the low-angle grain boundaries. Similar to *Pinctada fucata*, there occur parallel dark lines which indicate nacre lamellae. Each lamella is composed of nacre tablets corresponding to the SEM image shown in Fig. 3.3b. The inset in Fig. 3.10a shows that the grain boundaries are distributed around the nacre tablets indicating that the angle difference between the crystallites within one tablet is smaller than 2° .

Fig. 3.10b is the orientation information map. The index Y at the corner of the inset tells that all colours are shown with respect to the vertical direction of the measured surface. Different from the 'lizard skin' pattern in *Pinctada fucata* shell seen in Fig. 3.7b, the colours in *Anodonta cygnea* are quite homogeneous (green), except for a few isolated tablets with different orientation (red).

Two collective pole figures of {001} and {100} are shown in Fig. 3.10c. The *c*-axis is well co-oriented almost perpendicular to the measured surface. The *a*-axis is also oriented mainly in one direction but with a large degree of dispersion.

Fig. 3.10d shows the distribution of misorientation angles between neighbouring crystallites. The angles around and 57.5° are the two most dominant groups, the angle 63.8° has however a smaller fraction than *Pinctada fucata*.

Fig. 3.11 displays the lateral section of the prismatic layer of *Anodonta cygnea*. Different from *Pinctada fucata*, EBSD results show that the prismatic layer of *Anodonta cygnea* is composed of aragonite crystallites. Fig. 3.11a shows the BC map. Prisms can clearly be distinguished from each other and also the dark boundaries between them. Each prism does not have a compact texture but is composed of granules, corresponding to the granules found in

SEM images. One prism has been selected and is shown in the white frame where two twinning boundaries with misorientation angles of 63.8° and 52.4° occur.

Fig. 3.11b is the corresponding orientation information map. The colour key indicates the crystal orientation of prisms with respect to the vertical direction of the measured surface. Unlike the homogeneous distribution in calcitic prisms of *Pinctada fucata*, each of the aragonitic prisms is not dominated by one colour but they are multi-coloured.

Fig. 3.11c shows pole figures of $\{001\}$ and $\{100\}$ indicating that the *c*-axis of aragonite crystallites is centred in the direction perpendicular to the measured surface with a large dispersion, the *a*-axis is randomly distributed at the primitive circle.

Fig. 3.11d shows the distribution of misorientation angles in *Anodonta cygnea*. It is seen that the angles around 63.8° display a large quantity of misorientation angles.

Another result on the prismatic layer of *Anodonta cygnea* is shown in Appendix III, the index rate is not sufficient for this type of analysis, but the BC map shows the basic granular texture of the prisms.

3.2 Crystallography orientation of samples

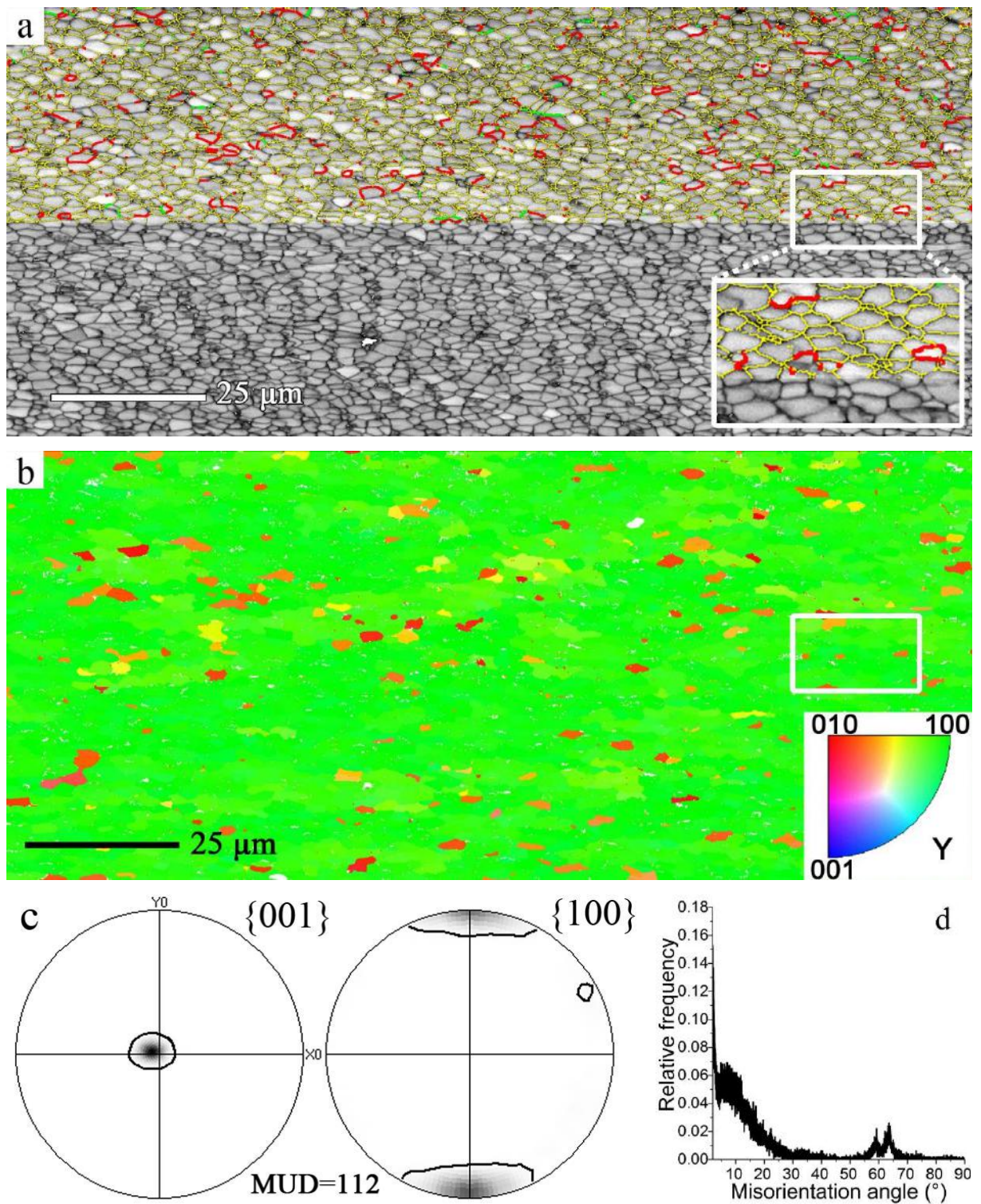


Fig. 3.10 EBSD measurement of the lateral section of nacreous layer of *Anodonta cygnea*. (a) Band contrast (BC) map. Upon the upper half of the BC map, grain boundaries of $63.8^\circ \pm 2^\circ$ (red), $52.4^\circ \pm 2^\circ$ (green) and $> 2^\circ$ (yellow) are superimposed. (b) Crystal orientation information map of (a). The orientation colour key is shown in the lower right corner. (c) Pole figures of $\{001\}$ and $\{100\}$ correspond to (b). (d) Misorientation angle distribution of (b).

3.2 Crystallography orientation of samples

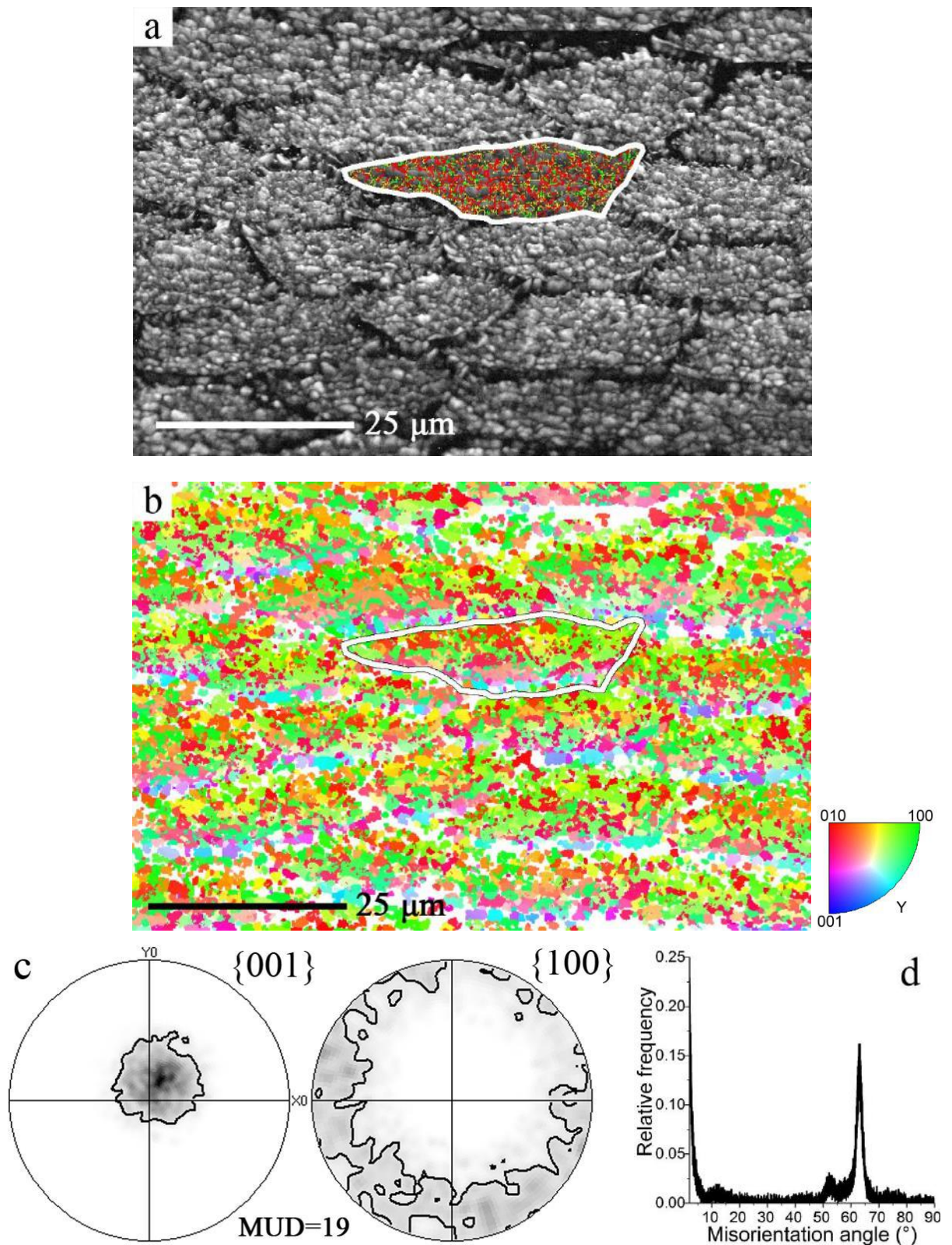


Fig. 3.11 EBSD measurement of the lateral section of the prismatic layer of *Anodonta cygnea*. (a) Band contrast map. A prism in the white frame is selected to show twinning boundaries. (b) Orientation information map corresponding to (a). The Y index at the corner of the colour key show the axis with respect to the vertical direction of the measured surface. (c) Pole figures of {001} and {100}. (d) Misorientation angle distribution of the aragonite crystallites.

EBSD measurement of cross section

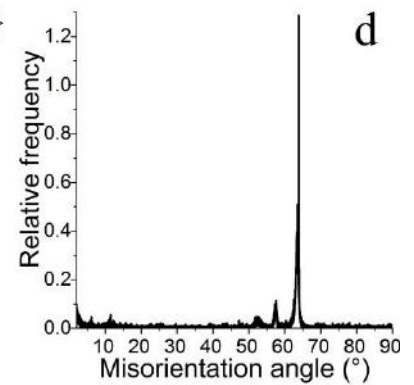
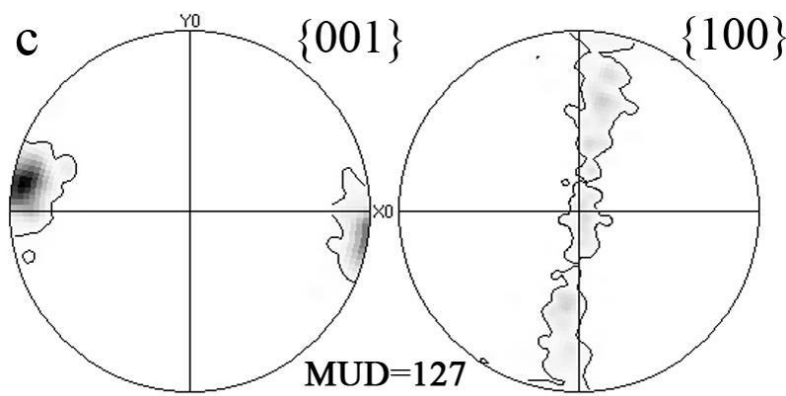
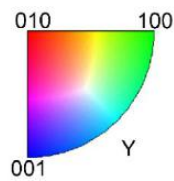
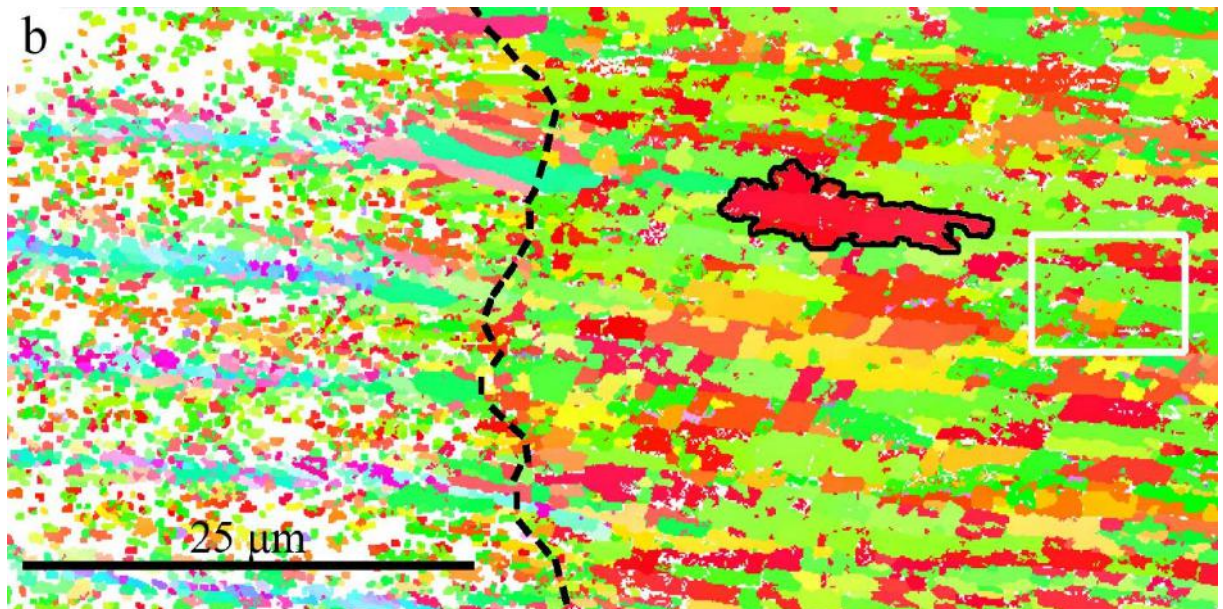
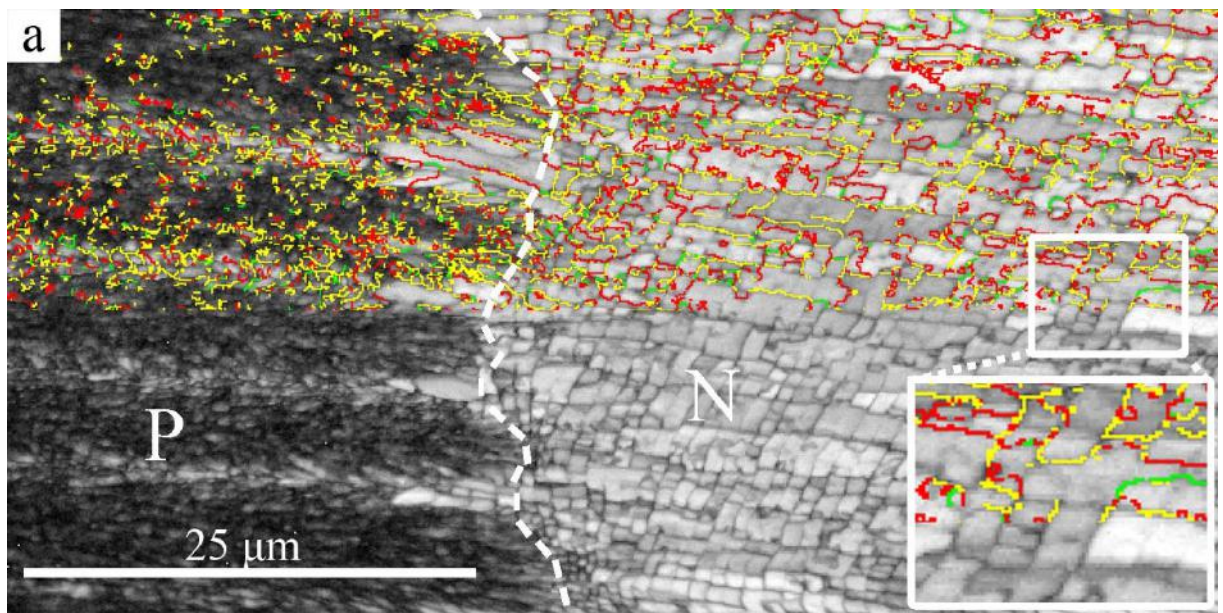
Fig. 3.12 shows the EBSD a measurement of the cross section from an area containing both, nacreous (right) and prismatic (left) layers in *Anodonta cygnea*. Fig. 3.12a shows the band contrast map. The parallel nacre lamellae can clearly be seen from the cross section. Corresponding to the texture shown in Fig. 3.11a, the prisms also show a composition of spherulites in the cross section. Unlike *Pinctada fucata*, there is no obvious gap between the prismatic and nacreous layer (see the dashed lines). One can however observe that there are needle-shaped crystallites between the prismatic and nacreous layers. The upper half of the BC map is superimposed by grain boundaries with orientation angles of $63.8^\circ \pm 2^\circ$ (red), $52.4^\circ \pm 2^\circ$ (green) and $> 2^\circ$ (yellow). The inset shows that the grain boundaries exist across and between the nacre lamellae.

Fig. 3.12b is the corresponding orientation information map of Fig. 3.12a. Both layers are indexed using aragonite lattice parameters. The colour key of both layers is shown under the orientation information map. The index rate in nacreous layer is much higher than the one in prismatic layer. The colours in nacreous layer show a patchy pattern similar to Fig. 3.9b. A colour (orientation) cluster has been selected surrounded by a black line. It is seen that the colour cluster form so-called ‘towergrain’, which grows through several layers of organic boundaries. The fragmentary distribution of the colours in the prismatic layer corresponds to Fig. 3.11b.

Figs. 3.12c and 3.12d show collective pole figures and the misorientation angle distribution in the nacreous layer of *Anodonta cygnea*, respectively. Figs. 3.12e and 3.12f are equivalent figures of the prismatic layer. In the nacreous layer, the *c*-axis of aragonite crystallites is well co-oriented almost perpendicular to the boundary between the prismatic and nacreous layers. The misorientation angles around 63.8° are the largest fraction. In the prismatic layer, the *c*-axis of aragonite crystallites centres in the direction parallel to the long axis of the prism however with large dispersion. Fig. 3.12d shows the corresponding distribution of misorientation angles. The misorientation is maximal around 63.8° but it is much lower than in nacreous layer. In conclusion, the aragonite crystallites in the prismatic layer are less co-oriented than in the nacreous layer.

The EBSD measurement has also been undertaken on the nacreous layer of another sample (see Appendix IV) and shows ‘towergrains’ across the nacre lamellae.

3.2 Crystallography orientation of samples



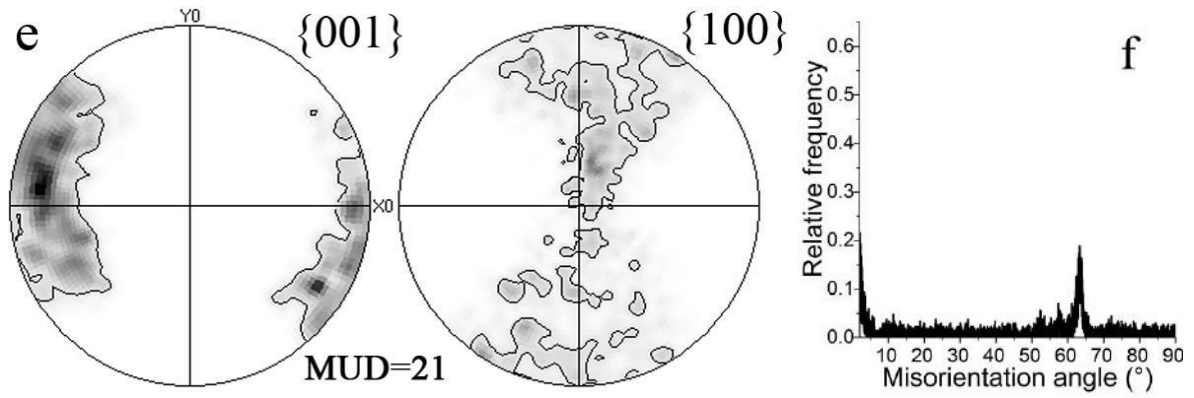


Fig. 3.12 EBSD measurement of cross section of *Anodonta cygnea*. (a) Band contrast map with grain boundaries with misorientation angles of $63.8^\circ \pm 2^\circ$ (red), $52.4^\circ \pm 2^\circ$ (green) and $> 2^\circ$ (yellow). (b) Orientation information map of (a). The white and black dashed lines represent the broadened boundary between nacreous and prismatic layers. (c) Pole figures of {001} and {100} corresponding to the nacreous layer (right part) in (b). (d) Misorientation angle distribution in the nacreous layer. (e) Pole figures of {001} and {100} corresponding to the prismatic layer (left part) in (b). (f) Misorientation angle distribution in the prismatic layer.

Raman measurements on lateral section of *Anodonta cygnea*

In addition to the EBSD measurements, the possibility to use polarized Raman spectroscopy as a tool to evaluate the orientation and variation of the *a*- and *b*-axis in the nacreous layer of *Anodonta cygnea* was expected.

First the relative intensities of all Raman modes under different polarization configurations were calculated. Then rotational Raman measurements on a reference single-crystal of aragonite along the *c*-axis were done to obtain the experimental intensities of selected Raman modes. Finally, mappings were processed on nacreous and prismatic layers along the *c*-axis to show the orientational variation of the *a*- or *b*-axis.

Calculation of relative Raman intensity

For an oriented single crystal, the intensity of a certain Raman mode depends on the directions of the polarization vectors of the incident and scattered light relative to the crystal axes. According to group theory, the relative intensity of selected Raman modes can be expressed as follow (Munisso *et al.*, 2009):

$$I \propto |\mathbf{e}_I \cdot \boldsymbol{\alpha}_{ij} \cdot \mathbf{e}_S|^2 \quad (3.1)$$

3.2 Crystallography orientation of samples

where I is the scattered Raman intensity, \mathbf{e}_I and \mathbf{e}_S are the unit polarization vectors of the electric field of the incident and scattered light, respectively. Under parallel and crossed polarization \mathbf{e}_I and \mathbf{e}_S are expressed as follows:

$$\begin{aligned}\mathbf{e}_I^{\parallel} &= (0 \ 1 \ 0), \mathbf{e}_S = \begin{pmatrix} 0 \\ 1 \\ 0 \end{pmatrix} \text{ and} \\ \mathbf{e}_I^{\perp} &= (1 \ 0 \ 0), \mathbf{e}_S = \begin{pmatrix} 0 \\ 1 \\ 0 \end{pmatrix}\end{aligned}\quad (3.2)$$

where the superscripts \parallel and \perp stand for parallel and crossed polarization, respectively. α_{ij} is the Raman polarizability tensor used to describe the Raman excitation in three-dimensional space. The second rank tensor is symmetric so that only six independent elements need to be considered. The tensor is expressed as:

$$\alpha_{ij} = \begin{pmatrix} \alpha_{xx} & \alpha_{xy} & \alpha_{xz} \\ \alpha_{yx} & \alpha_{yy} & \alpha_{yz} \\ \alpha_{zx} & \alpha_{zy} & \alpha_{zz} \end{pmatrix}, ij = x, y, z \quad (3.3)$$

Each Raman mode has a corresponding Raman activity and is determined by the appearance of Raman modes in a given polarization configuration. A single crystal can show several types of Raman modes due to its symmetry. In group theory, Mulliken Symbols (*Band and Avishai, 2013*) (see Table 3.1) are used to label irreducible representations with different symmetries.

3.2 Crystallography orientation of samples

Table 3.1 Symbols of irreducible representations for different types of Raman modes (*Band and Avishai, 2013*)

Symbol	Property
A	singly degenerate state which is symmetric with respect to rotation about the principal axis
B	singly degenerate state which is antisymmetric with respect to rotation about the principal axis
E	doubly degenerate
T	triply degenerate
subscript 1	(used on A or B) symmetric upon C_2 rotation perpendicular to the principle axis
subscript 2	(used on A or B) antisymmetric upon C_2 rotation perpendicular to the principle axis
subscript g	symmetric under inversion
subscript u	antisymmetric under inversion
prime(')	symmetric with respect to a horizontal mirror plane
Double prime ('')	antisymmetric with respect to a horizontal mirror plane

The space group of aragonite is D_{2h}^{16} or Pnma (62), the point group is mmm. It has 4 formula units per orthorhombic unit cell and hence, a total of 20 atoms; according to the character table of the point group mmm, its 57 optical modes are as follows:

$$\Gamma_{total} = 9A_g + 6A_u + 6B_{1g} + 8B_{1u} + 9B_{2g} + 5B_{2u} + 6B_{3g} + 8B_{3u} \quad (3.4)$$

$A_g, B_{1g}, B_{2g}, B_{3g}$ are Raman active, B_{1u}, B_{2u}, B_{3u} are infrared active, and A_u is an inactive mode. From the Bilbao crystallographic server, it shows that the Raman tensors associated with $A_g, B_{1g}, B_{2g}, B_{3g}$ are:

$$\alpha(A_g) = \begin{pmatrix} a & 0 & 0 \\ 0 & b & 0 \\ 0 & 0 & c \end{pmatrix}, \alpha(B_{1g}) = \begin{pmatrix} 0 & d & 0 \\ d & 0 & 0 \\ 0 & 0 & 0 \end{pmatrix}, \alpha(B_{2g}) = \begin{pmatrix} 0 & 0 & e \\ 0 & 0 & 0 \\ e & 0 & 0 \end{pmatrix}, \alpha(B_{3g}) = \begin{pmatrix} 0 & 0 & 0 \\ 0 & 0 & f \\ 0 & f & 0 \end{pmatrix} \quad (3.5)$$

where a, b, c, d, e and f are the Raman tensor elements.

If the crystal is placed on the XY-table in an arbitrary orientation, an Euler's matrix \mathbf{U} is used to transform the crystal coordinate (o, x, y, z) into the experimental one (O, X, Y, Z). The transformed polarizability tensor is denoted as α'_{ij} :

$$\alpha'_{ij} = \mathbf{U}^T \cdot \alpha_{ij} \cdot \mathbf{U} \quad (3.6)$$

where \mathbf{U}^T is the transpose of \mathbf{U} . In an intrinsic rotation with x-convention, \mathbf{U} consists of three orthogonal transformation matrices:

$$\mathbf{U}(\alpha, \beta, \gamma) = \mathbf{U}_Z(\gamma) \cdot \mathbf{U}_X(\beta) \cdot \mathbf{U}_Z(\alpha) \quad (3.7)$$

$\mathbf{U}(\alpha, \beta, \gamma)$ uses post-multiply, and $\mathbf{U}_Z(\gamma), \mathbf{U}_X(\beta), \mathbf{U}_Z(\alpha)$ are given by:

$$\mathbf{U}_Z(\gamma) = \begin{pmatrix} \cos\gamma & \sin\gamma & 0 \\ -\sin\gamma & \cos\gamma & 0 \\ 0 & 0 & 1 \end{pmatrix}, \mathbf{U}_X(\beta) = \begin{pmatrix} 1 & 0 & 0 \\ 0 & \cos\beta & \sin\beta \\ 0 & -\sin\beta & \cos\beta \end{pmatrix}, \mathbf{U}_Z(\alpha) = \begin{pmatrix} \cos\alpha & \sin\alpha & 0 \\ -\sin\alpha & \cos\alpha & 0 \\ 0 & 0 & 1 \end{pmatrix} \quad (3.8)$$

where α is the angle between x- and the N-axis, firstly rotated around the z-axis; β is the angle between z- and the Z-axis, secondly rotated around the N-axis; γ is the angle between N- and the X-axis, thirdly rotated around the Z-axis; the N intersection line is the line of nodes. Fig. 3.13 shows the process of Euler's rotation. In the experiment, the initial orientation of the crystal (o, x, y, z) is identical to the experimental coordinate (O, X, Y, Z), thus $\alpha = \beta = \gamma = 0^\circ$.

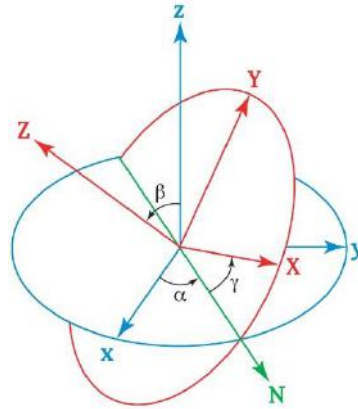


Fig. 3.13 Euler's rotation theorem. Figure presents the intrinsic rotation using the x-convention (Lionel Brits, 2008).

In the experiment, the single-crystal of aragonite is rotated in steps of 5° for every measurement. The tensor after rotation is expressed:

$$\alpha_{IJ} = \mathbf{U}'^T(\theta) \cdot \alpha'_{ij} \cdot \mathbf{U}'(\theta) \quad (3.9)$$

where α_{IJ} is the rotated Raman polarizability tensor; $\mathbf{U}'(\theta)$ is the orthogonal transformation matrix; $\mathbf{U}'^T(\theta)$ is the transpose of $\mathbf{U}'(\theta)$; θ is the rotated angle. Rotating along a different axis (X, Y or Z), $\mathbf{U}'(\theta)$ can be expressed as:

$$\mathbf{U}'_{Ox}(\theta) = \begin{pmatrix} 1 & 0 & 0 \\ 0 & \cos\theta & -\sin\theta \\ 0 & \sin\theta & \cos\theta \end{pmatrix}; \mathbf{U}'_{Oy}(\theta) = \begin{pmatrix} \cos\theta & 0 & \sin\theta \\ 0 & 1 & 0 \\ -\sin\theta & 0 & \cos\theta \end{pmatrix}; \mathbf{U}'_{Oz}(\theta) = \begin{pmatrix} \cos\theta & -\sin\theta & 0 \\ \sin\theta & \cos\theta & 0 \\ 0 & 0 & 1 \end{pmatrix} \quad (3.10)$$

where $\mathbf{U}'_{OX}(\theta)$, $\mathbf{U}'_{OY}(\theta)$, $\mathbf{U}'_{OZ}(\theta)$ stand for rotation matrices around X, Y or Z-axis for a given angle θ , respectively. In the experiment, the single-crystal of aragonite is rotated around the Z-axis.

Substituting Eqs. (3.2), (3.3) and (3.5)-(3.10) into Eq. (3.1), the relative intensity of different Raman modes is obtained under different polarization configurations (see Table 3.2).

Two geometries were measured on aragonite under parallel and crossed polarizations, $\bar{Z}(YY)Z$ and $\bar{Z}(XY)Z$, respectively. According to table 3.2, only intensities of A_g and B_{1g} modes are detectable.

Calculated and experimental Raman frequencies of different modes of aragonite have already been studied by former researchers (Carteret et al., 2013; De La Pierre et al., 2014). The 30 calculated Raman modes of aragonite are shown in Table 3.3.

In unpolarized Raman measurements, the frequency at $1095.3 \text{ cm}^{-1}(A_g)$ has the strongest intensity and the modes at $704.2 \text{ cm}^{-1}(A_g)$ and $701.2 \text{ cm}^{-1}(B_{3g})$ have the second strongest intensities. According to table 3.3, B_{3g} is undetectable under YY or XY scattering configuration, hence this work will focus on the 1095.3 cm^{-1} calculated excitation (which is 1087 cm^{-1} in the experiment). The depolarization ratio of the A_g mode can be calculated to be:

$$\rho \propto \frac{I_{XY}^{\perp}}{I_{YY}^{\parallel}} = \frac{(a-b)^2 \sin^2 \theta \cos^2 \theta}{(a \sin^2 \theta + b \cos^2 \theta)^2}$$

3.2 Crystallography orientation of samples

Table 3.2 Relative intensities of Raman modes of aragonite under different polarization configurations.

Polarization geometries in Porto's notation	$I_{IJ}(A_g) \propto$	$I_{IJ}(B_{1g}) \propto$	$I_{IJ}(B_{2g}) \propto$	$I_{IJ}(B_{3g}) \propto$
A(XX)D	$(b\sin^2\theta + a\cos^2\theta)^2$	$-\frac{d^2}{2}(\cos 4\theta - 1)$	0	0
A(XY)D	$(a - b)^2\sin^2\theta\cos^2\theta$	$\frac{d^2}{2}(\cos 4\theta + 1)$	0	0
A(XZ)D	0	0	$\frac{e^2}{2}(\cos 2\theta + 1)$	$-\frac{f^2}{2}(\cos 2\theta - 1)$
A(YX)D	$(a - b)^2\sin^2\theta\cos^2\theta$	$\frac{d^2}{2}(\cos 4\theta + 1)$	0	0
A(YY)D	$(a\sin^2\theta + b\cos^2\theta)^2$	$-\frac{d^2}{2}(\cos 4\theta - 1)$	0	0
A(YZ)D	0	0	$-\frac{e^2}{2}(\cos 2\theta - 1)$	$\frac{f^2}{2}(\cos 2\theta + 1)$
A(ZX)D	0	0	$\frac{e^2}{2}(\cos 2\theta + 1)$	$-\frac{f^2}{2}(\cos 2\theta - 1)$
A(ZY)D	0	0	$-\frac{e^2}{2}(\cos 2\theta - 1)$	$\frac{f^2}{2}(\cos 2\theta + 1)$
A(ZZ)D	c^2	0	0	0

3.2 Crystallography orientation of samples

Table 3.3 Calculated frequencies of Raman modes in aragonite (*Carteret et al., 2013; De La Pierre et al., 2014*).

No.	Symmetry	Calculated Frequency (cm ⁻¹)	No.	Symmetry	Calculated frequency (cm ⁻¹)
1	<i>A_g</i>	148.7	16	<i>B_{2g}</i>	182.5
2		161.9	17		207.2
3		195.8	18		249.2
4		205.0	19		260.7
5		280.2	20		278.7
6		704.2	21		714.6
7		862.8	22		911.8
8		1095.3	23		1091.6
9		1473.9	24		1591.8
10	<i>B_{1g}</i>	97.4	25	<i>B_{3g}</i>	101.3
11		152.1	26		167.6
12		199.0	27		177.8
13		213.4	28		271.4
14		705.5	29		701.2
15		1463.9	30		1415.0

3.2 Crystallography orientation of samples

Rotational measurements on a reference single-crystal of aragonite were carried out. The crystal was therefore placed on a rotation platform with the initial orientation of a -, b -, and c -axis parallel to the X, Y and Z direction of the platform, respectively (see Fig. 2.8). The crystal was rotated around the c -axis in steps of 5° and Raman spectra were measured under both, parallel and perpendicular configurations. All spectra were then processed and fitted using OriginPro software. The depolarization ratio of the mode at 1087 cm^{-1} was obtained by dividing the area of the 1087 cm^{-1} mode under XY configuration by its area under YY configuration. The result is shown in Fig. 3.14. The data were fitted using a Gaussian function. The area is 73.28, the baseline is at height 0.046, FWHM is 33.09, the peak centre is at 41.1° and the highest value of the depolarization ratio is 2.08. Using the depolarization ratio, one can also minimize the influence of instrumental factors.

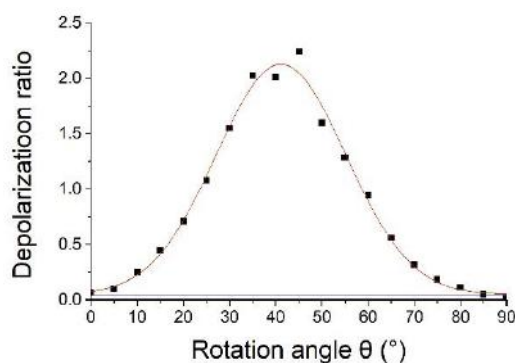


Fig. 3.14 Variation of the relative intensity of the depolarization ratio by rotating the aragonite crystal

Mapping using Raman spectroscopy in *Anodonta cygnea* was done in both, parallel and cross polarization with a lateral step length of $1\ \mu\text{m}$. Fig. 3.15 shows the maps of the depolarization ratio of the mode at 1087 cm^{-1} for nacreous and prismatic layers, respectively. Fig. 3.15a shows the nacreous layer under the optical microscope and Fig. 3.15b is the polarization ratio map corresponding to the black square shown in Fig. 3.15a ($25\ \mu\text{m} \times 40\ \mu\text{m}$). From the polarization ratio map, it is seen that the crystal orientation of nacre tablets in the nacreous layer is not homogeneous. Fig. 3.15c shows the prismatic layer under the optical microscope and Fig. 3.15d shows the corresponding depolarization ratio map of the black square in Fig. 3.15c ($50\ \mu\text{m} \times 20\ \mu\text{m}$). From Fig. 3.15d one can easily distinguish the boundaries between the prisms and also an inhomogeneous distribution of the crystallite orientation in each prism. The mapping images show clearly that the a - or b -axis has orientational variations, both in nacreous and prismatic layers. The depolarization ratios show the approximate orientation of the crystallites.

3.2 Crystallography orientation of samples

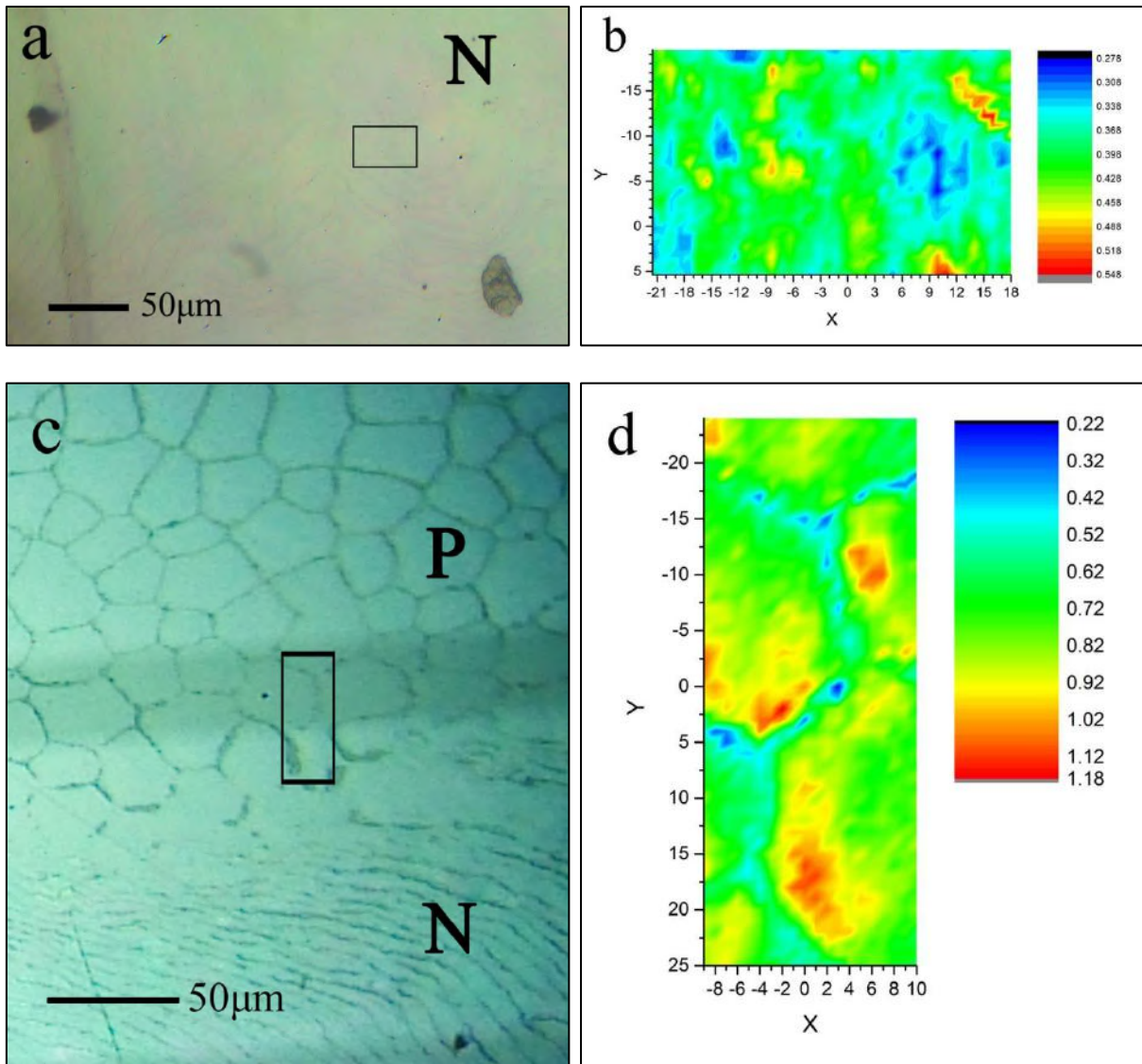


Fig. 3.15 Mapping results of Raman spectroscopy. (a) Nacreous layer under optical microscope. Black square shows the mapped area ($25 \mu\text{m} \times 40 \mu\text{m}$). (b) Depolarization rasion map of the mode at 1087 cm^{-1} of the nacreous layer corresponding to (a). (c) Prismatic layer under optical microscope. Black square shows the mapped area ($50 \mu\text{m} \times 20 \mu\text{m}$). (d) Depolarization rasion map of the mode at 1087 cm^{-1} of prismatic layer corresponding to (c)

3.2.3 *Phorcus turbinatus*

Lateral section

Fig. 3.16 shows the EBSD results of a lateral section of the nacreous layer from *Phorcus turbinatus*. Fig. 3.16a gives the band contrast (BC) image of a selected mapped area which is almost parallel to the nacre lamellae. Like the former two species, the sample was indexed using lattice parameters of aragonite. The upper half of the BC map is superimposed by grain boundaries of misorientation angles of $63.8^\circ \pm 2^\circ$ (red), $52.4^\circ \pm 2^\circ$ (green) and $> 2^\circ$ (yellow). Red and green boundaries represent misorientation angles of aragonite twins. The yellow boundaries represent misorientation angles of low-angle grain boundaries (LAGBs). Unlike previously shown in Fig. 3.7 and 3.10, the twin boundaries in this gastropod species are more widespread than in the former two samples. The inset in Fig. 3.16a shows an enlarged part of the boundaries, which are distributed around the nacre tablets.

Fig. 3.16b shows the crystallographic orientation map using IPF colouring code, corresponding to Fig. 3.16a. The Y-inset in the map shows the colour key which displays the crystallographic orientation of each indexed point with respect to the vertical direction of the measured surface. The colour distribution in Fig. 3.16b is more diverse than in Fig. 3.10b indicating more disorder than in Fig. 3.7b. The map displays mainly red, yellow and green colours, which means that the *c*-axis (blue) is not oriented along the vertical direction.

Fig. 3.16c shows collective pole figures of all indexed areas seen in Fig. 3.16b on planes {001} and {100}. It shows that the *c*-axis of all crystallites is well co-oriented and almost perpendicular to the measured surface. The MUD (multiples of uniform density) value of the pole figures is lower than in *Pinctada fucata* but higher than in *Anodonta cygnea*.

Fig. 3.16d shows the statistical distribution of misorientation angles between neighbouring crystallites. The relative frequency or the fraction of the angle around 63.8° is the only maximum and it is much higher than the related fractions of the other two species.

Because of the fibrous nature of the prismatic layer, the sample was difficult to prepare with a sufficient large surface containing both, nacreous and prismatic layers to carry out EBSD measurements. One result containing both, nacreous and prismatic layers is shown in the Appendix V. The index rate of the prismatic layer was not sufficient for quantitative analysis. Thus, the EBSD results of the cross section of *Phorcus turbinatus* on nacreous layer and prismatic layer are shown separately.

3.2 Crystallography orientation of samples

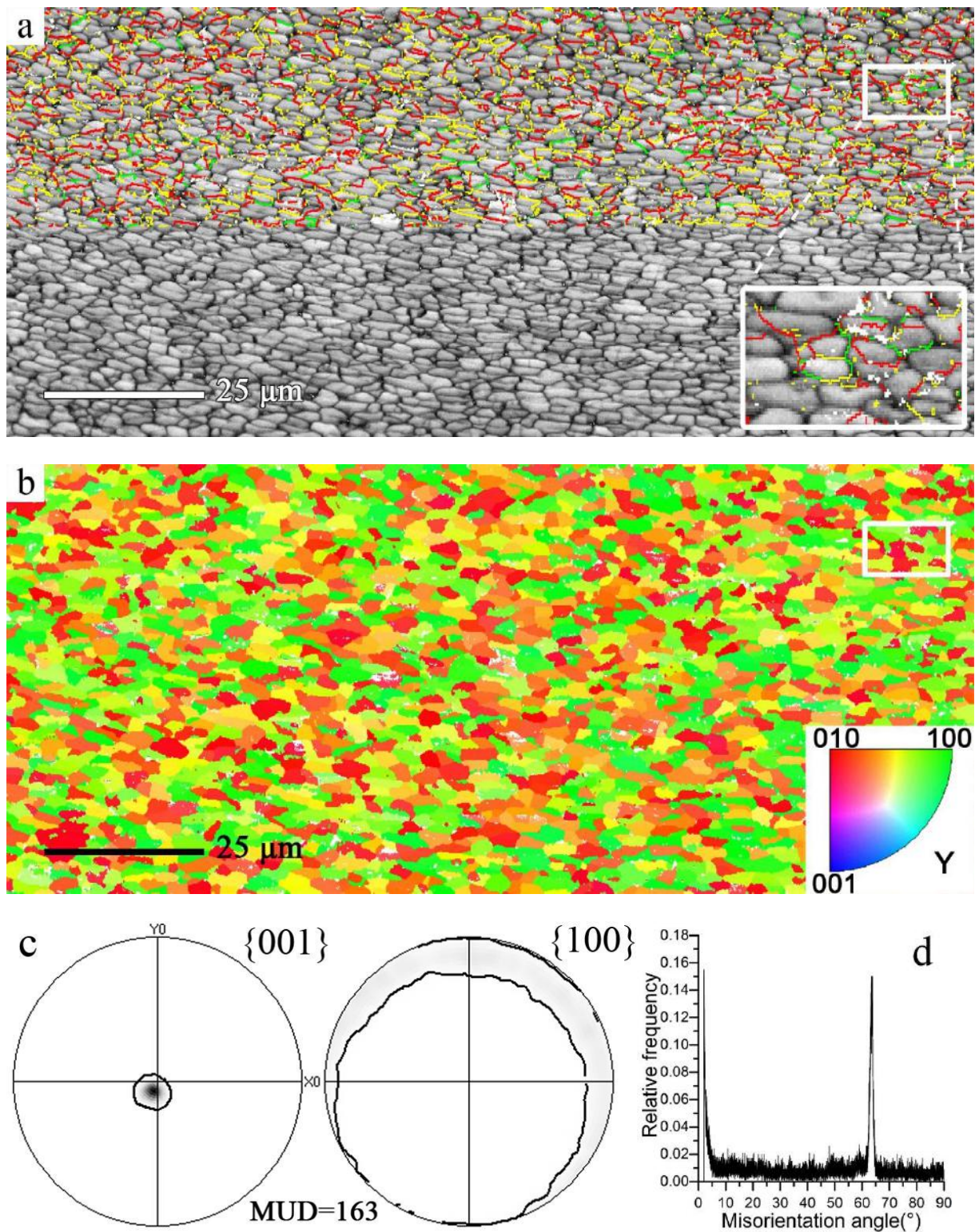


Fig. 3.16 EBSD measurement of the lateral section of the nacreous layer of *Phorcus turbinatus*. (a) Band contrast (BC) map. In the upper half of the BC map grain boundaries with misorientation angles of $63.8^\circ \pm 2^\circ$ (red), $52.4^\circ \pm 2^\circ$ (green) and $> 2^\circ$ (yellow) are marked. The inset shows an enlarged area. (b) Crystal orientation information map of (a) with orientation colour key in the lower right corner. (c) Pole figures of $\{001\}$ and $\{100\}$ corresponding to (b), the MUD value is shown below the pole figures. (d) Misorientation angle distribution of (b).

Cross section

Measurements of the cross sections were undertaken separately for the nacreous and prismatic layer.

Fig. 3.17 shows the cross section of the nacreous layer of *Phorcus turbinatus*. Fig. 3.17a shows the band contrast (BC) indexed using lattice parameters of aragonite. The boundaries across the nacre lamellae are so dominant that they divide the surface into ‘stripes’ (probably filled with organic matter in between). The upper half of the BC map is superimposed with grain boundaries showing misorientation angles of $63.8^\circ \pm 2^\circ$ (red), $52.4^\circ \pm 2^\circ$ (green) and $> 2^\circ$ (yellow). The inset in Fig. 3.16a shows an enlarged part of the grains and boundaries. The boundaries between the ‘stripes’ are non-linear.

Fig. 3.17b presents the crystallographic orientation map corresponding to Fig. 3.17a using the IPF colour code. The Y-inset shows the colour key. The index Y at the corner indicates how the crystallites are oriented towards the vertical direction of the measured surface. It is seen that the axis $\langle 010 \rangle$ (red), $\langle 100 \rangle$ (green) and $\langle 001 \rangle$ (blue) are not pointing towards vertical direction. It occurs mainly the colour between $\langle 010 \rangle$ and $\langle 001 \rangle$ and between $\langle 001 \rangle$ and $\langle 100 \rangle$. Similar to Fig. 3.17a, the colours (i.e. different crystallographic orientations) also show a distribution of ‘stripes’ or clusters. One of the clusters has been selected and is displayed inside a black frame.

Fig. 3.17c shows the collective pole figures of all indexed areas of Fig. 3.17b for $\{001\}$ and $\{100\}$. It occurs that the *c*-axis of the crystallites is well co-oriented and almost parallel to the measured surface. The direction of the *c*-axis is therefore identical to the extension direction of the ‘stripes’. The MUD (multiples of uniform density) value of the pole figures is lower than the one of *Pinctada fucata* but similar to the one of *Anodonta cygnea*.

Fig. 3.17d gives the statistical distribution of the misorientation angles between neighbouring crystallites. There are three main fractions in the angle distribution, one is around 57.5° and the others occur around 52.4° and 64.8° .

3.2 Crystallography orientation of samples

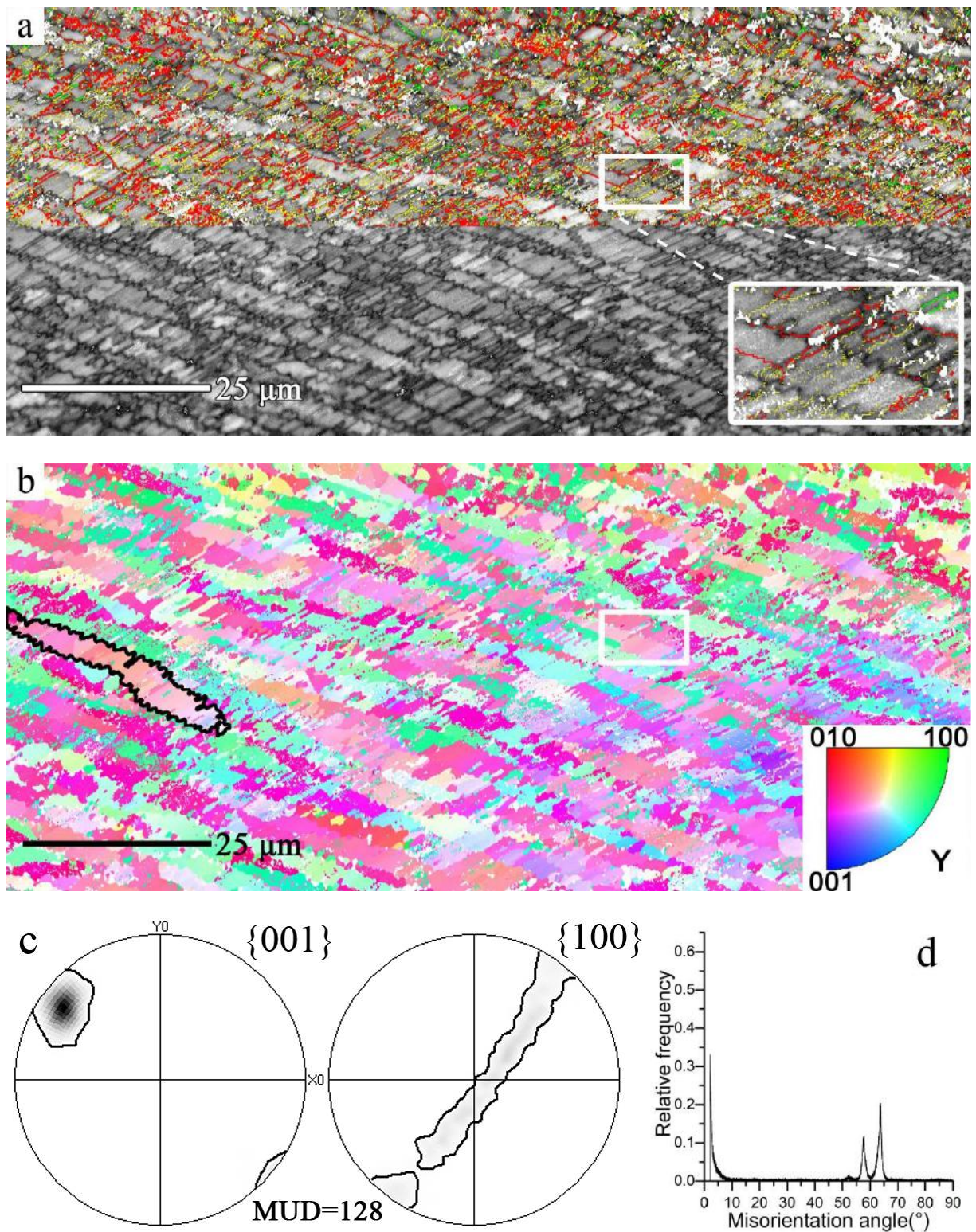


Fig. 3.17 EBSD measurement of the cross section of the nacreous layer of *Phorcus turbinatus*. (a) Band contrast (BC) map. In the upper half of the BC map grain boundaries with misorientation angles of $63.8^{\circ} \pm 2^{\circ}$ (red), $52.4^{\circ} \pm 2^{\circ}$ (green) and $> 2^{\circ}$ (yellow) are marked. The inset shows an enlarged area. (b) Crystal orientation information map of (a). The orientation colour key appears in the lower right corner. (c) Pole figures of {001} and {100} corresponding to (b). (d) Misorientation angle distribution of (b).

Fig. 3.18 shows the results of the EBSD measurement of the cross section of the prismatic layer of *Phorcus turbinatus*. Fig. 3.18a gives the band contrast map. From the band contrast map, it is seen that the prisms have a fibrous texture, which also corresponds to the SEM results of Fig. 3.6 but differs from the textures of the other two species shown in Figs. 3.8a and 3.11a. Within one prism, the fibrous crystallites are arranged in a feather-like pattern. One prism has been selected and was superimposed by grain boundaries with orientation angles of $63.8^\circ \pm 2^\circ$ (red), $52.4^\circ \pm 2^\circ$ (green) and $> 2^\circ$ (yellow).

Fig. 3.18b shows the crystal orientation information map corresponding to Fig. 3.18a. The colour key is shown in the right top corner. The colours are selected with respect to the normal direction of the measured surface. Similar to the texture shown in Fig. 3.18a, the prisms show a pinnate pattern with alternatively changing colours in each of the prisms. The prisms can be easily distinguished from each other by the colour differences.

Fig. 3.18c presents the collective pole figures of all crystallites from Fig. 3.18b on {001} and {100}. It shows that the *c*-axis of all indexed crystallites has a preferred orientation which is about 45° to the normal direction of the measured surface. The inclined direction of the *c*-axis is identical to the extended axis of the prisms. The MUD value (degree of co-orientation) is very low compared to the MUD value of the nacreous layer, which means that the crystallites in prismatic layer are less co-oriented than in the nacreous layer.

Fig. 3.18d shows the statistical result of the misorientation angles between neighbouring crystallites. The angle of 63.8° is the most dominant group of boundaries. Besides, there are also concentrations around 12° , 52.4° and 57.5° .

From the EBSD data in the Appendix V, there are no sufficient results to separate the relationship of crystal orientations between the nacreous and prismatic layers, but there is no obvious boundary between the two layers in the BC map.

3.2 Crystallography orientation of samples

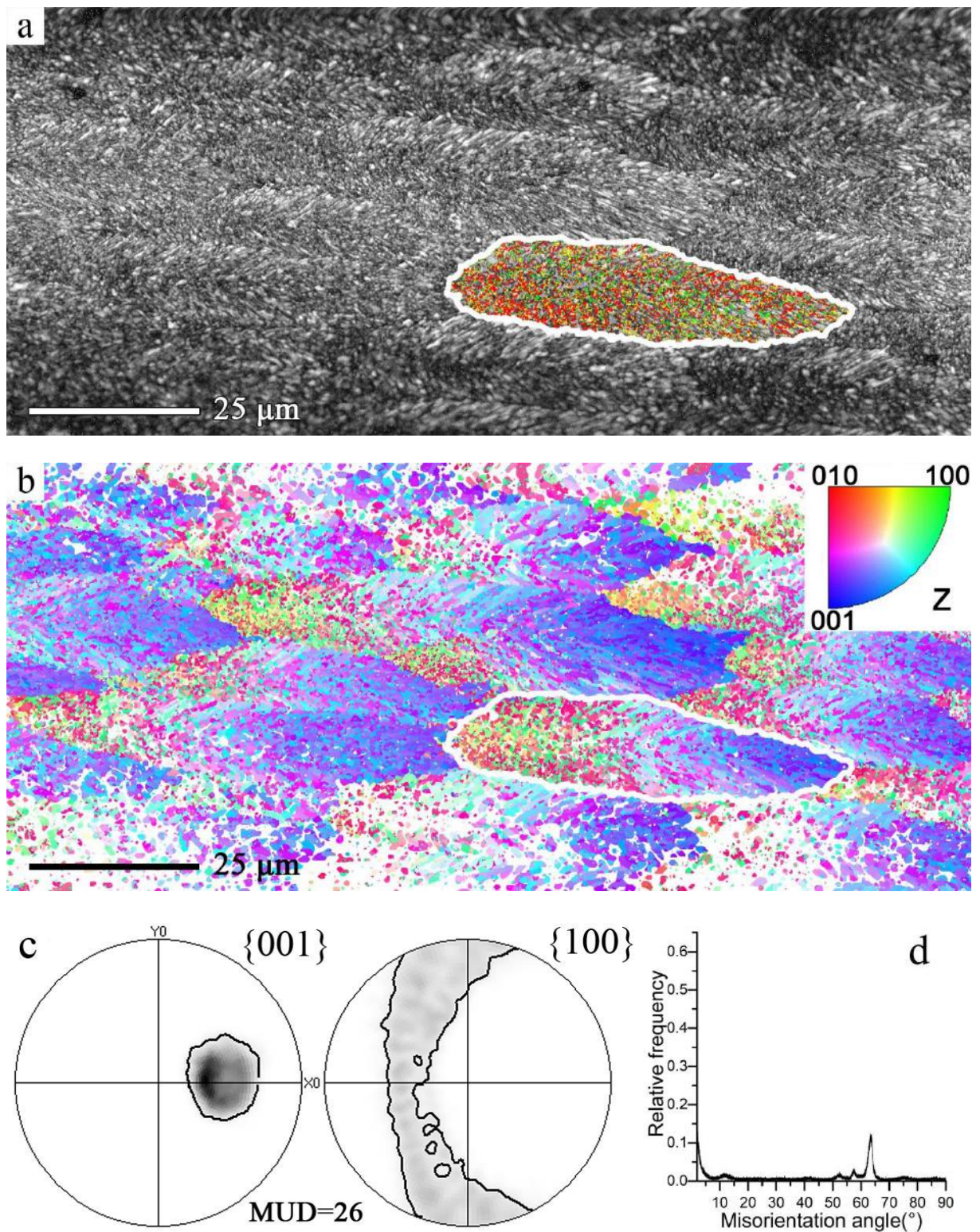


Fig. 3.18 EBSD measurement of the cross section of prismatic layer of *Phorcus turbinatus*. (a) Band contrast (BC) map. One prism selected in a white frame and superimposed by grain boundaries with misorientation angles of $63.8^{\circ} \pm 2^{\circ}$ (red), $52.4^{\circ} \pm 2^{\circ}$ (green) and $> 2^{\circ}$ (yellow) are marked. (b) Crystal orientation information map of (a). The orientation colour key is shown in the upper right corner. (c) Pole figures of {001} and {100} corresponding to (b). (d) Misorientation angle distribution of (b).

3.3 Chemical composition of samples

Six elements, Mg, S, Ca, Mn, Sr, Ba, were determined qualitatively by microprobe mappings and quantitatively using their profile analyses. Among the elements, S is mainly distributed in the organic matrix and the other elements are crucial for the biomineralization of calcium carbonate polymorphs. However, Mn, Sr and Ba show very low contents and they are relatively homogeneously distributed in the samples. The results of the calcium distribution are similar to the BSE images. The results of BSE images and the contents of S, Mg and Sr are presented as follows.

3.3.1 *Pinctada fucata*

Fig. 3.19 shows results of the electron microprobe mapping with the profile analysis of a lateral section of *Pinctada fucata*.

Fig. 3.19a shows the BSE image of the mapped area on the lateral section including the nacreous layer (N) and prismatic layer (P). Heavier atoms with larger atomic number are stronger scatter in SEM. The backscattered-electron (BSE) images can therefore be used to observe the compositional variations quantitatively. The brighter area on the image stands for a concentration of ions with heavier average atomic number. The white arrow in the BSE image represents the quantitative profile of a line analysis. The profile starts in the prismatic layer, crosses the interfacial area and ends in the nacreous layer. It can be observed that there are gaps between the prisms. Between the prismatic and nacreous layers there is a broad dark area.

Figs. 3.19b, 3.19c and 3.19d show the concentrations of sulphur, magnesium, and strontium using a brightness scale, respectively. Brighter areas indicate higher concentrations. Reversely to the BSE figure, sulphur shows a much higher concentration in the dark area of the BSE image. It surrounds the prisms and also exists in the interfacial area between the two parallel layers. Magnesium occurs primarily in the prismatic layer. Strontium occurs in both, prismatic and nacreous layer but in the nacreous layer concentration is slightly higher.

Fig. 3.19e shows the results of the three elements given in weight percent. Above the three lines, there is a corresponding BSE image shown where the line scan has been processed for quantitative analysis (arrow in Fig. 3.19a). For the line scan, 100 points with a step width of 3.30 μm were measured. The concentration of sulphur is about 0.5 wt. % in the dark area and 0.05 wt. % in the bright area in Fig. 3.19a. Magnesium has about 1.1 wt. % in the prisms (left part of the first dashed line) and almost vanishes in the nacreous layer (right part of the second dashed line). Due to the detection limit, strontium scatters around zero values but indicates a rising concentration from the prismatic to the nacreous layer.

3.3 Chemical composition of samples

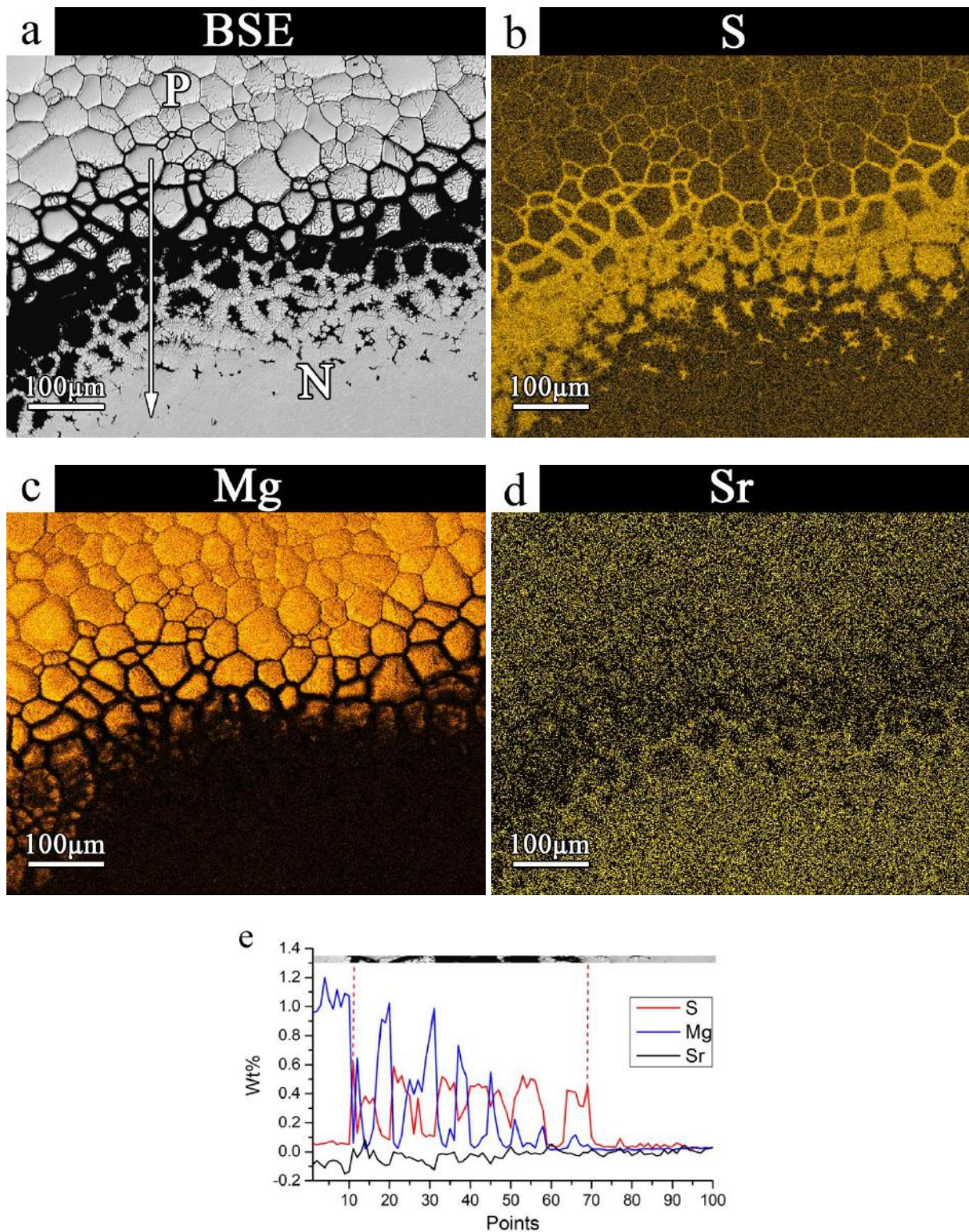


Fig. 3.19 Electron microprobe analyses on a lateral section of *Pinctada fucata*. (a) The BSE image shows prismatic (P) and nacreous (N) layer. The white arrow indicates a line for quantitative profile analysis of elements. (b)- (d) Intensity maps of S, Mg and Sr corresponding to location in (a), respectively. (e) Results of quantitative analyses of S, Mg and Sr. One point corresponds to 3.30 µm of the length scale along the arrow in (a).

Fig. 3.20 shows the results of the electron microprobe mapping and the profile analysis of a cross section of *Pinctada fucata*.

BSE image is given in Fig. 3.20a to show the mapped area including the nacreous (N) and prismatic (P) layer. The white arrow in the BSE image represents a line of the quantitative profile analysis, starting in the prismatic layer and ending in the nacreous layer. 80 points were measured with a width of 1.15 μm per step.

Figs. 3.20b, 3.20c and 3.20d show concentrations of sulphur, magnesium, and strontium using a brightness scale, respectively. Since brighter areas indicate higher ion concentrations, it is seen that sulphur occurs a higher concentration between the prisms, as well as in the area between the prisms and the nacreous layer. Similar to Fig. 3.19c, magnesium was found only in the prismatic layer in Fig. 3.20c. From the cross section, it occurs that magnesium shows weak parallel concentration changes across the prisms in the direction perpendicular to their long axis. Strontium occurs in both prismatic and nacreous layers and shows a rather homogeneous distribution.

Fig. 3.20e shows the results of the ion concentrations in weight percent of three elements. Above the element lines, there is the corresponding BSE image following the white arrow in Fig. 3.20a. The red dashed line indicates the boundary between the prismatic (left) and nacreous layers (right). The concentration of sulphur is almost equal in both layers but perhaps slightly higher in the boundary itself. Magnesium has a higher concentration in the prisms (~0.55 wt. %) than in the nacreous layer (almost zero). Due to the detection limit and data scattering, the strontium was negative values but similar to Fig. 3.19e, it shows a higher concentration in the nacreous layer than in the prismatic layer.

3.3 Chemical composition of samples

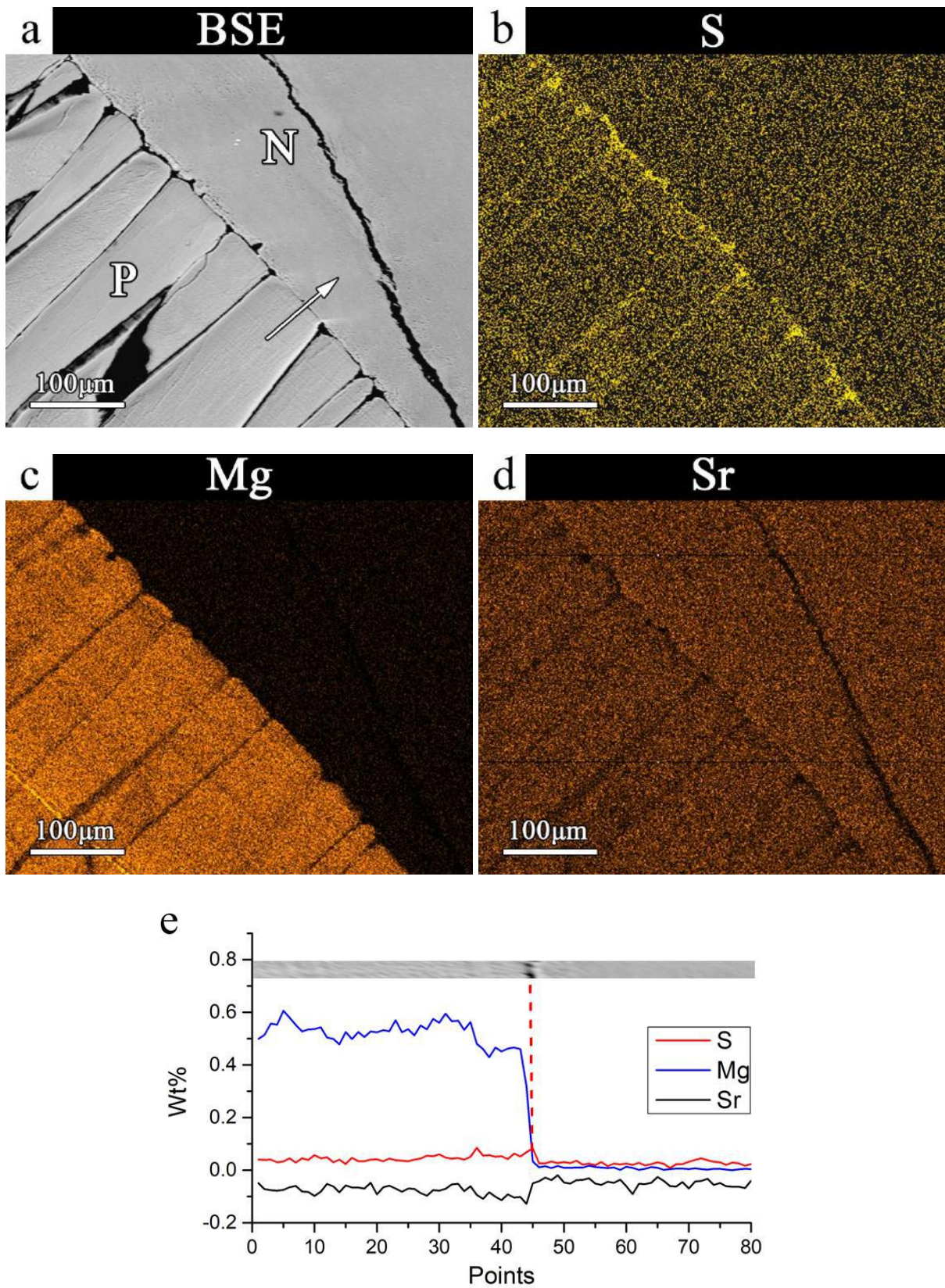


Fig. 3.20 Electron microprobe data of a cross section of *Pinctada fucata*. (a) BSE image includes prismatic (P) and nacreous (N) layers. The white arrow runs along the quantitative line profile analysis. (b)-(d) Intensity maps of S, Mg and Sr corresponding to (a), respectively. (e) Quantitative analyses data of S, Mg and Sr. One point corresponds to a step of 1.15 μm.

3.3.2 *Anodonta cygnea*

Fig. 3.21 shows the results of electron microprobe mapping and profile analysis of a lateral section of *Anodonta cygnea*.

Fig. 3.21a provides the BSE image of the measured area including nacreous (N) and prismatic (P) layer. The white arrow indicates the quantitative line profile elemental analysis, it starts in the prismatic layer and ends in the nacreous layer. 90 points were measured using with a step width of 2.70 μm . From the BSE image, one can observe dark lines between the prisms and each prism is separated into smaller units. Unlike the lateral section of *Pinctada fucata*, there is no dark area in the interfacial area between the two layers.

The concentrations of sulphur, magnesium, and strontium are shown in Figs. 3.21b, 3.21c and 3.21d based on a brightness scale. Sulphur presents a higher concentration around the prisms and a homogeneous distribution in the nacreous layer. It is confirmed that sulphur does not concentrate between the nacreous and prismatic layer. Different from *Pinctada fucata*, magnesium and strontium occur in both, prismatic and nacreous layers homogeneously.

Fig. 3.21e shows the results of quantitative concentration levels of three elements in weight percent. Above the three element lines, there is the corresponding BSE image shown from Fig. 3.21a. Red dashed lines indicate boundaries between the prisms, where the concentration of sulphur is higher (~0.07 wt. %) than inside the prisms and the nacreous layer. Magnesium shows a low concentration in both layers. Different from *Pinctada fucata*, strontium has a relatively higher average value (~0.07 wt. %) than magnesium.

3.3 Chemical composition of samples

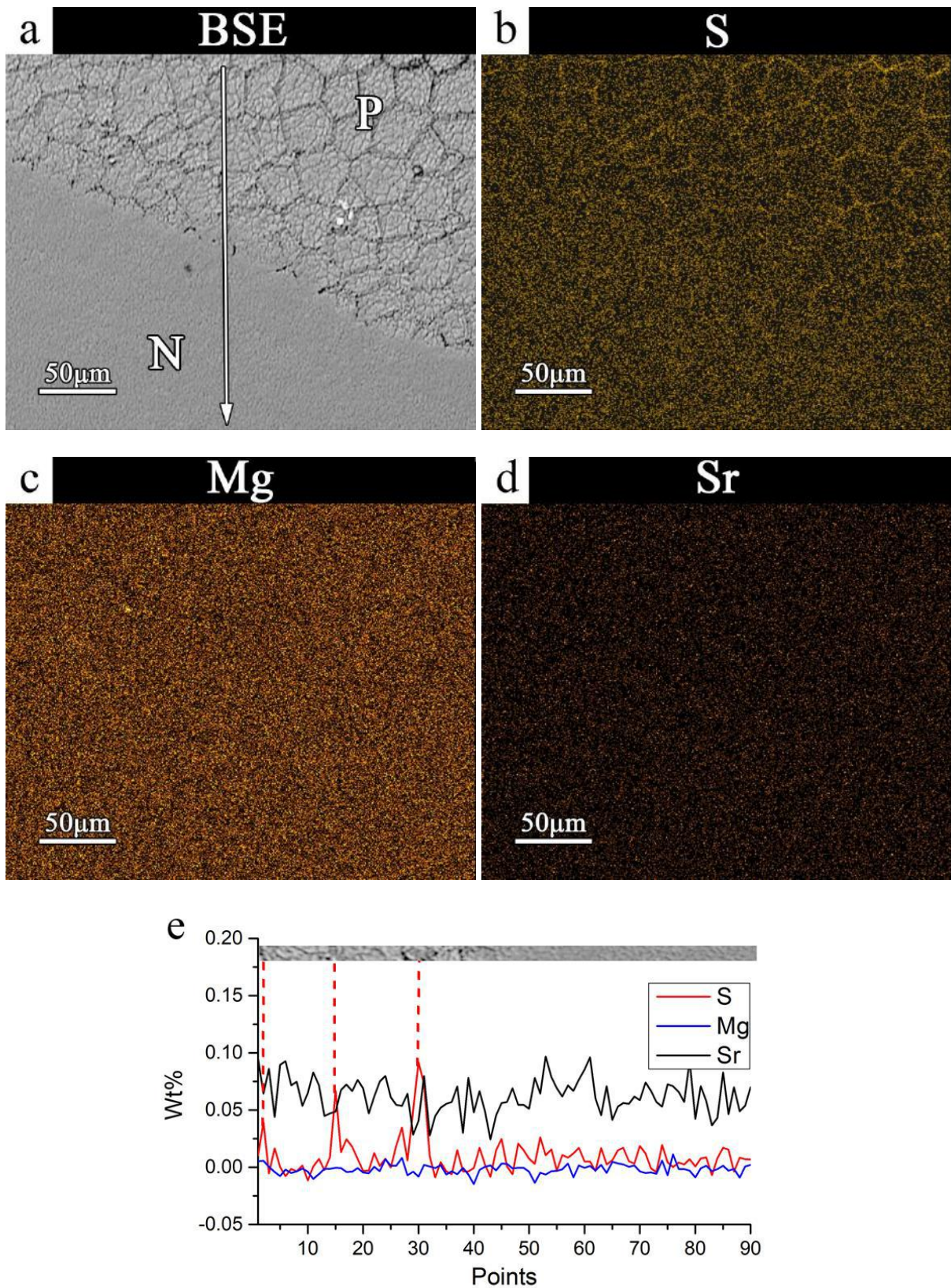


Fig. 3.21 Electron microprobe analyses data of a lateral section of *Anodonta cygnea*. (a) BSE image including prismatic (P) and nacreous (N) layers. The white arrow indicates the quantitative line profile analysis. (b)- (d) Intensity maps of S, Mg and Sr corresponding to (a), respectively. (e) Results of quantitative analyses of S, Mg and Sr. One point corresponds to a step width of 2.70 µm.

Fig. 3.22 shows the electron microprobe mapping results and elemental line profile analysis of a cross section of *Anodonta cygnea*.

An area containing both, nacreous (N) and prismatic (P) layers is shown in Fig. 3.22a. The white arrow shows the quantitative line profile analysis which begins in the nacreous layer and ends in the prismatic layer. 90 points were measured with a width of 1.43 μm per step. The BSE image displays clearly the boundaries between the prisms and there are dark lines in the nacreous layer which are aligned perpendicular to the surface of the shell. Between the prisms and the nacreous layer, there occurs no obvious boundary, which corresponds the result in lateral section.

Concentrations of sulphur, magnesium, and strontium are shown in Figs. 3.22b, 3.22c and 3.22d using a brightness scale, respectively. Sulphur occurs in a higher concentration between the prisms and shows a homogeneous distribution in the nacreous layer. Similar to the lateral section in Fig. 3.21, magnesium and strontium occur in both prismatic and nacreous layers homogeneously distributed.

Results of elemental concentration in weight percent are presented in Fig. 3.22e for three elements. The corresponding BSE image shown along the white arrow in Fig. 3.22a was added above the quantitative results. The left red dashed line indicates the boundaries between the nacreous and prismatic layers. It is seen that there occurs no obvious change in the concentration of the three elements in both layers. The right dashed line (around point 86) indicates the boundary of two prisms. Here the concentration of sulphur (~0.1 wt. %) is higher than in other areas. In addition, magnesium has a lower concentration than strontium (~0.09 wt. %) all over the scanned line.

3.3 Chemical composition of samples

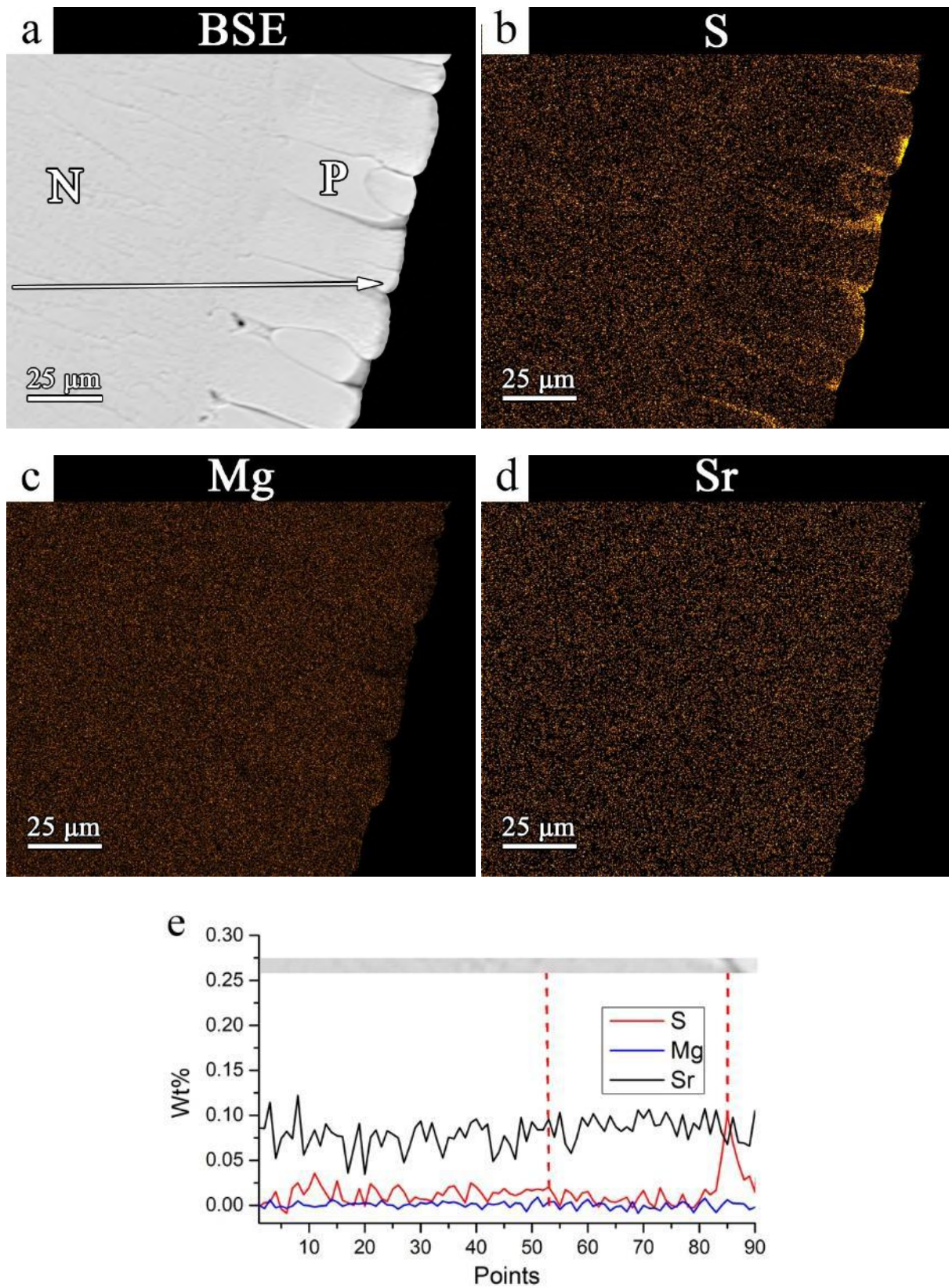


Fig. 3.22 Electron microprobe analyses results of a cross section of *Anodonta cygnea*. (a) BSE image including prismatic (P) and nacreous (N) layer. The white arrow indicates the trace of the quantitative line profile analysis. (b)- (d) Intensity maps of S, Mg and Sr corresponding to (a), respectively. (e) Results of quantitative analyses of S, Mg and Sr. One point corresponds to a step of 1.43 μm .

3.3.3 *Phorcus turbinatus*

Fig. 3.23 shows electron microprobe mapping results and the elemental line profile analysis of a lateral section of *Phorcus turbinatus*.

Fig. 3.23a is the BSE image of the mapped area of the studied lateral section including nacreous (N) and prismatic (P) layers. A quantitative line profile elemental analysis across two layers is shown as the white arrow in the BSE image. The profile starts in the nacreous layer and ends in the prismatic layer. 100 points were measured using a width of 3 μm per step. There is no sharp compositional gap visible between the two layers. However, different textures from the two layers can be observed.

Figs. 3.23b, 3.23c and 3.23d show the concentrations of sulphur, magnesium, and strontium, respectively. Unlike *Pinctada fucata* and *Anodonta cygnea*, sulphur does neither show a higher concentration between the prisms nor between the prismatic and nacreous layers. In addition, magnesium is distributed homogeneously. Strontium occurs in both, prismatic and nacreous layer but in nacreous layer, a slightly higher concentration can be assumed.

Fig. 3.23e shows the results of the element concentrations in weight percent for three elements. Above the three element lines, a corresponding BSE image plotted along the white arrow in Fig. 3.23a is shown. The dashed red line indicates the boundary between nacreous (left) and prismatic (right) layers. Combining the BSE image and the quantitative results, it is concluded that the concentration of sulphur has in general a higher concentration in the prismatic layer (0.05 wt. %) than in the nacreous layer (0.02 wt. %). Magnesium shows a low concentration in both layers. The overall concentration of strontium is higher than for the other two elements. Besides, strontium shows a higher content in the nacreous layer (0.18 wt. %) than in the prismatic layer (0.08 wt. %).

3.3 Chemical composition of samples

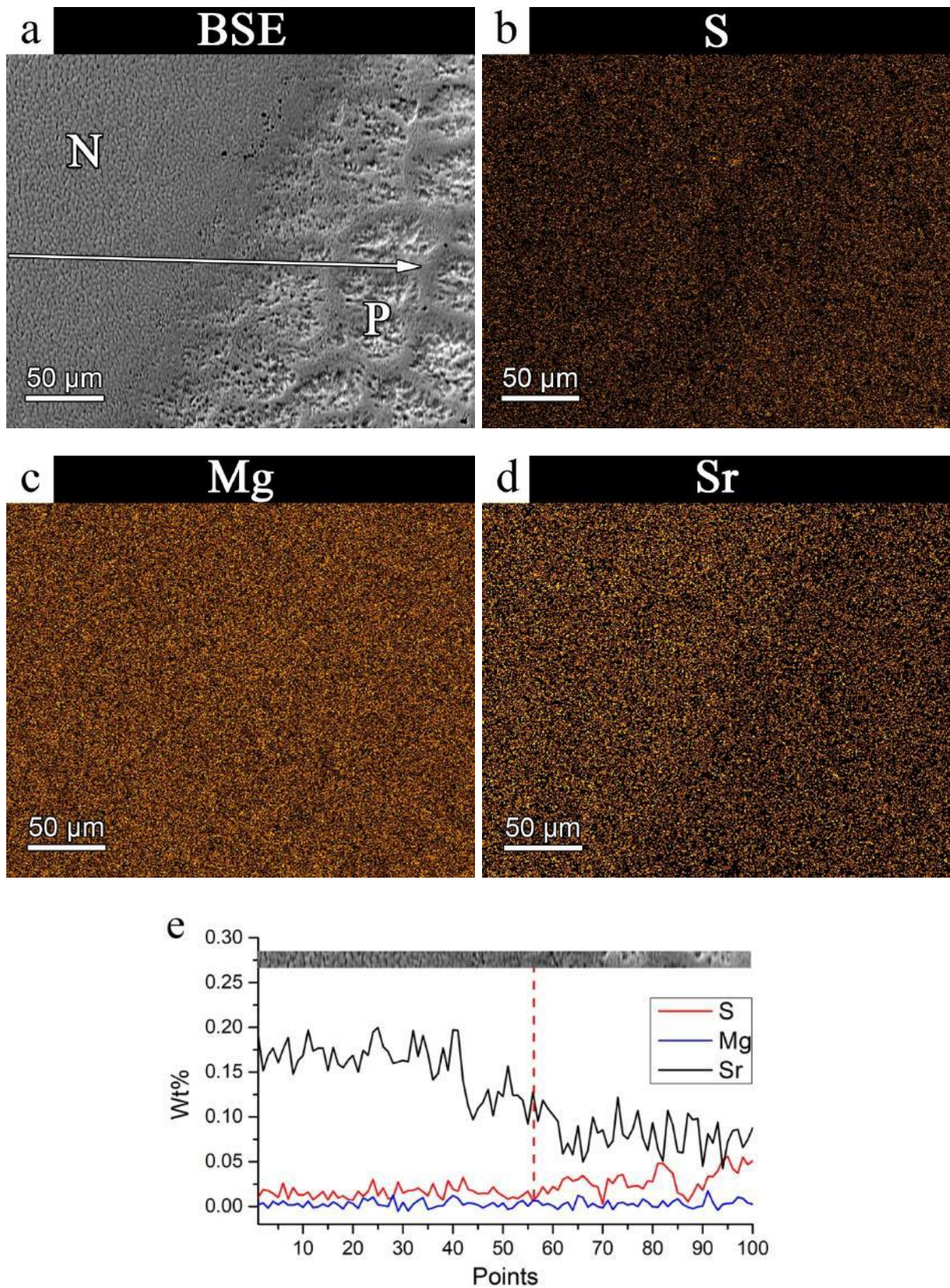


Fig. 3.23 Electron microprobe analyses results of a cross section of *Anodonta cygnea*. (a) BSE image including prismatic (P) and nacreous (N) layer. The white arrow indicates the quantitative elemental line profile analysis. (b)- (d) Intensity maps of S, Mg and Sr corresponding to (a), respectively. (e) Results of quantitative analyses of S, Mg and Sr. One point corresponds to a step of 3 µm.

Fig. 3.24 shows the electron microprobe mapping results and the elemental line profile analysis of a cross section of *Phorcus turbinatus*.

Fig. 3.24a provides the BSE image of the mapped area on a cross section including nacreous (N) and prismatic (P) layers. Similar to Fig. 3.23a, there occurs no obvious compositional gap between the two layers, but the contrast and colour gradient reflects the different textures in the two layers. The white arrow in the BSE image represents the trace of the quantitative line profile analysis. The profile starts in the prismatic layer and ends in the nacreous layer. 100 points in steps of 2.30 μm were measured.

Figs. 3.24b, 3.24c and 3.24d show concentrations of sulphur, magnesium, and strontium using the brightness scale, respectively. Similar to the results in lateral section and different from the other two species, it can be seen that sulphur does neither occur in denser concentration between the prisms nor between the prismatic and nacreous layers. However, sulphur has an overall higher content in the prisms than in nacre. Magnesium is distributed homogeneously in each layer but shows a slightly higher concentration in the prisms. Strontium occurs in both prismatic and nacreous layers homogeneously.

Fig. 3.24e shows the line analysis of the elements in weight percent. The corresponding BSE image along the white arrow in Fig. 3.24a is shown above. The dashed red line indicates the boundary position between the prismatic (left) and nacreous (right) layers. Similar to the result shown in Fig. 3.23e, sulphur has a higher concentration in the prism (0.11 wt. %) than in the nacre area (0.02 wt. %). In the Appendix VI, one can also observe that the colour of the prismatic layer is darker than the nacreous layer under the polarized optical microscope. This may indicate that the prismatic layer has higher content of organic matter. Magnesium shows a low concentration in both layers, but one can still see that the concentration in prisms (0.02 wt. %) is higher than in nacre areas. The overall concentration of strontium is higher compared with the other two elements and it shows a slightly higher content in nacreous layer (0.18 wt. %) than in the prismatic layer (0.13 wt. %).

3.3 Chemical composition of samples

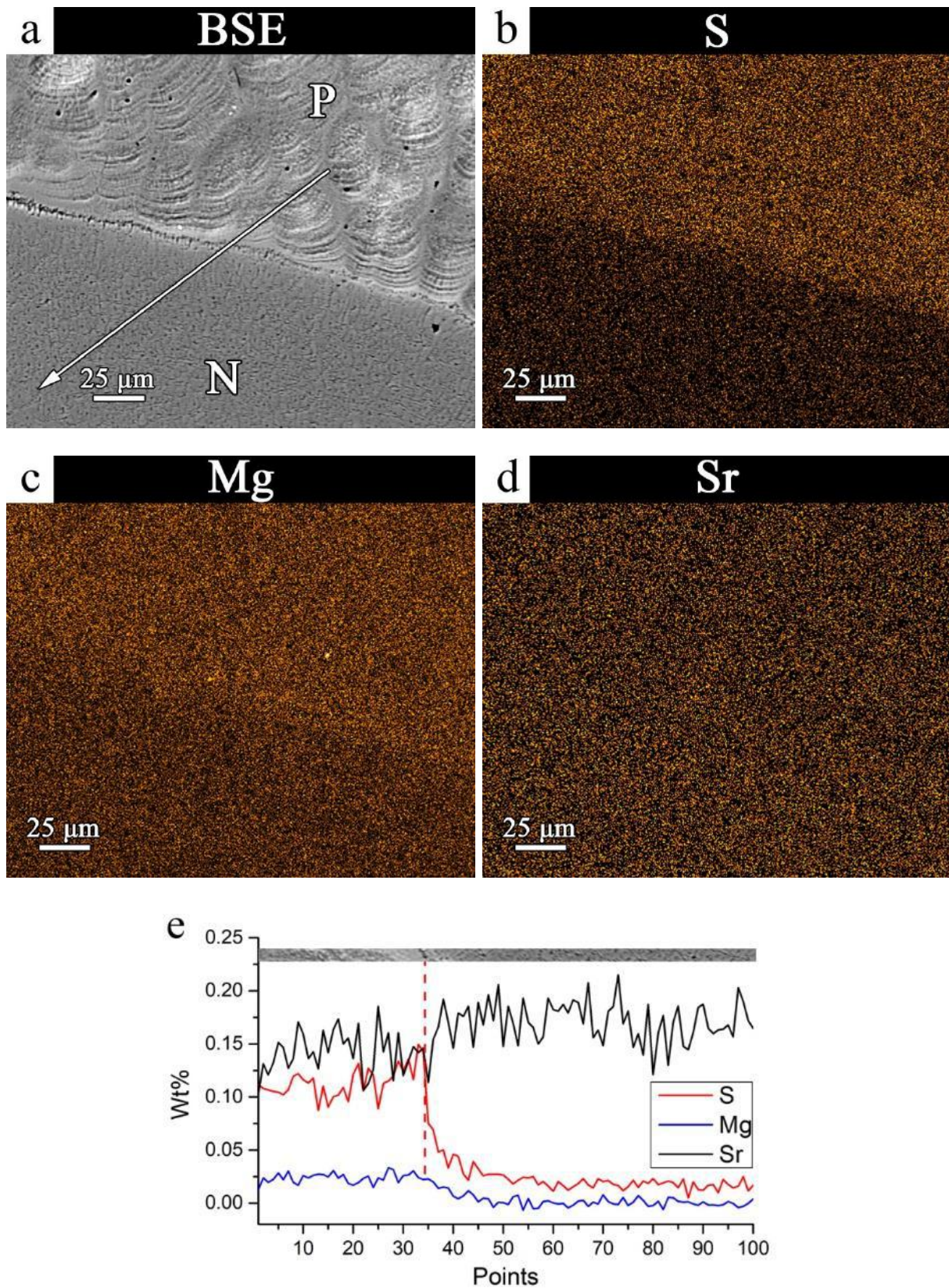


Fig. 3.24 Electron microprobe analyses data of a cross section of *Anodonta cygnea*. (a) BSE image including prismatic (P) and nacreous (N) layer. The white arrow indicates the trace of the quantitative line profile analysis. (b)- (d) Intensity maps of S, Mg and Sr corresponding to (a), respectively. (e) Results of quantitative analyses of S, Mg and Sr. One point corresponds to a step of 2.30 μm.

3.3 Chemical composition of samples

Table 3.1 shows a compilation of the quantitative results of the electron microprobe analyses. Sulphur has in general a low content in all three species, it has higher concentration in the prismatic layer of *Pinctada fucata* and *Phorcus turbinatus*. Magnesium occurs mostly in the calcitic prismatic layer of *Pinctada fucata*; Strontium was found only in *Anodonta cygnea* and *Phorcus turbinatus*, it occurs with higher content in the nacreous layer than in the prismatic layer of *Phorcus turbinatus*.

Table 3.1 Electron microprobe results

	<i>Pinctada fucata</i>				<i>Anodonta cygnea</i>				<i>Phorcus turbinatus</i>			
	Lateral section		Cross section		Lateral section		Cross section		Lateral section		Cross section	
	Prism	Nacre	Prism	Nacre	Prism	Nacre	Prism	Nacre	Prism	Nacre	Prism	Nacre
S	0.05*	0.02	0.05	0.02	0.02	0.02	0.02	0.02	0.03	0.02	0.11	0.02
Mg	1.1	**	0.55	\	\	\	\	\	\	\	0.02	\
Sr	\	\	\	\	0.07	0.07	0.09	0.09	0.08	0.18	0.13	0.18

* Results are given in weight percent.

** \ below the detecting limit.

4 Discussion

4.1 Nacreous layers

The nacreous layers of three species have in general a related microstructure but differ from each other in sizes, surface morphologies, crystal orientation, distributions of mesoscale twinning and the degrees of co-orientation of crystallographic axes.

Both SEM and EBSD results show that the nacreous layer is made of parallel lamellae and each lamella is composed of nacre tablets. This study confirmed that the nacreous layers of the three species have similar mesoscopic structure, which has been described in former researchers' work as 'brick-and-mortar' structure: where the polygonal tablets made of aragonite crystallites are the bricks and the organic matter corresponds to the mortar (Watabe, 1965; Addadi and Weiner, 1997).

From Figs. 3.1b, 3.3b and 3.5b, the diameters of nacre tablets from *Pinctada fucata*, *Anodonta cygnea* and *Phorcus turbinatus* can be determined to be 2-5 μm , 2-5 μm and 2-10 μm , respectively. From the SEM results of the cross sections in Figs. 3.2a, 3.4a and 3.6a, the thickness of nacre tablets from *Pinctada fucata*, *Anodonta cygnea* and *Phorcus turbinatus* occurs to be 0.5-0.7 μm , 1.3-1.5 μm and 1-1.6 μm , respectively. The average size of the nacre tablets from the gastropod species is the largest. The nacre tablets in *Anodonta cygnea* and *Phorcus turbinatus* are 2-3 times thicker than the nacre tablets of *Pinctada fucata*. From a previous study (Snow and Pring, 2005), it is known that the diffraction of light through the lamellae structure causes the angle-dependent iridescence of nacreous layers of shells and pearls, which is relevant for their economic value. The thickness and the regularity of each nacreous layer will determine the intensity and colour of the iridescence. For the human eye, visible colour occurs when the thickness is about 0.4-0.7 μm . Combined with the results of this work, we can explain the iridescence observed on the inner surface of the *Pinctada fucata* shell and why it is economically more important than the other two species.

Nevertheless, the three species possess different features on the surface of the nacreous layer. Fig. 3.1b and Appendix I.a show that the inner surface of *Pinctada fucata* is terrace made of nacre lamellae. Fig. 3.3b and Appendix I.b show that *Anodonta cygnea* has no significant texture pattern. New nacre tablets appear isolated upon older ones. Fig. 3.5b and Appendix I.c show that the surface of the nacreous layer in *Phorcus turbinatus* is composed of aragonite columns. Several former studies have discussed the formation and growth of nacreous layer.

An important theory is that new nacre tablets grow from old nacre tablets through mineral bridges across the organic sheets (or membranes) between the nacre lamellae (*Schäffer et al.*, 1997). As shown in Fig. 1.2b, organic matter exists between the lamellae (named interlamellar sheets) (*Nakahara*, 1991), as well as between the nacre tablets within the same lamella. AFM (*Schäffer et al.*, 1997) and ultrahigh-resolution SEM (*Lopez et al.*, 2014) have revealed that the interlamellar organic sheets are porous. The growth of new nacre tablets may occur as homoepitaxial crystallization through the pores (*Checa et al.*, 2011; *Griesshaber et al.*, 2013; *Shao et al.*, 2014). It has also been reported that the pores in the interlamellar sheets have different positions and sizes (*Cartwright and Checa*, 2007). The pores in interlamellar sheets of gastropods are larger than the ones in bivalves. Besides, the pores are located at the centre of a nacre tablet in gastropods, while the pores locate at the edge of a tablet in bivalves. Combing the results of this work and those of the former studies, the different surface morphologies may be due to the position and the size of the mineral bridges. Fig. 4.1 shows possible models of three different morphologies.

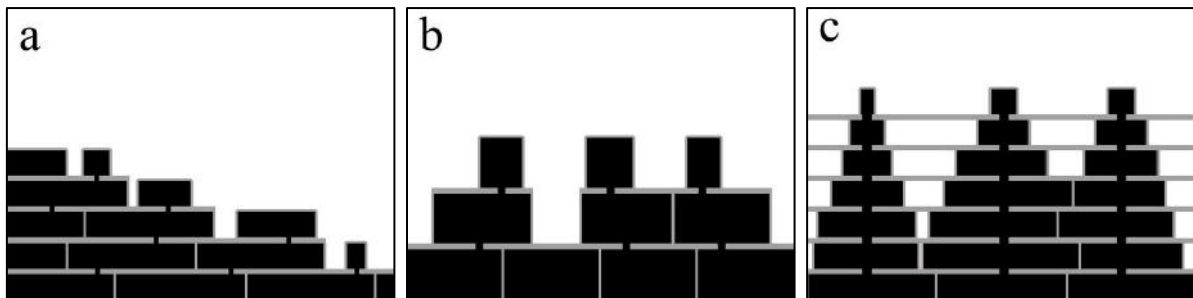


Fig. 4.1 Schematic illustrations of morphology types at the surface of nacreous layer (cross section view). (a) *Pinctada fucata* (b) *Anodonta cygnea* (c) *Phorcus turbinatus*. Black areas show nacre tablets and grey areas show organic matter. The sketch is based on results of this thesis and former studies (*Nudelman*, 2015).

The Band contrast maps of the lateral section of nacreous layers in Figs. 3.7a, 3.10a and 3.16a are indexed using aragonite lattice parameters. All three surfaces display terrace-like patterns which are divided into small tablets. The upper half of the BC maps is superimposed respectively by three grain boundary types with different misorientation angles of $63.8^\circ \pm 2^\circ$ (red), $52.4^\circ \pm 2^\circ$ (green) and $> 2^\circ$ (yellow). Red and green colours are widely distributed in the gastropod sample *Phorcus turbinatus*. From the insets in the BC maps, we see that all boundaries exist between the tablets, leading to the conclusion that the angle differences between crystallites within a tablet are smaller than 2° . These results also correspond well to previous studies of *Mytilus* species by *Griesshaber et al.* (*Griesshaber et al.*, 2013).

Although they resemble with each other in the BC maps, the orientation information map of Figs. 3.7b, 3.10b and 3.16b reveal that the three species have in fact different topological organization of the aragonite crystallites in their nacreous layer. In *Pinctada fucata* (Fig. 3.7b), the aragonite tablets shows a ‘patchy’ or a ‘lizard skin-like’ pattern, which is composed of various clusters of different particle orientations. *Anodonta cygnea* shows a homogeneous particle orientational background with a small amount of isolated deviations. Particle orientations in *Phorcus turbinatus* are evenly distributed corresponding to a variety of colours. Combining the results from pole figures in Fig. 3.7c, 3.10c and 3.16c, we confirm that the *c*-axis of the three species has basically one principle orientation, which is perpendicular to the measured surface (i.e. the shell surface). However, the *a*- or *b*-axis of aragonite crystallites in *Pinctada fucata* can be arranged in six groups, the colour clusters in the ‘lizard skin-like’ pattern display orientation domains. The *a*- or *b*-axis of aragonite crystallites in *Anodonta cygnea* is arranged in one direction but with large dispersion. The *a*- or *b*-axis in *Phorcus turbinatus* is however neither arranged in domains nor along one direction, but they are evenly distributed in all directions parallel to the measured surface.

From the distribution of the misorientation angles of three species shown in Figs. 3.7d, 3.10d and 3.16d, the misorientation around 63.8° in the gastropod sample of *Phorcus turbinatus* is the highest fraction among the three species and corresponds to the high distribution of red and green colours in the corresponding BC map. 63.8° is a typical angle between the same axes of twins in abiogenic aragonite. From previous studies (He *et al.*, 2014; He *et al.*, 2016), it is known that grain boundaries of 63.8° and 52.4° cannot be called classical twin boundaries, since the individuals of the ‘twins’ are not single crystals in biominerals. Each tablet is made of nanoparticles with considerable amount of organic impurities (named intracrystalline organic matrix) (Wang *et al.*, 2001; Rousseau *et al.*, 2005; Dalbeck *et al.*, 2006). We concluded in a former study that the nacreous layers observed also in this work present a typical mesocrystal type structure. Mesocrystals have been defined as highly oriented superstructures of nanocrystals (Cölfen and Mann, 2003; Cölfen and Antonietti, 2005). The ‘twinning’ mentioned here is in fact a mesotwinning. A mesotwin is related to a twin, like a mesocrystal to a crystal and it contains defects, since there is probably organic material in the ‘twin’ boundaries (Floquet and Vielzeuf, 2011). In our former study on *Pinctada fucata* (He *et al.*, 2016), we found that the mesotwin boundaries can extend well in large domains which contain several to dozens of nacre tablets. Massive mesotwin boundaries found in the gastropod *Phorcus*

turbinatus exist mostly between the nacre tablets and do not extend further. In other words, the domains in *Phorcus turbinatus* are considerably smaller and more discrete.

Among the three species, *Pinctada fucata* has the highest MUD values which means that the crystallographic *c*-axis of *Pinctada fucata* has the highest degree of co-orientation, *Phorcus turbinatus* was the second and *Anodonta cygnea* has the lowest co-orientation.

In the cross sections, more details about the co-orientation of axes in the nacreous layer are displayed in Figs. 3.9, 3.12 and 3.17. The orientation of crystallites, displayed by different colours in Fig. 3.9b (right part), 3.12b (right part) and 3.17, is separated into clusters. One cluster or stripe has been selected and framed in black outline in each of the three species for detailed investigation. The colours extend in both directions along and across the lamellae, which means that the crystal orientation domains occur in 3-dimensional disorder. The clusters in black frames form so-called ‘towergrains’ defined in previous studies (*Checa et al.*, 2009; *Checa et al.*, 2011; *Griesshaber et al.*, 2013). We observe that the towergrains in the gastropod sample *Phorcus turbinatus* extend mostly in one direction across the lamellae and include basically all nacre tablets. Some additional plots of the ‘towergrains’ can be seen in Appendix II, IV and V.

Pole figures in Figs. 3.9c, 3.12c and 3.17c show that the crystallographic *c*-axis of aragonite crystallites in the cross section of the nacreous layer also points along one general direction, which is along the extended axis of the prisms and perpendicular to the shell surface. The results correspond to the data of the lateral section. Combining the surface morphologies observed by SEM with the EBSD results, it can be assumed that the new tablets in the three species inherited crystal orientations of older nacre tablets like seeds when they grow. Inheriting the crystal orientation occurs in directions parallel as well as perpendicular to the shell surface in bivalves and mostly perpendicular to the shell surface in gastropods. Neighbouring columns with intersecting tablets shown by the red circles in Fig. 3.5b could indicate a mesotwin relationship. The MUD values show that the nacreous layer of *Pinctada fucata* has the largest co-orientation of the crystallites, which corresponds to results of the lateral section.

The large fraction of misorientation angles around 63.8° shown in Figs. 3.9d, 3.12d and 3.17d indicate that there also occurs intensive mesoscale twinning in cross sections. From the insets in BC maps of Figs. 3.9a, 3.12a and 3.17a, it is seen that the mesotwin boundaries exist both, between and across the nacre lamellae in all three species.

By growing calcium carbonate in different solutions with organic matrix extracted from the shells, previous studies have confirmed that the organic matrix seems to control the morphology and the crystallization of different calcium carbonate polymorphs (*Belcher et al.*, 1996; *Falini et al.*, 1996). However, whether they are the main cause of the crystallites co-orientation requires further work. From other studies, it is also known that triple twin structures of (110) are frequently formed in geological aragonite in order to mimic a higher symmetry and to reduce the system's energy. On the other hand, the twinning structure reduces the grain size and form more boundaries to prevent crack propagation and deformation (*Carter and Norton*, 2007; *He et al.*, 2016). From EBSD results in nacreous layer in this work, it is found that the aragonite mesotwinning is common and is leading to a random distribution between nacre tablets within one lamella or between adjacent lamellae. An energy-driven texture may be a disproof for a simple hypothesis, which considers only the organic matrices to conduct the co-orientation of crystallites (*Weiner and Hood*, 1975; *Reeves and Evans*, 1997).

Furthermore, in grain boundary theory, the boundaries between crystallites can usually be divided into two groups, the low-angle grain boundaries (LAGBs), which are accommodated by an array of edge and/or screw dislocations (*Lejcek*, 2010), and the high-angle grain boundaries (HAGBs). The transition angle between LAGBs and HAGBs lies between 13–15°, depending on materials (*Brandon*, 1966; *Glicksman and Vold*, 1972). Compared with high angle grain boundaries, the low-angle grain boundaries have fewer defects; and can also act as a barrier to prevent deformations (*Campbell*, 2008). In results this thesis, the misorientation angles between 2° -15° are a dominant group of grain boundaries and widely distributed between the nacre tablets. It may be considered that these low-angle grain boundaries have enhanced the mechanical properties of our biominerals in addition to the mesotwin boundaries.

4.2 Prismatic layers

The prismatic layers of three selected species have different chemical compositions, sizes, structures and crystal orientations.

The prismatic layers in the samples of *Anodonta cygnea* and *Phorcus turbinatus* are composed of aragonite, however the prismatic layer of *Pinctada fucata* is made of calcite. Contrary to the size differences of nacre, it was found that the diameter of prisms in *Anodonta cygnea* (2-5 μm) is 2-10 times smaller than the prisms of *Pinctada fucata* and *Phorcus turbinatus*. Besides, *Pinctada fucata* has the thickest prismatic layer and *Anodonta cygnea* has the thinnest one. The latter is 7-20 times thinner than the former one. From previous studies (Menzies *et al.*, 1992; Zajac, 2002; Southgate and Lucas, 2011), it is known that the three species live in different habitats. *Pinctada fucata* lives in shallow littoral zone in tropical region, which goes through a huge change of temperature, salinity and desiccation with the tides. *Anodonta cygnea* lives in wide ponds or slow rivers in temperate region with high concentration of dissolved oxygen. *Phorcus turbinatus* is found principally in the lower midlittoral zone of the Mediterranean Sea. The differences of the prism sizes may reflect how the animals adapt to their habitats.

From SEM results in Figs. 3.2b, 3.4b and 3.6b as well as the BC maps in Figs. 3.8a, 3.11a and 3.18a, we can see that calcitic prisms in sample of *Pinctada fucata* are composed of very fine particles, the aragonitic prisms in *Anodonta cygnea* are mainly composed of granules ($\sim 1 \mu\text{m}$) and in *Phorcus turbinatus* they are mainly composed of pinnate fibrous crystallites. This fibrous structure can also be observed in a thin section of the *Phorcus turbinatus* sample (see Appendix VI).

Calcitic prisms from many species of the subclass Pteriomorphia, including *Mytilus californianus*, *Atrina rigida*, *Pinctada margaritifera* have been studied previously (Checa *et al.*, 2013; Olson *et al.*, 2013). EBSD results have shown that the *Mytilus californianus* and *Atrina rigida* consist of single-crystalline prisms and *Pinctada margaritifera* has multi-domain prisms. In the first two species, each prism has a crystallographic angle spread less than 0.3° , however we consider the word ‘single-crystalline’ here is questionable, since other work has shown that there occurs intraprismatic organic matter in the prisms of *Mytilus* and *Atrina* (Nudelman *et al.*, 2007; Checa *et al.*, 2014). In the third species, it occurs that the crystallographic orientation of a calcitic prism can split into different domains during growth and the crystallographic orientation of each domain shows also longitudinal and transversal gradients. In other studies

(Dalbeck *et al.*, 2006; Harper and Checa, 2017), it was shown that the *c*-axis of calcitic prisms is aligned along one direction parallel to the long axis of the prisms (i.e. perpendicular to the shell surface).

In this study, it is seen that different calcitic prisms of our sample *Pinctada fucata* do not align in one orientation, and may even differ strongly from each other. A large percentage of prisms (red prisms in Fig. 3.8b and blue prism in 3.9b) have the *c*-axis parallel to their long axes (i.e. perpendicular to the shell surface). The *c*-axis of the remaining prisms is however oriented perpendicular or approximately perpendicular to their morphologically extended axes (see the poles distributed at the primitive circle of {001} in Fig. 3.8c). Furthermore, the pole figure {001} in Fig. 3.9e shows three distinct clusters of poles from the three prisms shown in Fig. 3.9b. The three prisms are oriented approximately perpendicular to each other. Misorientation angles between neighbouring prisms can be as large as 90° and in between occurs no visible topological transition.

It has been suggested in other studies that the regular sequence of functional groups in the organic matter can be a template to initialize and guide the crystallization of aragonite and calcite to the finally defined orientation (Weiner and Hood, 1975; Feng *et al.*, 2000). Since all prisms (Fig. 3.8 and 3.9) seem to crystallize simultaneously, the result of this work may question a simple template theory.

The orientation gradient within one calcitic prism has also been studied in this work. The homogeneous colour of each prism in Figs. 3.8b and 3.9b (left part) show that the calcite crystallites within one prism are highly co-oriented and their crystallographic orientation matches well. The BC maps shown in Figs. 3.8a and 3.9a, indicate however deviations by dark lines in the prisms, which is assumed to be the location of intraprismatic organic matter. In order to know the relationship of intraprismatic organic matter and the crystallographic orientation, six misorientation profiles selected from Figs. 3.8b and 3.9b with their corresponding pole figures are shown in Fig. 4.2. The selected profiles are labelled from 1-6 following the arrows in Fig. 3.8b and 3.9b.

Fig. 4.2a indicates for example that the *c*-axis of the crystallites in this prism is parallel to the measured surface (i.e. the shell surface) and one of the three *a*-axes is perpendicular to the measured surface. The misorientation profile reveals that the overall point-to-point misorientation is below 2° but point-to-origin misorientation has a gradient, which can reach 28°. The result shows that the *c*-axis of calcite is turning gradually around one *a*-axis.

Fig. 4.2b and 4.2c are chosen from a prism, which has been divided internally by intraprismatic organic matter into smaller units. Fig. 4.2b is located within one unit and Fig. 4.2c goes over several units. The former one shows a similar gradient as Fig. 4.2a but with the c -axis perpendicular to the measured surface. Pole figures in Fig. 4.2b shows the rotation of the a - and c -axis. Fig. 4.2c reveals that the misorientation angle between different units is discontinuous and can be as large as 26° . Fig. 4.2b and 4.2c show that intraprismatic organic matter within one prism could act as a separation of the local crystallographic orientation.

In Fig. 4.2d, the direction of the c -axis is approximately perpendicular to the c -axis of Fig. 4.2a and 4.2b. The pole figure shows the change of the a -axis. Fig. 4.2e and 4.2f indicate that there exists an orientation gradient both, parallel and perpendicular to the long axis of the prism in the cross section. The orientation gradients found here coincide with the findings from previous study on *Pinctada margaritifera* (Checa *et al.*, 2013) and hence, we define the smaller units here as domains within the prisms.

Unlike the calcitic prisms under investigation, most aragonitic prisms lack sufficient microstructural research. The crystallographic orientation of aragonite prisms in cross sections of two Anodonta species has been studied using EBSD (Freer *et al.*, 2009). The authors could show that a single prism is composed of nanogranules, which have the c -axis perpendicular to the shell surface. They proposed that the a - and b -axis have different orientations but did not provide further details. The microstructure of aragonitic prisms in cross sections of several species from the bivalves has also been described in a former study (Checa and Rodríguez-Navarro, 2001). In the species *Lamprotula sp.*, each prism is composed of elongated monocrystalline aragonite fibres, which appear in a feather-like arrangement. X-ray texture diffractometry has shown that the c -axis of the aragonite crystallites points perpendicular to the shell surface and the b -axis is parallel to the growth direction of the shell.

In this work, the prisms of *Anodonta cygnea* and *Phorcus turbinatus* have entirely different textures compared with *Pinctada fucata*. From the pole figures on $\{001\}$ in Figs. 3.11c, 3.12e and 3.18c, it is confirmed that the c -axis of aragonite crystallites in both shells are co-oriented perpendicular to the shell surface with a certain dispersion. Secondly, Figs. 3.11b, 3.12b and

3.18b show abundant colours due to particle orientations, which means that the a - or b -axis of aragonite crystallites does not have uniform orientation, they are arranged in domains. Thirdly, Figs. 3.11d, 3.12f and 3.18d show that misorientations angles focus around 52.4° and 63.8° , which are the typical misorientation angles between aragonite mesotwins. From the

4.2 Prismatic layers

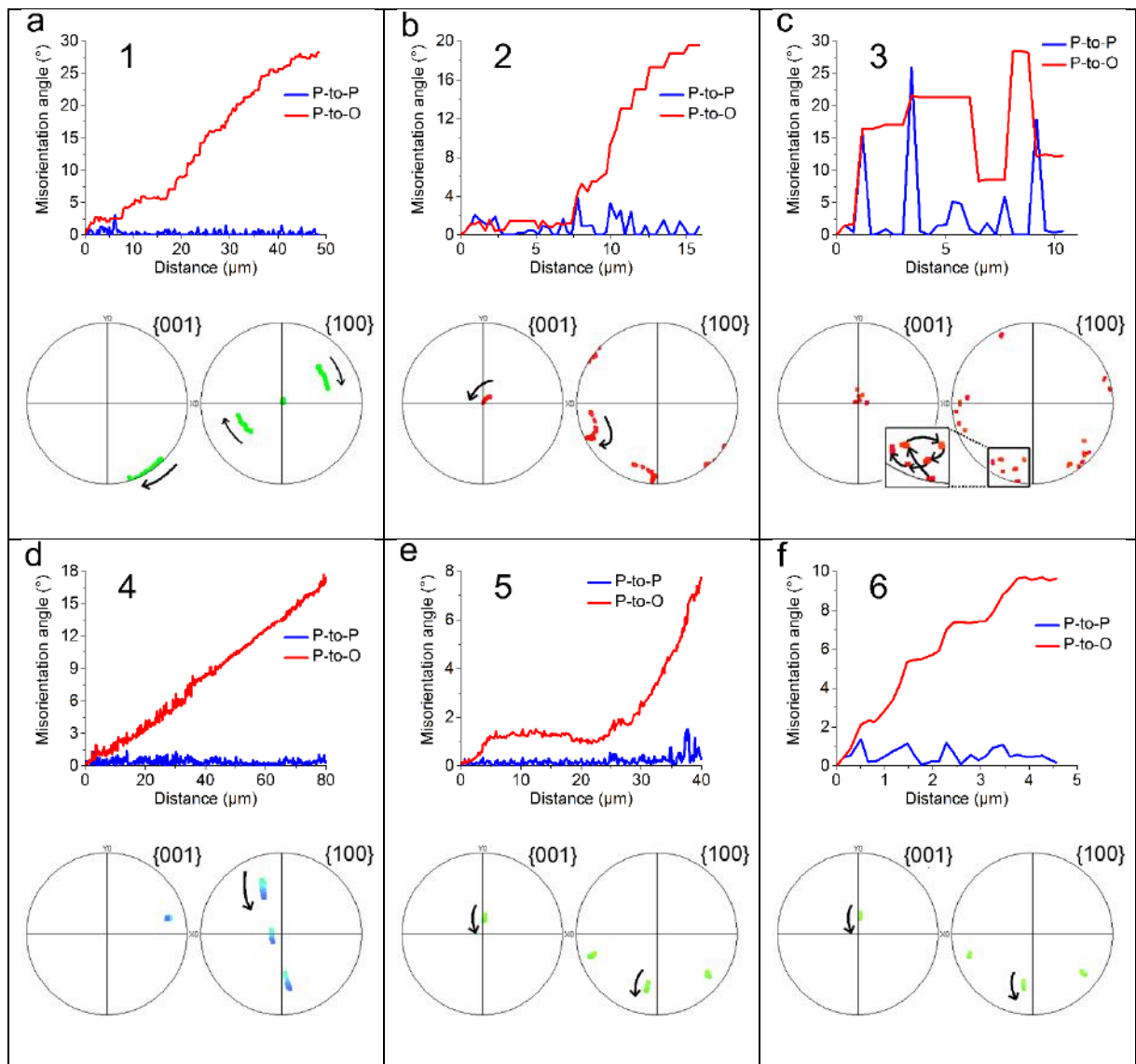


Fig. 4.2 Misorientation profiles from 1-6 with corresponding pole figures of {001} and {100}. Red profiles, point-to-origin misorientations; black profiles, point-to-point misorientations. The arrows indicate changing direction of the poles along the trace of the line profiles.

selected prism in each of the shells in Figs. 3.11a and 3.18a, it is also can be seen that there are considerable numbers of mesoscale aragonite twinning boundaries in the aragonitic prisms. This result is different from studies by the scientists mentioned above. Furthermore, Freer et al. (Freer et al., 2009) described that the orientation of prisms changes alternatively in other Anodonta species. According to Figs. 3.11b and 3.18b, such alternating orientation cannot be confirmed. Finally, the electron microprobe results in Figs. 3.19b, 3.20b, 3.21b and 3.22b show that there is a higher concentration of organic matter around the prisms in bivalves *Pinctada*

fucata and *Anodonta cygnea*, however we did not find such high concentration between the prisms in the gastropod sample of *Phorcus turbinatus*

Based on previous studies and the present results, a more accurate definition of the prismatic layer from three species can be given: *Pinctada fucata* has pseudo-single-crystalline calcitic prisms with considerable orientation divergence; *Anodonta cygnea* has poly-crystalline aragonitic prisms with twinned domains on the mesoscale, the twinned domains are arranged in a granular structure with size of ca. 1 μm ; *Phorcus turbinatus* also has poly-crystalline aragonitic prisms with mesoscale twinning, but the twinned domains are arranged in a pinnate fibrous texture. Fig. 4.3 shows the schematic illustrations of morphology types of prismatic layer.

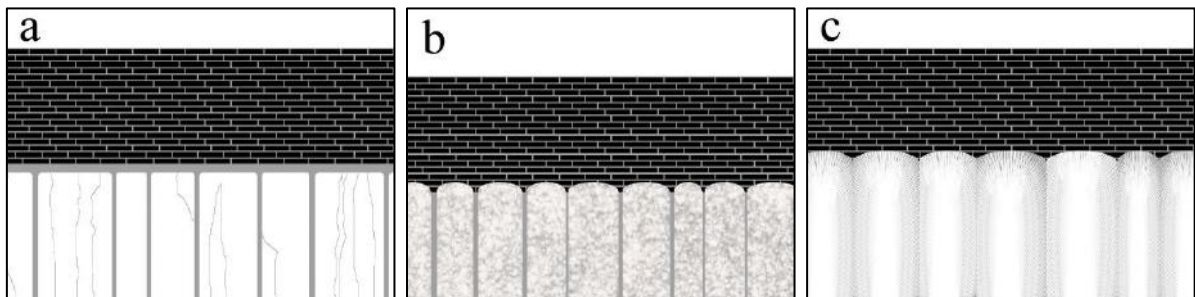


Fig. 4.3 Schematic illustrations of morphology types of prismatic layer (cross section view). (a) *Pinctada fucata* (b) *Anodonta cygnea* (c) *Phorcus turbinatus*. Black areas show the aragonite lamellae, grey areas show organic matter and white areas show the prisms.

4.3 From prisms to nacre

The shells from the three selected species have different prisms and accordingly have different transition areas between nacreous and prismatic layers. The differences of the transition between the two layers is seen in the chemical components and interface topography.

In *Pinctada fucata*, the compositional difference of the magnesium content between the prisms and nacre may due to the structural difference between calcite and aragonite. In former studies, it is proved that magnesium is easily incorporated into the crystal structure of calcite instead of aragonite in sea water since they have the same structure, and magnesium keeps calcite thermodynamically stable in sea water (Bernier, 1975). Moreover, Figs. 3.19b and 3.20b show that there is a higher sulphur content between the calcite and aragonite layer. Since sulphur occurs only in the organic matter, it is obvious that the calcitic prisms and aragonitic nacre are separated by a layer of organic matter, which also corresponds to the SEM images (Figs. 3.1a and 3.1c). Fig. 3.1c shows that an organic layer extends from the organic envelopes (i.e. interprismatic organic matter) between the prisms. The coverage of this organic material gets larger closer to the nacre material. Besides, Fig. 3.9b shows that the transformation of the crystal orientation from prisms to nacre appears a sharp boundary. Since only one of the three prisms in Fig. 3.9b has identical orientation of the crystallographic *c*-axis with the crystallites in nacre, it seems that the crystallographic orientation in nacre is hardly inherited from the calcitic prisms.

The electron microprobe results of *Anodonta cygnea* shown in Figs. 3.21b and 3.22b indicate that no or little organic layer occurs between nacre and the prisms because higher concentration of sulphur is seen only between the prisms. It can also be assumed from SEM images that the crystallization of nacre tablets was initialized at the rim of the convex top of the prisms directly (Fig. 3.3a and 3.3c). The top of the prisms changed their form of granules to fibrous crystallites (see SEM image of Fig. 3.4b and BC map of Fig. 3.12a). In addition, Fig. 3.12b shows the boundary between two layers and we find that parts of the nacre have identical crystallographic orientations as the fibres in prisms.

The electron microprobe analyses of *Phorcus turbinatus* shown in Fig. 3.23b and 3.24b do neither display a high concentration of sulphur between the prismatic and nacreous layers, nor between the prisms. From SEM images, we also did not find evidence for organic membranes between the two layers or between the prisms. From SEM images (Fig. 3.6), we can see that the shape of the prisms are less condensed as the prisms in the former two species. Electron

microprobe results shows that there is a much higher concentration of sulphur in the prismatic layer. Combined with an image from a thin section under the optical microscope (see Appendix II), it is concluded that there is more organic matter distributed in the prismatic layer. However, how the organic material is distributed around the fibrous crystallites in detail requires further studies.

The possible growth process of the shells has previously been studied and discussed for the freshwater bivalve *Amblema plicata* (family Unionidae, subclass Palaeoheterodonta) (*Petit et al.*, 1980). The periostracum is composed of three layers: outer, middle and inner layers; in this process, prisms are formed in the middle layer; then on the surface of the inner periostracum, which is located between nacre and middle periostracum layer, carbonate becomes mineralized as nacre. Later, in another model it was suggested that the periostracum has only two layers, and both layers cover the outside of the shell (*Checa*, 2000). Since we did not observe any traces of middle or inner periostracum between prismatic and nacreous layers in *Anodonta cygnea* and *Phorcus turbinatus*, the findings of this work may account for the model from the work of Checa. Additionally, the organic layer between the prisms and nacre in *Pinctada fucata* supplements the growth models of shells in different subclasses. As biological hard tissues are functionalized and environment adapted materials, the differences in calcium carbonate phases as well as in their crystallographic orientation may possibly reflect habitat specific requirements.

5 Conclusions

Main conclusions about the morphological and crystallographic features in the shell layers of *Pinctada fucata*, *Anodonta cygnea* and *Phorcus turbinatus* are as follows:

- (1) The investigated samples of three species have different surface morphologies of nacreous layer. The nacreous layers of three species are all composed of aragonite tablets and the size of the aragonite tablets varies from species to species. The crystallographic *c*-axis of aragonite crystallites is co-oriented in one direction. The *a*- or *b*-axis of aragonite crystallites is arranged in a domain structure in *Pinctada fucata* and *Phorcus turbinatus*, and co-oriented in *Anodonta cygnea*. Cross sections of all three investigated species clearly show experimental evidence that the particles with similar crystallographic orientation grow through several organic boundaries forming larger clusters. The three species show all mesoscale twinning in the nacreous layer in directions perpendicular and parallel to the shell surface, and the mesotwins have different forms in the three species. *Pinctada fucata* has the highest degree of co-orientation of aragonite crystallites.
- (2) The prismatic layers of samples from the three species have different size and different microstructures; the prisms of *Pinctada fucata* are composed of calcite, while the other two shells are made of aragonite; strontium occurs only in the latter two species; sulphur has a higher concentration in the prisms of *Pinctada fucata* and *Phorcus turbinatus*; only the calcitic prisms possess magnesium ions and appear in a pseudo-single-crystalline structure: the crystallites in one prism are oriented in the same orientation with a certain degree of divergence; the crystallographic *c*-axis is either perpendicular or parallel to the long axis of the prism; neighbouring calcitic prisms can have a large misorientation angle and there is no gradient of misorientation angles in between. The aragonitic prisms show a granular structure in *Anodonta cygnea* and a fibrous structure in *Phorcus turbinatus*. Both aragonite prisms possess heavy mesoscale twinning. The *c*-axis of the crystallites in aragonitic prisms is co-oriented along the same orientation, which is along the morphological extended axes of the prisms; the *a*- and *b*-axes of the crystallites are arranged in domains in aragonitic prisms, which are separated by mesoscale twin boundaries.
- (3) Between the prismatic and the nacreous layer of the samples of *Pinctada fucata* there exists an organic layer, which extends from the interprismatic organic matter, and the co-orientation of the *c*-axis in nacre seems not to be inherited from prisms; Nacre of *Anodonta*

cygnea and *Phorcus turbinatus* grows directly on top of the prisms and EBSD results show that the orientation of the nacre could be inherited from the prisms.

- (4) The relative intensities of different Raman modes have been calculated from different polarization directions and ratios. From mapping experiments, it can be confirmed that Raman spectroscopy is a useful tool to recognise the crystal orientation and local variations in biominerals, and the distribution of organic matter. Combined with rotational measurements on a reference single-crystal aragonite, one can determine the crystallographic orientation of the crystallites in the nacreous and prismatic layers.

Bibliography

- Addadi L., Weiner S. Biomineralization: A pavement of pearl. *Nature*, 1997, **389**(6654): 912-915.
- Addadi L., Raz S., Weiner S. Taking advantage of disorder: amorphous calcium carbonate and its roles in biomineralization. *Advanced Materials*, 2003, **15**(12): 959-970.
- Aizenberg J., Tkachenko A., Weiner S., Addadi L., Hendler G. Calcitic microlenses as part of the photoreceptor system in brittle stars. *Nature*, 2001, **412**(6849): 819-822.
- Band Y. B., Avishai Y. *Quantum mechanics with applications to nanotechnology and information science*. Academic Press, 2013.
- Bandel K. Shell structure of the Gastropoda excluding Archaeogastropoda. *Skeletal biomineralization: patterns, processes and evolutionary trends*, 1990, 117-134.
- Bandel K. Higher classification and pattern of evolution of the Gastropoda: a synthesis of biological and paleontological data. *Courier Forschungsinstitut Senckenberg*, 1997, **201**: 57-81.
- Belcher A. M., Wu X. H., Christensen R. J., Hansma P. K., Stucky G. D., Morse D. E. Control of crystal phase switching and orientation by soluble mollusc-shell proteins. *Nature*, 1996, **381**(6577): 56-58.
- Berland S., Ma Y., Marie A., Andrieu J., Bedouet L., Feng Q. Proteomic and profile analysis of the proteins laced with aragonite and vaterite in the freshwater mussel *Hyriopsis cumingii* shell biominerals. *Protein and peptide letters*, 2013, **20**(10): 1170-1180.
- Berner R. A. The role of magnesium in the crystal growth of calcite and aragonite from seawater. *Geochimica et Cosmochimica Acta*, 1975, **39**(4): 489-504.
- Bertini I. *Biological inorganic chemistry: structure and reactivity*. University Science Books, 2007.
- Bismayer U., Shi J., Klocke A., Gierlotka S., Palosz B. F. From Dental Enamel to Synthetic Hydroxyapatite-Metal Composites. *Key Engineering Materials*, 2005, 561-564.
- Boss K. J. *Critical estimate of the number of Recent Mollusca*. Department of Mollusks, Museum of Comparative Zoology, Harvard University, 1971.
- Bouchet P., Rocroi J., Frýda J., Hausdorf B., Ponder W., Valdés Á., Warén A. Classification and nomenclator of gastropod families. *Malacologia*, 2005, **47**(1-2), 1-368.
- Bouchet P., Rocroi J., Hausdorf B., Kaim A., Kano Y., Nützel A., Parkhaev P., Schrödl M., Strong E. E. Revised classification, nomenclator and typification of gastropod and monoplacophoran families. *Malacologia*, 2017, **61**(1-2): 1-526.
- Boynton W. V., Ming D. W., Kounaves S. P., Young S., Arvidson R. E., Hecht M. H., Hoffman

- J., Niles P. B., Hamara D. K., Quinn R. C. Evidence for calcium carbonate at the Mars Phoenix landing site. *Science*, 2009, **325**(5936): 61-64.
- Bragg W. L. The structure of aragonite. *Proceedings of the Royal Society of London. Series A, Containing Papers of a Mathematical and Physical Character*, 1924, **105**(729): 16-39.
- Brandon D. G. The structure of high-angle grain boundaries. *Acta metallurgica*, 1966, **14**(11): 1479-1484.
- Bruno M., Massaro F. R., Rubbo M., Prencipe M., Aquilano D. (10.4), (01.8), (01.2), and (00.1) Twin Laws of Calcite (CaCO₃): Equilibrium Geometry of the Twin Boundary Interfaces and Twinning Energy. *Crystal Growth & Design*, 2010, **10**(7): 3102-3109.
- Campanella L., Conti M. E., Cubadda F., Sucapane C. Trace metals in seagrass, algae and molluscs from an uncontaminated area in the Mediterranean. *Environmental Pollution*, 2001, **111**(1): 117-126.
- Campbell F. C. *Elements of metallurgy and engineering alloys*. ASM International, 2008.
- Carter C. B., Norton M. G. *Ceramic materials: science and engineering*. Springer Science & Business Media, 2007.
- Carteret C., De La Pierre M., Dossot M., Pascale F., Erba A., Dovesi R. The vibrational spectrum of CaCO₃ aragonite: A combined experimental and quantum-mechanical investigation. *The Journal of chemical physics*, 2013, **138**(1): 14201.
- Cartwright J. H., Checa A. G. The dynamics of nacre self-assembly. *Journal of the Royal Society Interface*, 2007, **4**(14): 491-504.
- Chapman A. D. *Numbers of living species in Australia and the world*. Australian Biological Resources Study, 2009.
- Chase R. B. *Behavior & its neural control in gastropod molluscs*. Oxford University Press on Demand, 2002.
- Checa A. A new model for periostracum and shell formation in Unionidae (Bivalvia, Mollusca). *Tissue and Cell*, 2000, **32**(5): 405-416.
- Checa A. G., Rodríguez-Navarro A. Geometrical and crystallographic constraints determine the self-organization of shell microstructures in Unionidae (Bivalvia: Mollusca). *Proceedings of the Royal Society of London B: Biological Sciences*, 2001, **268**(1468): 771-778.
- Checa A. G., Esteban-Delgado F. J., Rodríguez-Navarro A. B. Crystallographic structure of the foliated calcite of bivalves. *Journal of structural biology*, 2007, **157**(2): 393-402.
- Checa A. G., Cartwright J. H., Willinger M. The key role of the surface membrane in why gastropod nacre grows in towers. *Proceedings of the National Academy of Sciences*, 2009, **106**(1): 38-43.
- Checa A. G., Cartwright J. H., Willinger M. Mineral bridges in nacre. *Journal of structural*

- biology*, 2011, **176**(3): 330-339.
- Checa A. G., Bonarski J. T., Willinger M. G., Faryna M., Berent K., Kania B., González-Segura A., Pina C. M., Pospiech J., Morawiec A. Crystallographic orientation inhomogeneity and crystal splitting in biogenic calcite. *Journal of the Royal Society Interface*, 2013, **10**(86): 20130425.
- Checa A. G., Pina C. M., Osuna-Mascaró A. J., Rodríguez-Navarro A. B., Harper E. M. Crystalline organization of the fibrous prismatic calcitic layer of the Mediterranean mussel *Mytilus galloprovincialis*. *European Journal of Mineralogy*, 2014, **26**(4): 495-505.
- Cölfen H., Mann S. Higher-order organization by mesoscale self-assembly and transformation of hybrid nanostructures. *Angewandte Chemie International Edition*, 2003, **42**(21): 2350-2365.
- Cölfen H., Antonietti M. Mesocrystals: Inorganic superstructures made by highly parallel crystallization and controlled alignment. 2005.
- Colthup N. *Introduction to infrared and Raman spectroscopy*. Elsevier, 2012.
- Conti M. E., Cecchetti G. A biomonitoring study: trace metals in algae and molluscs from Tyrrhenian coastal areas. *Environmental Research*, 2003, **93**(1): 99-112.
- Crane N. J., Popescu V., Morris M. D., Steenhuis P., Ignelzi M. A. Raman spectroscopic evidence for octacalcium phosphate and other transient mineral species deposited during intramembranous mineralization. *Bone*, 2006, **39**(3): 434-442.
- Crenshaw M. A. The soluble matrix from *Mercenaria mercenaria* shell. *Biomineralization*, 1972, **6**: 6-11.
- Cusack M., England J., Dalbeck P., Tudhope A. W., Fallick A. E., Allison N. Electron backscatter diffraction (EBSD) as a tool for detection of coral diagenesis. *Coral Reefs*, 2008, **27**: 905-911.
- Dalbeck P., England J., Cusack M., FALLICK A. E. Crystallography and chemistry of the calcium carbonate polymorph switch in *M. edulis* shells. *European journal of mineralogy*, 2006, **18**(5): 601-609.
- Daudon M., Bazin D., André G., Jungers P., Cousson A., Chevallier P., Véron E., Matzen G. Examination of whewellite kidney stones by scanning electron microscopy and powder neutron diffraction techniques. *Journal of Applied Crystallography*, 2009, **42**(1): 109-115.
- De La Pierre M., Carteret C., Maschio L., André E., Orlando R., Dovesi R. The Raman spectrum of CaCO₃ polymorphs calcite and aragonite: A combined experimental and computational study. *The Journal of chemical physics*, 2014, **140**(16): 164509.
- De Leeuw N. H., Parker S. C. Surface structure and morphology of calcium carbonate polymorphs calcite, aragonite, and vaterite: an atomistic approach. *The Journal of Physical Chemistry B*, 1998, **102**(16): 2914-2922.

- DeVol R. T., Metzler R. A., Kabalah-Amitai L., Pokroy B., Politi Y., Gal A., Addadi L., Weiner S., Fernandez-Martinez A., Demichelis R. Oxygen spectroscopy and polarization-dependent imaging contrast (PIC)-mapping of calcium carbonate minerals and biominerals. *The Journal of Physical Chemistry B*, 2014, **118**(28): 8449-8457.
- Driessens F. C., Verbeeck R. K. *Biominerals*. CRC Press, 1990.
- Falini G., Albeck S., Weiner S., Addadi L. Control of aragonite or calcite polymorphism by mollusk shell macromolecules. *Science*, 1996, **271**: 67-69.
- Fdez-Gubieda M. L., Muela A., Alonso J., García-Prieto A., Olivi L., Fernández-Pacheco R., Barandiarán J. M. Magnetite biomineralization in *Magnetospirillum gryphiswaldense*: time-resolved magnetic and structural studies. *ACS nano*, 2013, **7**(4): 3297-3305.
- Feng Q. L., Li H. B., Pu G., Zhang D. M., Cui F. Z., Li H. D., Kim T. N. Crystallographic alignment of calcite prisms in the oblique prismatic layer of *Mytilus edulis* shell. *Journal of materials science*, 2000, **35**(13): 3337-3340.
- Floquet N., Vielzeuf D. Mesoscale twinning and crystallographic registers in biominerals. *American Mineralogist*, 2011, **96**(8-9): 1228-1237.
- Freer A., Greenwood D., Chung P., Pannell C. L., Cusack M. Aragonite prism–nacre interface in freshwater mussels *Anodonta anatina* (Linnaeus, 1758) and *Anodonta cygnea* (L. 1758). *Crystal Growth & Design*, 2009, **10**(1): 344-347.
- Gauldie R. W., Sharma S. K., Volk E. Micro-Raman spectral study of vaterite and aragonite otoliths of the coho salmon, *Oncorhynchus kisutch*. *Comparative Biochemistry and Physiology Part A: Physiology*, 1997, **118**(3): 753-757.
- Gierlinger N., Sapei L., Paris O. Insights into the chemical composition of *Equisetum hyemale* by high resolution Raman imaging. *Planta*, 2008, **227**(5): 969-980.
- Glicksman M. E., Vold C. L. Heterophase dislocations—an approach towards interpreting high temperature grain boundary behavior. *Surface science*, 1972, **31**: 50-67.
- Gorr M. C. An atomic force microscope (AFM) study of the calcite cleavage plane: Image averaging in Fourier space. *American Mineralogist*, 1992, **77**: 904-910.
- Gosling E. *Bivalve molluscs: biology, ecology and culture*. John Wiley & Sons, 2008.
- Griesshaber E., Schmahl W. W., Ubhi H. S., Huber J., Nindiyasari F., Maier B., Ziegler A. Homoepitaxial meso- and microscale crystal co-orientation and organic matrix network structure in *Mytilus edulis* nacre and calcite. *Acta Biomaterialia*, 2013, **9**(12): 9492-9502.
- Halliday D., Resnick R., Walker J. *Fundamentals of Physics Extended, 10th Edition*. Wiley, 2013.
- Harper E. M., Checa A. Physiological versus Biological Control in Bivalve Calcite Prisms: Comparison of Euheterodonts and Pteriomorphs. *The Biological Bulletin*, 2017, **232**(1): 19-29.

- Haszprunar G. The Heterobranchia—a new concept of the phylogeny of the higher Gastropoda. *Journal of Zoological Systematics and Evolutionary Research*, 1985, **23**(1): 15-37.
- Haszprunar G. *Mollusca (Molluscs)*. John Wiley & Sons, Ltd, 2001.
- He J., Zhao S., Yang M. Preferred Orientation of Aragonite in Nacre of *Pinctada Martensii* Shell Determined by Electron Backscatter Diffraction. *Chinese Journal of Inorganic Chemistry*, 2014, **30**(10): 2252-2257.
- He J., Zhao S., Wei Z., Bismayer U. Mesoscale twinning in shells of *Pinctada martensii*. *Zeitschrift für Kristallographie-Crystalline Materials*, 2016, **231**(11): 673-680.
- Hedegaard C. Shell structures of the recent Vetigastropoda. *Journal of Molluscan Studies*, 1997, **63**(3): 369-377.
- Heywood B. R., Mann S. Molecular construction of oriented inorganic materials: controlled nucleation of calcite and aragonite under compressed Langmuir monolayers. *Chemistry of Materials*, 1994, **6**(3): 311-318.
- Huang Y., Hsiao P., Chai H. Hydroxyapatite extracted from fish scale: Effects on MG63 osteoblast-like cells. *Ceramics International*, 2011, **37**(6): 1825-1831.
- Ji H. M., Li X. W. Microstructural characteristic and its relation to mechanical properties of *Clinocardium californiense* shell. *Journal of the American Ceramic Society*, 2014, **97**(12): 3991-3998.
- Kirov G. K., Vesselinov I., Cherneva Z. Conditions of formation of calcite crystals of tabular and acute rhombohedral habits. *Crystal Research and Technology*, 1972, **7**(5): 497-509.
- Lejcek P. *Grain boundary segregation in metals*. Springer Science & Business Media, 2010.
- Lewis I. R., Edwards H. *Handbook of Raman spectroscopy: from the research laboratory to the process line*. CRC Press, 2001.
- Li X. W., Ji H. M., Yang W., Zhang G. P., Chen D. L. Mechanical Properties of Crossed-Lamellar Structures in Biological Shells: A Review. *Journal of the Mechanical Behavior of Biomedical Materials*, 2017.
- Liang Y., Zhao Q., Li X., Zhang Z., Ren L. Study of the microstructure and mechanical properties of white clam shell. *Micron*, 2016, **87**: 10-17.
- Liao H., Mutvei H., Sjöström M., Hammarström L., Li J. Tissue responses to natural aragonite (Margaritifera shell) implants in vivo. *Biomaterials*, 2000, **21**(5): 457-468.
- Lippmann F. *The Polymorphism Calcite-Aragonite*. Springer, 1973.
- Litvin A. L., Valiyaveetil S., Kaplan D. L., Mann S. Template-directed synthesis of aragonite under supramolecular hydrogen-bonded Langmuir monolayers. *Advanced Materials*, 1997, **9**(2): 124-127.

- Lopez M. I., Martinez P. E. M., Meyers M. A. Organic interlamellar layers, mesolayers and mineral nanobridges: contribution to strength in abalone (*Haliotis rufescens*) nacre. *Acta biomaterialia*, 2014, **10**(5): 2056-2064.
- Lowenstam H. A., Abbott D. P. Vaterite: a mineralization product of the hard tissues of a marine organism (Asciidiacea). *Science*, 1975, **188**(4186): 363-365.
- Lowenstam H. A. Spicular morphology and mineralogy in some Pyuridae (Asciidiacea). *Bulletin of Marine Science*, 1989, **45**(2): 243-252.
- Lu R. *Crystallographic Orientation of Biogenic Aragonite in Pearls*. Gemological Institute of America, 2009.
- Mann S., Perry C. C., Webb J., Luke B., Williams R. Structure, morphology, composition and organization of biogenic minerals in limpet teeth. *Proceedings of the Royal Society of London B: Biological Sciences*, 1986, **227**(1247): 179-190.
- Mann S. *Biomineralization: principles and concepts in bioinorganic materials chemistry*. Oxford University Press on Demand, 2001.
- Marxen J. C., Hammer M., Gehrke T., Becker W. Carbohydrates of the organic shell matrix and the shell-forming tissue of the snail *Biomphalaria glabrata* (Say). *The Biological Bulletin*, 1998, **194**(2): 231-240.
- Menzies R., Cohen Y., Lavie B., Nevo E. Niche adaptation in two marine gastropods, *Monodonta turbiformis* and *M. turbinata*. *Italian Journal of Zoology*, 1992, **59**(3): 297-302.
- Monje P. V., Baran E. J. Characterization of calcium oxalates generated as biominerals in cacti. *Plant Physiology*, 2002, **128**(2): 707-713.
- Morton B. The evolutionary history of the Bivalvia. *Origin and evolutionary radiation of the Mollusca*, 1996, 337-359.
- Munisso M. C., Zhu W., Pezzotti G. Raman tensor analysis of sapphire single crystal and its application to define crystallographic orientation in polycrystalline alumina. *Physica status solidi (b)*, 2009, **246**(8): 1893-1900.
- Nakahara H. *Nacre formation in bivalve and gastropod molluscs*. Springer, 1991.
- Nehrke G., Nouet J. Confocal Raman microscope mapping as a tool to describe different mineral and organic phases at high spatial resolution within marine biogenic carbonates: case study on *Nerita undata* (Gastropoda, Neritopsina). *Biogeosciences*, 2011, **8**(12): 3761-3769.
- Nehrke G., Poigner H., Wilhelms Dick D., Brey T., Abele D. Coexistence of three calcium carbonate polymorphs in the shell of the Antarctic clam *Laternula elliptica*. *Geochemistry, Geophysics, Geosystems*, 2012, **13**(5).
- Newell N. D. *Classification of the Bivalvia*. American Museum of Natural History, 1965.

- Nowell M. M., Witt R. A., True B. EBSD sample preparation: Techniques, tips, and tricks. *Microscopy and Microanalysis*, 2005, **11**(S02): 504.
- Nudelman F., Chen H. H., Goldberg H. A., Weiner S., Addadi L. Spiers Memorial Lecture Lessons from biomineralization: comparing the growth strategies of mollusc shell prismatic and nacreous layers in *Atrina rigida*. *Faraday discussions*, 2007, **136**: 9-25.
- Nudelman F. Nacre biomineralization: a review on the mechanisms of crystal nucleation. Elsevier, 2015. 2-10.
- Oldenbourg R. Polarized light field microscopy: an analytical method using a microlens array to simultaneously capture both conoscopic and orthoscopic views of birefringent objects. *Journal of microscopy*, 2008, **231**(3): 419-432.
- Olson I. C., Metzler R. A., Tamura N., Kunz M., Killian C. E., Gilbert P. U. Crystal lattice tilting in prismatic calcite. *Journal of structural biology*, 2013, **183**(2): 180-190.
- Ozaki N., Kogure T. Crystal orientation of calcite components in coccoliths: EBSD analyses of submicron crystals. *Geochimica et Cosmochimica Acta*, 2003, **67**: 368.
- Park N. S., Kim M. W., Langford S. C., Dickinson J. T. Atomic layer wear of single-crystal calcite in aqueous solution using scanning force microscopy. *Journal of Applied Physics*, 1996, **80**(5): 2680-2686.
- Patterson J. D., Bailey B. C. *Solid-state physics: introduction to the theory*. Springer Science & Business Media, 2007.
- Pérez-Huerta A., Dauphin Y., Cuif J. P., Cusack M. High resolution electron backscatter diffraction (EBSD) data from calcite biominerals in recent gastropod shells. *Micron*, 2011, **42**(3): 246-251.
- Perić J., Vučak M., Krstulović R., Brečević L., Kralj D. Phase transformation of calcium carbonate polymorphs. *Thermochimica Acta*, 1996, **277**: 175-186.
- Perrin C., Prestimonaco L., Servelle G., Tilhac R., Maury M., Cabrol P. Aragonite–calcite speleothems: identifying original and diagenetic features. *Journal of Sedimentary Research*, 2014, **84**(4): 245-269.
- Petit H., Davis W. L., Jones R. G., Hagler H. K. Morphological studies on the calcification process in the fresh-water mussel *Amblema*. *Tissue and Cell*, 1980, **12**(1): 13-28.
- Pilati T., Demartin F., Gramaccioli C. M. Lattice-dynamical estimation of atomic displacement parameters in carbonates: calcite and aragonite CaCO_3 , dolomite $\text{CaMg}(\text{CO}_3)_2$ and magnesite MgCO_3 . *Acta Crystallographica Section B: Structural Science*, 1998, **54**(5): 515-523.
- Pokroy B., Kabalah-Amitai L., Polishchuk I., DeVol R. T., Blonsky A. Z., Sun C., Marcus M. A., Scholl A., Gilbert P. U. Narrowly distributed crystal orientation in biomineral vaterite. *Chemistry of Materials*, 2015, **27**(19): 6516-6523.

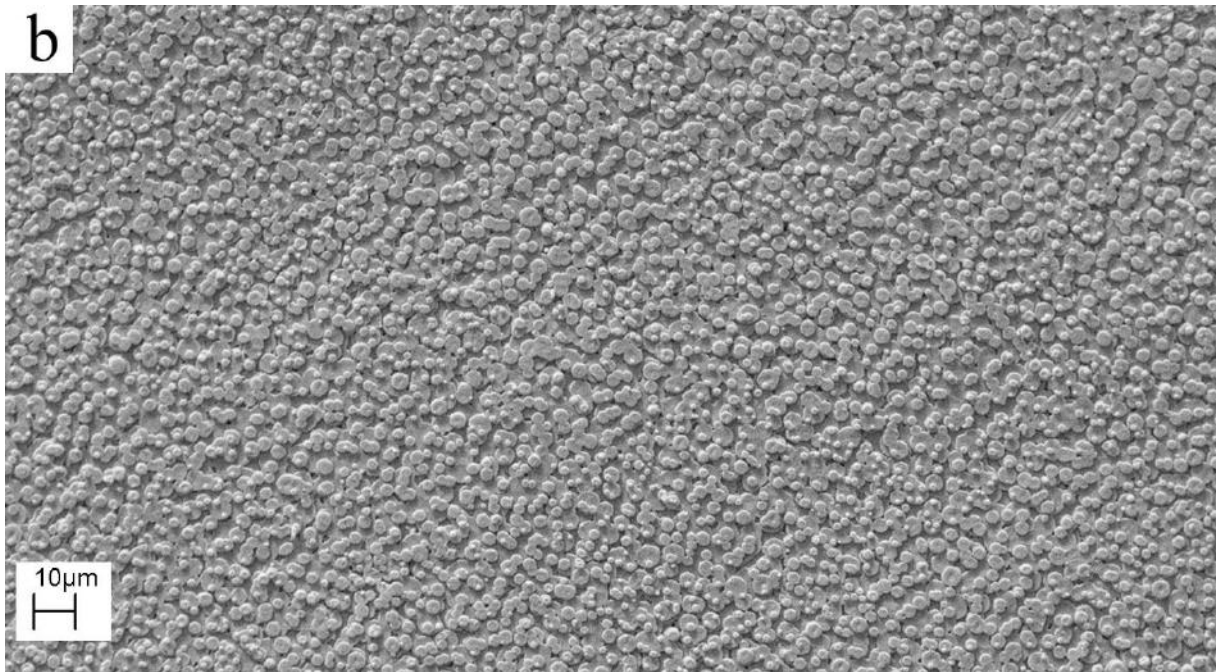
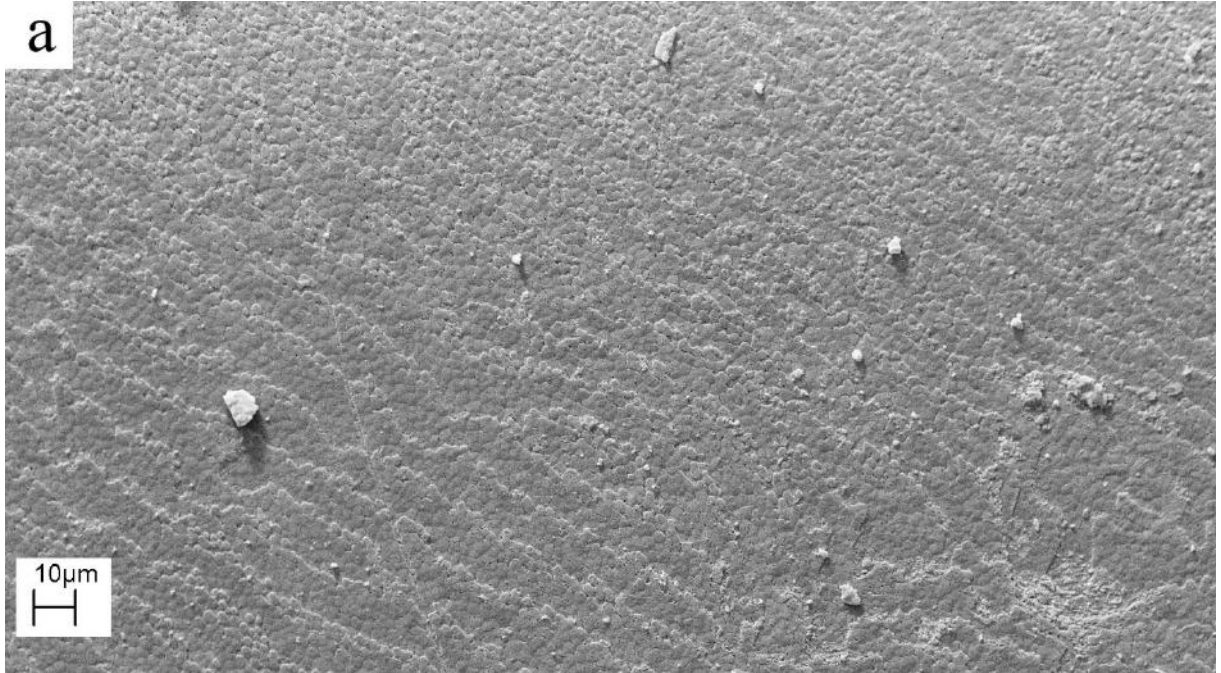
- Ponder W., Hutchings P., Chapman R. *Overview of the conservation of Australian marine invertebrates*. Report for Environment Australia, Australian Museum, Sydney, 2002.
- Ponder W. F., Colgan D. J., Healy J., Nützel A., Simone L., Strong E. E. Caenogastropoda. In: *Molluscan Phyloheny*. University of California Press, Los Angeles. 2008, 331-383.
- Prothero D. R. *Bringing fossils to life: An introduction to paleobiology*. Columbia University Press, New York. 2013.
- Raman C. V., Krishnan K. S. A new type of secondary radiation. *Nature*, 1928, **121**(3048): 501.
- Raz S., Testeniere O., Hecker A., Weiner S., Luquet G. Stable amorphous calcium carbonate is the main component of the calcium storage structures of the crustacean *Orchestia cavimana*. *The Biological Bulletin*, 2002, **203**(3): 269-274.
- Reed S. J. B. *Electron microprobe analysis and scanning electron microscopy in geology*. Cambridge University Press, Cambridge. 2005.
- Reeves N. J., Evans J. S. Polypeptide Interactions at Ice and Biomineral Interfaces Are Defined by Secondary Structure-Dependent Chain Orientations. *The Journal of Physical Chemistry B*, 1997, **101**(34): 6665-6669.
- Rousseau M., Lopez E., Stempflé P., Brendlé M., Franke L., Guette A., Naslain R., Bourrat X. Multiscale structure of sheet nacre. *Biomaterials*, 2005, **26**(31): 6254-6262.
- Schaeffer M. Crystal Structures of Aragonite, Strontianite, and Witherite. *The American Mineralogist*, 1971, **56**: 758-767,
- Schäffer T. E., Ionescu-Zanetti C., Proksch R., Fritz M., Walters D. A., Almqvist N., Zaremba C. M., Belcher A. M., Smith B. L., Stucky G. D. Does abalone nacre form by heteroepitaxial nucleation or by growth through mineral bridges? *Chemistry of Materials*, 1997, **9**(8): 1731-1740.
- Schmahl W. W., Griesshaber E., Neuser R., Lenze A., Reinhart J., Brand U. The microstructure of the fibrous layer of terebratulide brachiopod shell calcite. *European journal of mineralogy*, 2004, **16**(4): 693-697.
- Schwartz A. J., Kumar M., Adams B. L., Field D. P. *Electron Backscatter Diffraction in Materials Science*. Springer US, 2010.
- Señorale-Pose M., Chalar C., Dauphin Y., Massard P., Pradel P., Marín M. Monohydrocalcite in calcareous corpuscles of *Mesocostoides corti*. *Experimental parasitology*, 2008, **118**(1): 54-58.
- Shao Y., Zhao H., Feng X. Optimal characteristic nanosizes of mineral bridges in mollusk nacre. *RSC Advances*, 2014, **4**(61): 32451-32456.
- Sikes C. S., Wheeler A. P. Regulators of biomineralization. *Chemtech*, 1988, **18**(10): 620-626.
- Smith B. L., Schäffer T. E., Viani M., Thompson J. B., Frederick N. A., Kindt J., Belcher A.,

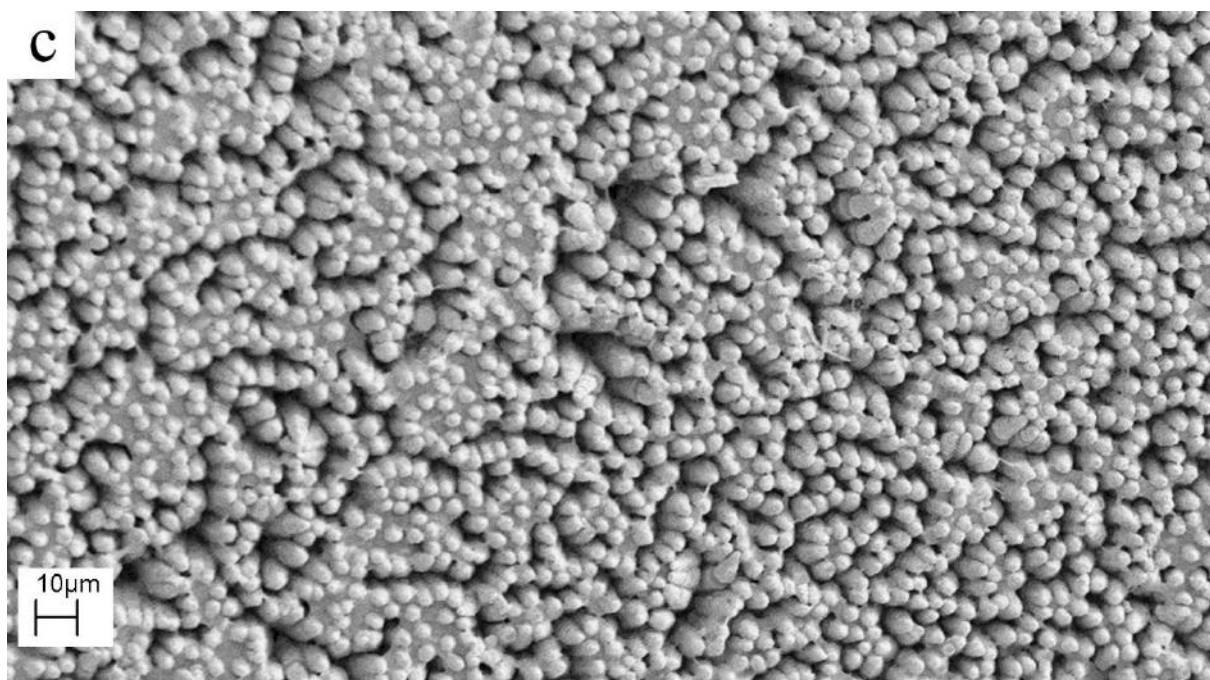
- Stucky G. D., Morse D. E., Hansma P. K. Molecular mechanistic origin of the toughness of natural adhesives, fibers and composites. *Nature*, 1999, **399**(6738): 761-763.
- Smith E., Dent G. *Modern Raman spectroscopy: a practical approach*. John Wiley & Sons, 2013.
- Snow M. R., Pring A. The mineralogical microstructure of shells: Part 2. The iridescence colors of abalone shells. *American Mineralogist*, 2005, **90**(11-12): 1705.
- Southgate P., Lucas J. *The pearl oyster*. Elsevier, 2011.
- Spero H. J., Bijma J., Lea D. W., Bemis B. E. Effect of seawater carbonate concentration on foraminiferal carbon and oxygen isotopes. *Nature*, 1997, **390**(6659): 497-500.
- Stanley S. M. *Relation of shell form to life habits of the Bivalvia (Mollusca)*. Geological Society of America, 1970.
- Stokes D. *Principles and practice of variable pressure: environmental scanning electron microscopy (VP-ESEM)*. John Wiley & Sons, 2008.
- Strong E. E., Gargominy O., Ponder W. F., Bouchet P. Global diversity of gastropods (Gastropoda; Mollusca) in freshwater. *Hydrobiologia*, 2008, **595**(1): 149-166.
- Suzuki S., Uozumi S. Organic components of prismatic layers in molluscan shells. *Journal of the Faculty of Science, Hokkaido University. Series 4, Geology and mineralogy*, 1981, **20**(1): 7-20.
- Theodor M., Schmiedl G., Mackensen A. Stable isotope composition of deep-sea benthic foraminifera under contrasting trophic conditions in the western Mediterranean Sea. *Marine Micropaleontology*, 2016, **124**: 16-28.
- Unvros J., Sharma S., Mackenzie F. Characterization of some biogenic carbonates with Raman spectroscopy. *American Mineralogist*, 1991, **76**: 641-646.
- Urmos J., Mackenzie F. T., Sharma S. K. Characterization of biominerals with Raman spectroscopy. *Transactions American Geophysical Union*, 1986, **67**: 1721.
- Vermeij G. J., Signor P. W. The geographic, taxonomic and temporal distribution of determinate growth in marine gastropods. *Biological Journal of the Linnean Society*, 1992, **47**(3): 233-247.
- Vielzeuf D., Floquet N., Chatain D., Bonneté F., Ferry D., Garrabou J., Stolper E. M. Multilevel modular mesocrystalline organization in red coral. *American Mineralogist*, 2010, **95**(2-3): 242-248.
- Wang R. Z., Suo Z., Evans A. G., Yao N., Aksay I. A. Deformation mechanisms in nacre. *Journal of Materials Research*, 2001, **16**(09): 2485-2493.
- Watabe N. Studies on shell formation: XI. Crystal--matrix relationships in the inner layers of mollusk shells. *Journal of ultrastructure research*, 1965, **12**(3): 351-370.

- Weaver J. C., Wang Q., Miserez A., Tantuccio A., Stromberg R., Bozhilov K. N., Maxwell P., Nay R., Heier S. T., DiMasi E. Analysis of an ultra hard magnetic biomineral in chiton radular teeth. *Materials Today*, 2010, **13**(1): 42-52.
- Weiner S., Hood L. Soluble protein of the organic matrix of mollusk shells: a potential template for shell formation. *Science*, 1975, **190**(4218): 987-989.
- Weiner S., Traub W., Parker S. B. Macromolecules in mollusc shells and their functions in biomineralization [and Discussion]. *Philosophical Transactions of the Royal Society of London. B, Biological Sciences*, 1984, **304**(1121): 425-434.
- Weiner S., Addadi L. Design strategies in mineralized biological materials. *Journal of Materials Chemistry*, 1997, **7**(5): 689-702.
- Wisniewski W., Rüssel C. An experimental viewpoint on the information depth of EBSD. *Scanning*, 2016, **38**(2): 164-171.
- Yang Y., Liu Y. L., Zhang L. Y., Zhu K., Ma S. Y., Siu G. G., Xu Z. K., Luo H. S. Polarized Raman mapping study of the microheterogeneity in $0.67\text{PbMg}_{1/3}\text{Nb}_{2/3}\text{O}_3-0.33\text{PbTiO}_3$ single crystal. *Journal of Raman Spectroscopy*, 2010, **41**(12): 1735-1742.
- Yonge C. M. Mantle margins with a revision of siphonal types in the Bivalvia. *Journal of Molluscan Studies*, 1982, **48**(1): 102-103.
- Zaefferer S. A critical review of orientation microscopy in SEM and TEM. *Crystal Research and Technology*, 2011, **46**(6): 607-628.
- Zajac K. Habitat preferences of Swan Mussel *Anodonta cygnea* (Linnaeus 1758) (Bivalvia, Unionidae) in relation to structure and successional stage of floodplain waterbodies. *Ecology-International Journal for Ecological Problems of the Biosphere*, 2002.
- Zhang Y., Gong Y. Application of polarized Raman spectroscopy in the research on molecule conformation. *Spectroscopy and Spectral Analysis*, 2013, **33**(7): 1810-1815.
- Zhou W., Wang Z. L. *Scanning microscopy for nanotechnology: techniques and applications*. Springer science & business media, 2007.

Appendix

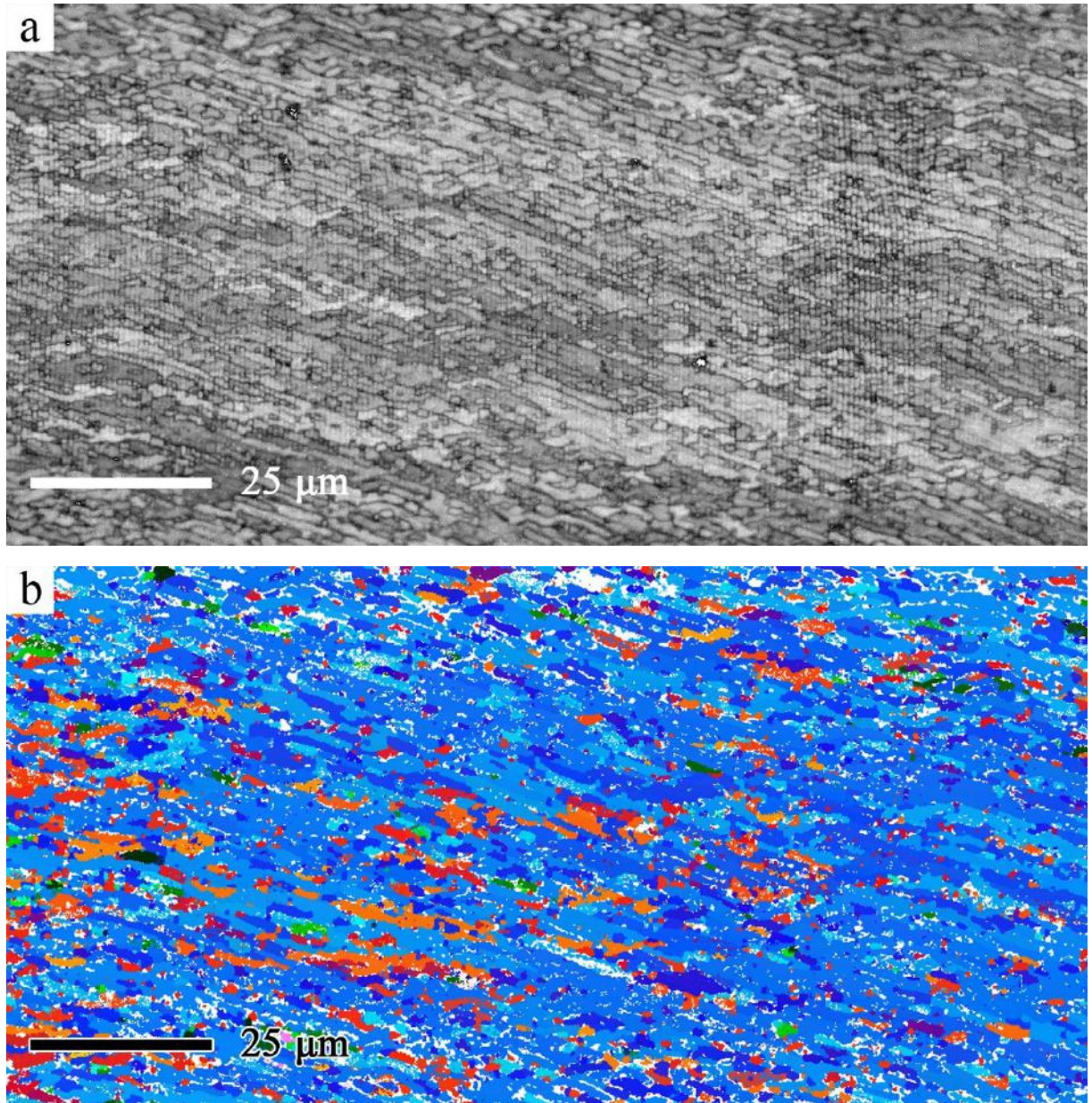
Appendix I





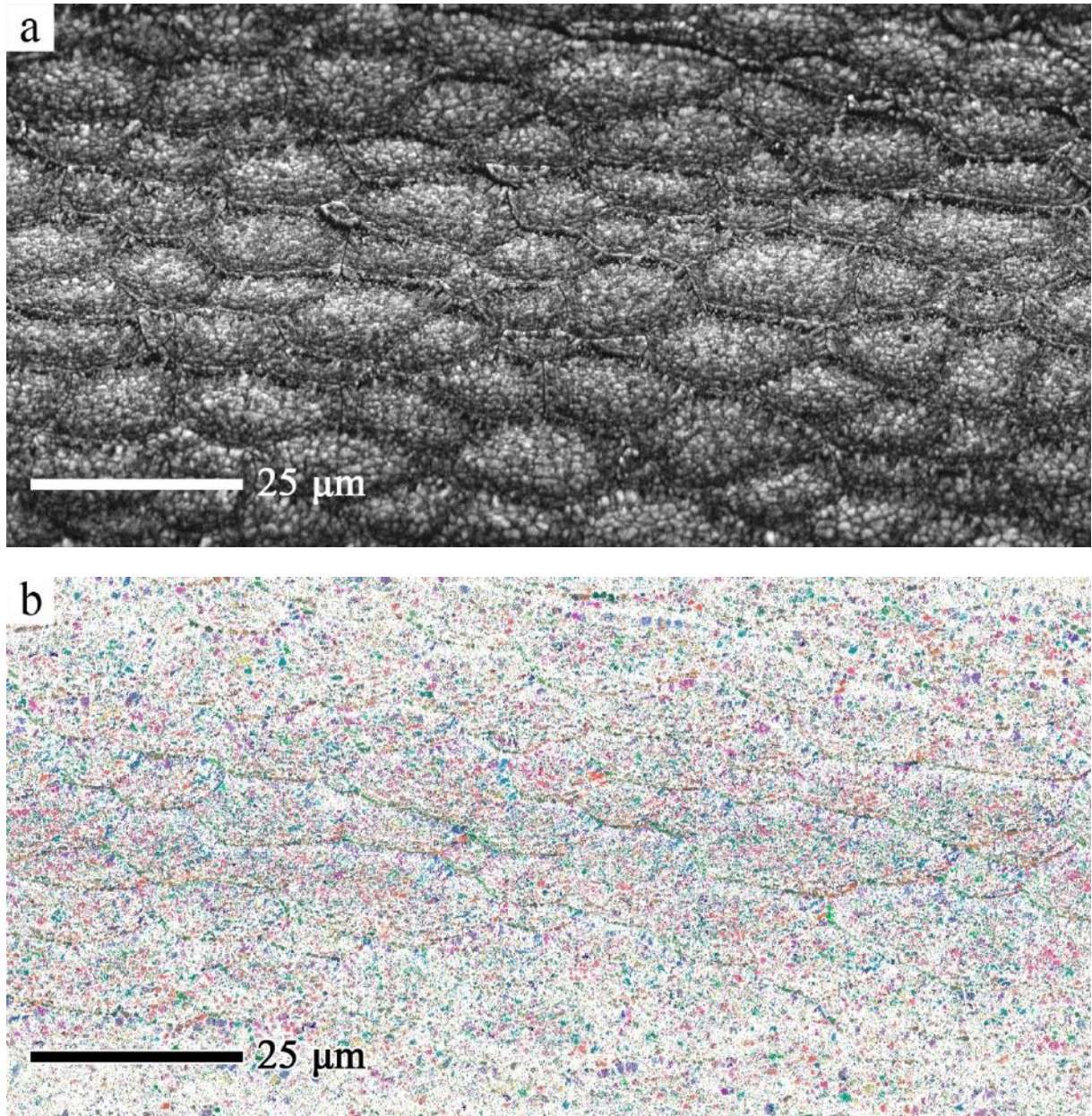
Appendix I Overview of the inner surface of nacreous layer. (a) *Pinctada fucata*. (b) *Anodonta cygnea*. (c) *Phorcus turbinatus*.

Appendix II



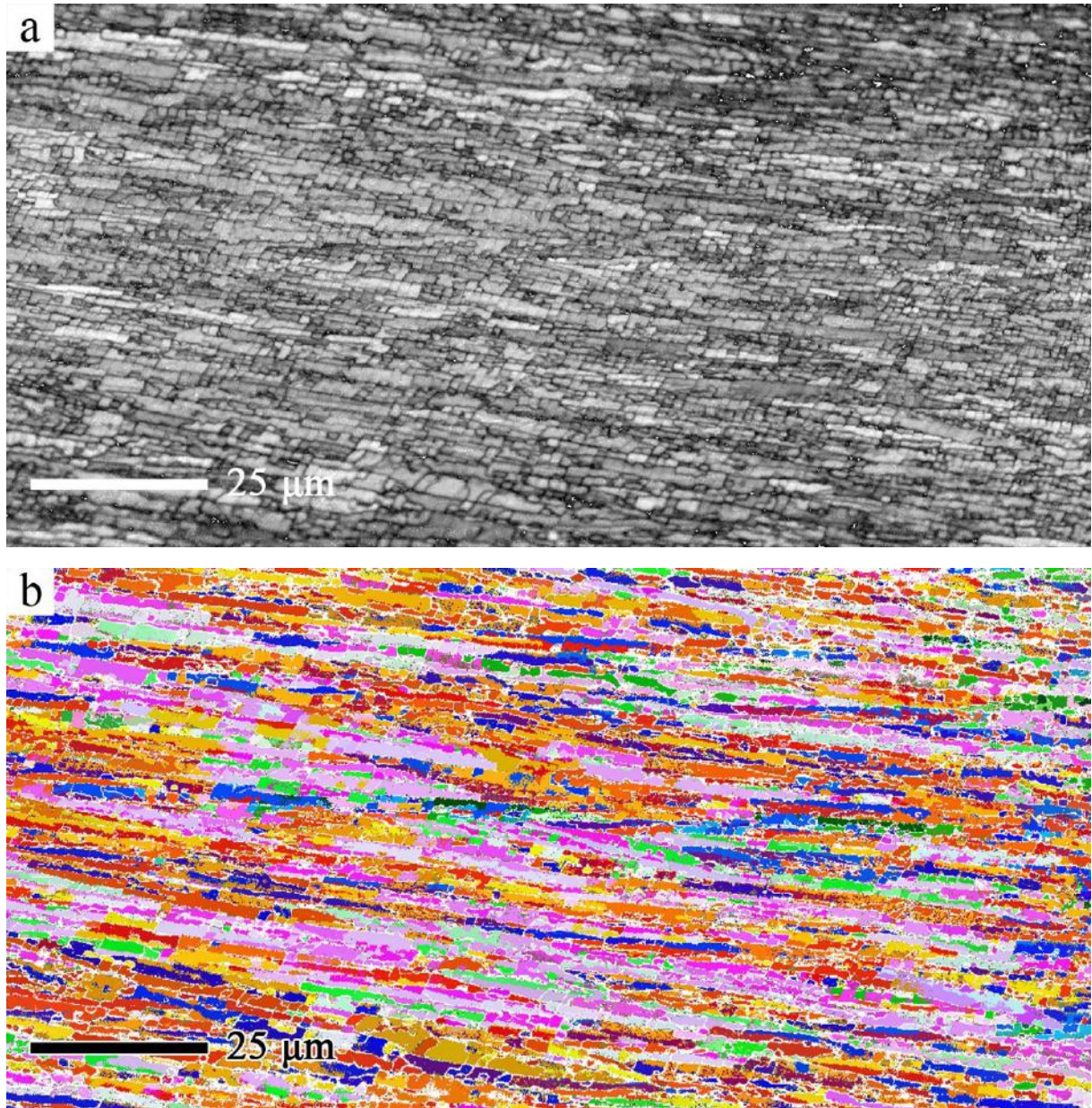
Appendix II EBSD results from the cross section of the nacreous layer of *Pinctada fucata*. (a) Band contrast map. The direction of the nacre lamellae is along the vertical direction of the surface. (b) Orientation information map with colour code of the Euler angles. Different colour areas indicate different crystal orientations.

Appendix III



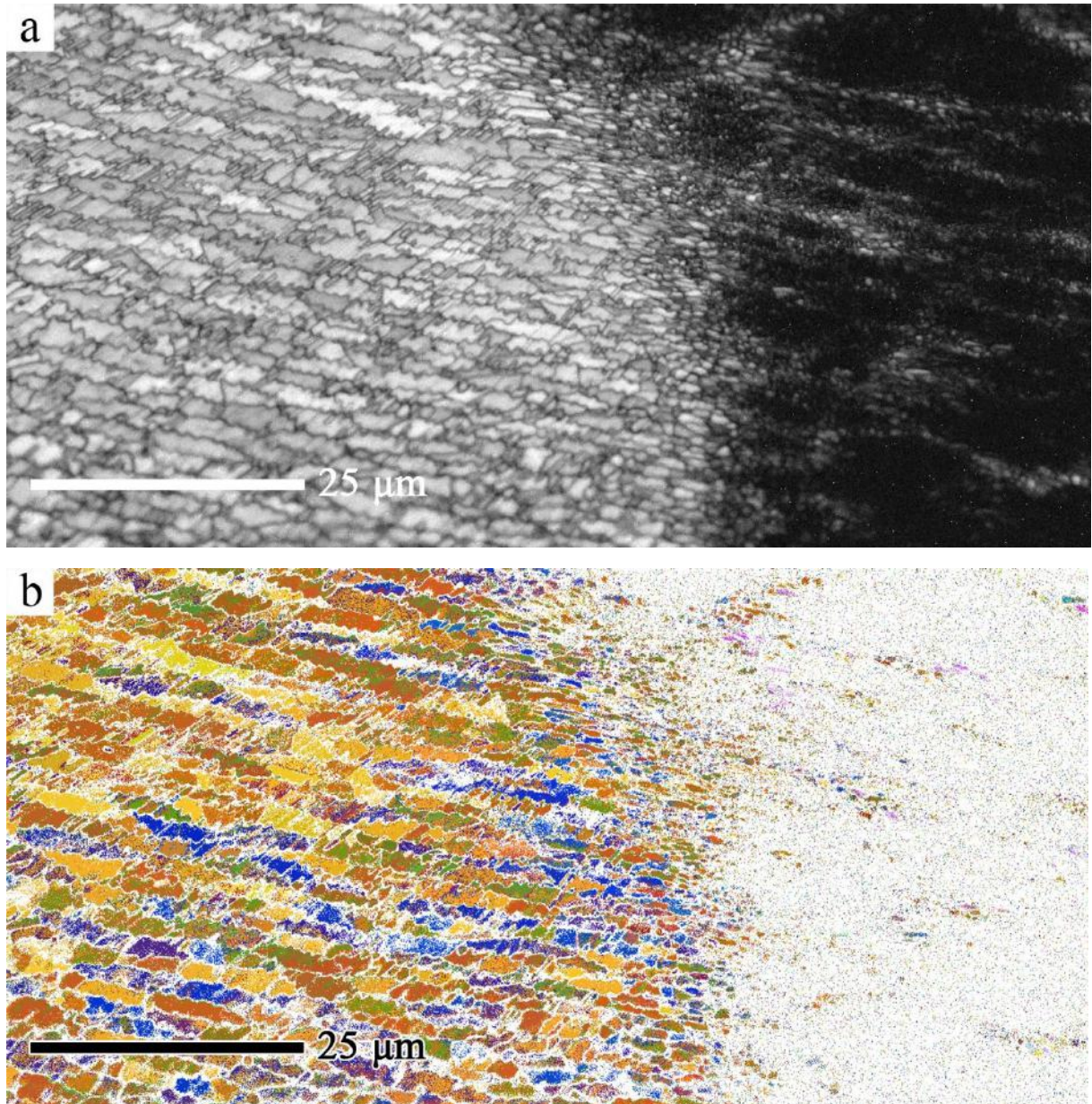
Appendix III EBSD results of the lateral section of the prismatic layer of *Anodonta cygnea*. (a) Band contrast map. The prisms are composed of granules with a size of ca. 1 µm. (b) Orientation information map showed colour code of the Euler angles. Different colour areas indicate different clusters of crystal orientations.

Appendix IV



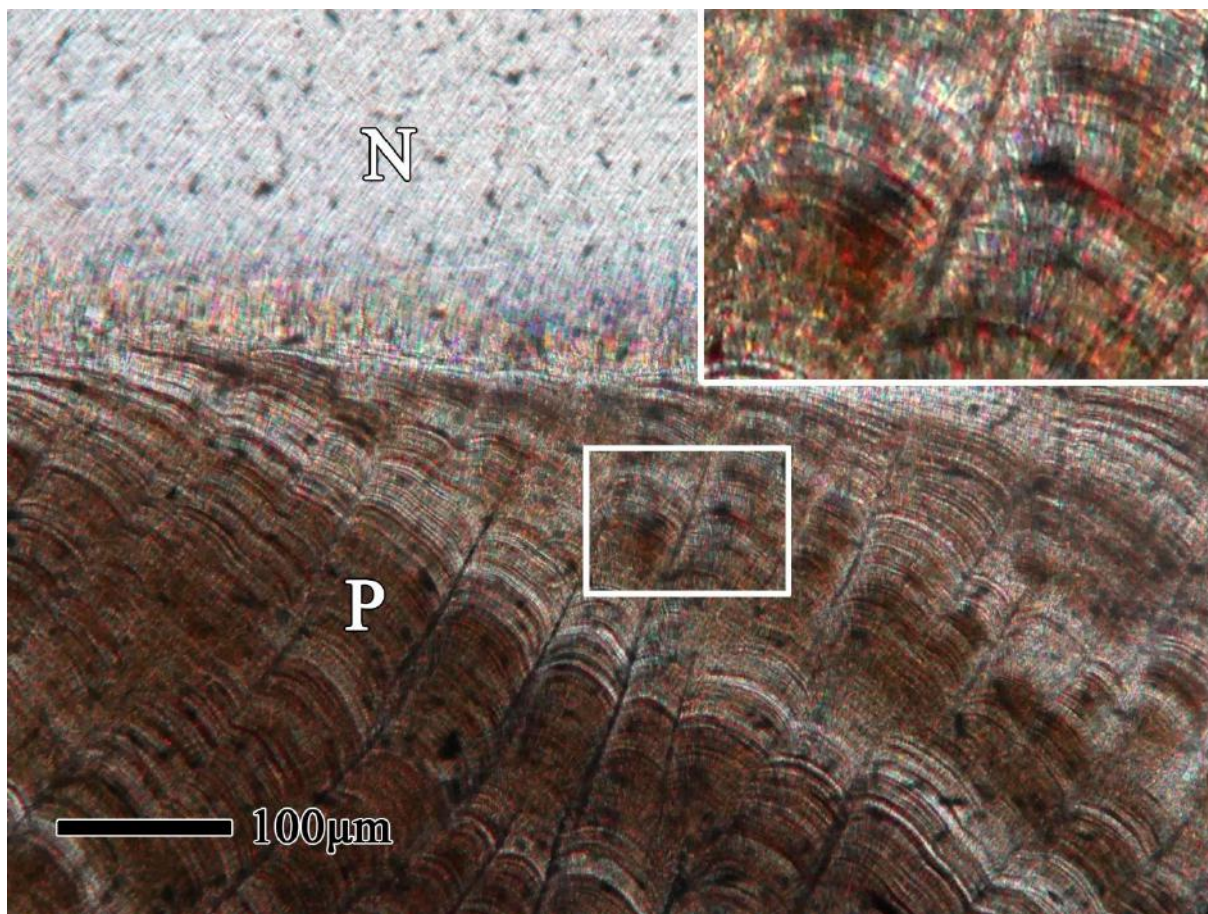
Appendix IV EBSD results of the cross section of the nacreous layer in *Anodonta cygnea*. (a) Band contrast map. The direction of the nacre lamellae is mainly along the vertical direction of the surface. (b) Orientation information map with colour code of the Euler angles. Different colours indicate different crystal orientations. The 'towergrains' are elongated in the direction perpendicular to the nacre lamellae.

Appendix V



Appendix V EBSD results of the cross section in *Anodonta cygnea* containing both nacreous (left) and prismatic (right) layers. (a) Band contrast map. The nacreous layer is divided by 'bands'. (b) Orientation information map with a colour code of the Euler angles. Different colours indicate different crystal orientations. The 'towergrains' are elongated in the direction perpendicular to the nacre lamellae.

Appendix VI



Appendix VI Thin section of the *Phorcus turbinatus* shell under a polarized optical microscope. The inset shows an enlarged area with curved growth lines and fibrous crystallites in pinnate texture.

Curriculum Vitae

Personal

Name Jianhan He

Birth 28.05.1989, Jingzhou, China

Nationality Chinese

Address Universität Hamburg
Mineralogisch-Petrographisches Institut
Grindelallee 48
20146 Hamburg

Phone +49 40 42838 2484

E-mail jianhan.he@uni-hamburg.de

Education

09/2007-06/2011 Bachelor of Science, China University of Geosciences, Wuhan, China.
Major: Gemology and Material Technology.
Undergraduate dissertation: Research of the differences between the pearls, the prismatic layer, and the nacles of *Hyriopsis cumingii*.

09/2011-06/2014 Master of Science, China University of Geosciences, Wuhan, China.
Major: Mineralogy, Petrology & Economic Geology.
Postgraduate dissertation: The morphology and preferred orientation study of biominerals in two species of shells.

10/2014-10/2018 Ph.D. candidate, Universität Hamburg, Hamburg, Germany.

Teaching activities

2012-2013 Lecturer of ‘Basis of Gemology’ and ‘Marketing of Gems and Jewelleries’, Wuhan University of Engineering Science, China.

Contributions to conferences

- 10/2015 **He J.**, Bandel K., Theodore M., Bismayer U. Shells of bivalves and gastropods – perfect bio-composites. Deutsche Mineralogische Gesellschaft, Berlin. Poster presentation.
- 03/2016 **He J.**, Zhao S., Bismayer U. Topological study of calcium carbonates in the mollusc shell *Pinctada martensii*. Deutsche Kristallographische Gesellschaft, Stuttgart, Germany. Poster presentation.
- 09/2016 **He J.**, Zhao S., Wei Z., Bismayer U. Hierarchical domain structure of calcium carbonates on *Pinctada martensii* shells. European Mineralogical Conference, Rimini, Italy. Poster presentation.
- 09/2017 **He J.**, Zhao S., Wei Z., Bismayer U. Mesoscale twinning patterns in a mollusc shell: *Pinctada martensii*. Deutsche Mineralogische Gesellschaft, Bremen. Oral presentation.
- 10/2017 **He J.**, Griesshaber E., Schmahl W., Bismayer U. The carbonate crystallite organization in the shell layers of *Pinctada fucata* and *Anodonta cygnea*. International Symposium on Biomineralization, Tsukuba, Japan. Oral and poster presentation.
- 03/2018 **He J.**, Griesshaber E., Schmahl W., Bismayer U. Comparison of the microstructure from two bivalve shells – *Pinctada fucata* and *Anodonta cygnea*. Deutsche Kristallographische Gesellschaft, Essen, Germany. Poster presentation.

List of publications

Kong J., Yang M., **He J.** Preliminary experiments of colour improvement of freshwater pearls during growth process (in Chinese), *China Gems & Jades*, 2012, (4): 153-157.

He J., Zhao S., Yang M. Preferred orientation of aragonite in nacre of *Pinctada martensii* shell determined by electron backscatter diffraction (in Chinese), *Chinese Journal of Inorganic Chemistry*, 2014, **30** (10): 2252-2257.

He J., Zhao S., Wei Z., Bismayer U. Mesoscale twinning in shells of *Pinctada martensii*, *Zeitschrift für Kristallographie*, 2016, **213**(11): 673-680

He J., Griesshaber E., Schmahl W. W., Bismayer U. The carbonate crystallite organization in the shell layers of *Pinctada fucata* and *Anodonta cygnea*. In preparation.

Acknowledgements

First, I would particularly like to thank my supervisor Prof. Dr. Ulrich Bismayer. He offered me a life-changing opportunity, I feel grateful and lucky to be one of his Ph.D. students. He is the kindest and most responsible person I have ever known. He created a working environment free from stress and fear, he provided comprehensive knowledge of mineralogy and crystallography, he built up all kinds of academic connections for me and he revised all the mistakes I have made in my posters, articles and thesis during the last years. There is still much for me to learn from him.

I would also like to thank the support from my second supervisor Prof. Dr. Jochen Schlüter from Centrum für Naturkunde, Universität Hamburg. He provided me literatures and samples of aragonite crystals, he is always ready to help me and his opinions on biominerals are valuable for my study.

I want to give special thanks to Prof. Dr. Klaus Bandel from the Institute for Geology, Universität Hamburg. He provided me plenty of shells to study. Thanks to his knowledge of shells, I quickly found the right direction at the beginning of my study.

I would especially like to thank Dr. Erika Griesshaber and Prof. Dr. Wolfgang Schmahl from Ludwig-Maximilians-Universität München for providing me opportunities to carry out EBSD measurements. Our cooperation and discussions are important for this work. I give also thanks to Dr. Laura Casella in Munich for the help of preparing samples for EBSD measurements, and to Prof. Dr. Peter Gille in Munich for the Laue diffraction measurements on single-crystal aragonite.

Thanks to Dr. Marc Theodore and Prof. Dr. Gerhard Schmiedl from the Institute for Geology, Universität Hamburg for providing me opportunities to carry out SEM measurements.

Thanks to Prof. Dr. Boriana Mihailova at Mineralogical-Petrographic Institute, Universität Hamburg for providing me chances to carry out Raman spectroscopy measurements on my samples. She is a living encyclopaedia for Raman spectroscopy and I learnt so much from her.

Thanks to Stefanie Heidrich at Mineralogical-Petrographic Institute, Universität Hamburg for helping me perform the EMPA measurements.

Acknowledgements

Thanks to all the kind help from Peter Stutz at Mineralogical-Petrographic Institute, Universität Hamburg for the preparation of the samples.

Thanks to Dr. Martin Ritter, Jens Timmermann and Lida Wang for letting me analyse the EBSD data at the Electron Microscopy Unit (BEEM) of Hamburg University of Technology, Hamburg Harburg

Thanks to Peter Zietlow, Kristoff Svensson, Anke Watenphul, Mascha Gollub, Reinhardt Kurtz, Tobias Beirau and all the other friends from my institute, their company is also very important for my study.

Thanks to my supervisors of bachelor and master theses, Prof. Dr. Mingxing Yang and Prof. Dr. Shanrong Zhao, they guided me on the road of studying biominerals. Thanks to all my other friends in Hamburg. Finally, I want to thank my parents for giving me the freedom and support to do the things I want to do.

This Ph.D. thesis is generously funded by the China Scholarship Council.